מכון ויצמן למדע
WEIZMANN INSTITUTE OF SCIENCE

חבור לשם קבלת התואר
דוקטור לפילוסופיה

Thesis for the degree
Doctor of Philosophy

מאת
טלי דדוש

By
Tali Dadosh

מדידות הולכה וספקטרוסקופיית רמאן של מולקולות בודדות בעזרת דימרים של ננו-חלקיקים

Conductance and Surface-Enhanced Raman Scattering of Single Molecules Utilizing Dimers of Nanoparticles

Regular Format

מנחים
פרופ' ישראל בר-יוסף
פרופ' יוסי שפרלינג

Advisors
Prof. Israel Bar-Joseph
Prof. Joseph Sperling

אדר א' תשס"ח

February 2008

מוגש למועצה המדעית של
מכון ויצמן למדע
רחובות, ישראל

Submitted to the Scientific Council of the
Weizmann Institute of Science
Rehovot, Israel

This work has been carried out
Under the supervision of
Prof. Israel Bar-Joseph
The Department of Condensed Matter Physics
The Weizmann Institute of Science
&
Prof. Joseph Sperling
The Department of Organic Chemistry
The Weizmann Institute of Science

To my Dear Parents: Orna & Reuven
To my Husband Gabi
To my Son Noam
With All my Love

Acknowledgments

It would be surely impossible to arrive to this page without the help of so many people; each in a particular way made every moment of my PhD term enjoyable, fascinating, and educative.

First and foremost, I wish to thank my advisors, *Prof. Israel Bar-Joseph* and *Prof. Joseph Sperling*, for putting so much faith in my ability to work well in both fields – Chemistry and Physics – and for their continued encouragement and exceptional support throughout the course of my studies.

I wish to thank *Prof. Amir Yacoby* for his guidance throughout the molecular transport project.

I would like to thank the people I have had the pleasure of collaborating with in the SERS project:

Prof. Gilad Haran for his excellent support and guidance throughout the research.
Prof. Garnett Bryant, from NIST, for assisting me in understanding the experimental results and for performing the plasmonic calculations.

I would like to thank the members of Prof. Bar-Joseph's lab:

Yoav Gordin for being such a wonderful partner and a great friend.
Eyal Cohen-Hoshen, Maria Dyshel, Avi Guttman, Michael Stern, and *Valery Garmider* for always maintaining a pleasant atmosphere.

I wish to express my gratitude to past and present members of Prof. Sperling's lab: *Galit Yahalom, Eyal Kamhi,* and *Yael Hacham* for their support and friendship.

I would like to thank the poeple in Prof. Yacoby's lab: *Hadar Steinberg, Gilad Barak, Basile Verdene, Sandra Foletti, Ophir Auslaender, Shahal Ilani,* and *Jens Martin* for their assistance and for creating such a pleasant atmosphere.

Special thanks go to *Timur Segai* for fruitful discussions and collaborations, as well as his assistance and friendship.

I wish to acknowledge *Dr. Diana Mahalu*'s help in the e-beam writing, *Olga Raslin's* help in the preparation of optical masks, *Yoram Rotblat's* help in technical support and the help of the entire Sub-Micron center staff; without their technical as well as moral support, this work would not have been possible.

I would like to thank *Dr. Ronit Popovitz, Orna Yeger, Talmon Arad,* and the entire electron microscopy unit at the Weizmann Institute for introducing me to the world of electron microscopy.

I thank *Dr. Veronica Frydman* for the organic synthesis.

My gratitude also extends to my advisory committee, *Prof. David Cahen* and *Prof. Eli Zeldov* for their guidance and constructive comments over the years.

My special and warmest thanks go to my dear friends at the Weizmann Institute:
Hadas Shtrikman for great friendship
Ifat Kaplan-Ashiri, Sharon Ruthstein, Berith Issac, and *Eya Ben-Ari* for their continuous interest, unfailing support, and immeasurable assistance during the last few years.

Finally, I am grateful for my beloved husband, *Gabi*, for his love and devotion.

Abstract

In the past few years, the field of molecular electronics and in particular, the development of new techniques for contacting and measuring single molecules, has emerged, providing new insights into this field. The relatively small size of a molecule, typically of the order of 1 nm, requires innovative approaches in order to develop functioning single-molecule devices. The experimental methods currently used for single-molecule measurements provide little control over the number of molecules bridging the gap or the local electronic properties of the metal-molecule contact. In this thesis, a new approach for contacting a single molecule is presented that provides better control of these parameters. Our method is based on synthesizing a dimer structure consisting of two gold colloids connected by a thiol group to either side of the molecule. This structure is then positioned between two electrodes by electrostatic trapping and, thus, the conductance of the molecule can be measured.

The fundamental questions addressed by the field of molecular electronics are as follows: “what is the conductivity of a junction containing an individual molecule and how is it affected by the molecule's specific structure?” We were able to shed some light on these questions by studying the electrical conduction through three short organic molecules that differ by their degree of conjugation. We will consider here a fully conjugated molecule, 4,4'-biphenyldithiol (BPD), Bis-(4-mercaptophenyl)-ether (BPE), in which the conjugation is broken at the center by an oxygen atom, and 1,4-benzenedimethanethiol (BDMT), where the conjugation is broken near the contacts by a methylene group. We found that the presence of localizing groups such as the oxygen in the BPE and the methylene groups in the BDMT suppresses the electrical conduction dramatically, relative to the conjugated molecule, BPD. A unique feature of the BPD molecule is the appearance of reproducible, pronounced peaks in its conductance at certain voltage values. The position of peaks in the spectrum was affected by the electrostatic environment, resulting in random gating.

In view of the above developments, my thesis focuses on surface-enhanced Raman scattering (SERS) measurement of single molecules. Single-molecule spectroscopy is an emerging field that provides detailed information on molecular response, which is unavailable in measurements performed on an assembly of molecules. The obvious problem, however, in implementing most spectroscopic techniques, such as Raman scattering, is the very weak signal obtained from a single molecule. Interestingly, the

Raman signal from a molecule has been shown to increase dramatically when the molecule is adsorbed to metal particles of certain types having sub-wavelength dimensions [1, 2]. This enhancement technique, known as surface-enhanced Raman scattering, can increase the Raman signal by as much as 14–15 orders of magnitude, which has been shown to be sufficient for performing single-molecule spectroscopy successfully.

Dimer structures are not only attractive for conductance measurements on single-molecule devices; they could also serve as an efficient antenna system that greatly enhances the electromagnetic field at the center of the dimer, where the molecule resides. Dimers provide a basic experimental model for studying the fundamentals of the SERS enhancement, which are not well understood. Dimers have the advantage of possessing a small gap (on the order of a nanometer) that is beyond the limit of today's sophisticated lithography techniques. By utilizing the dimer structures that contain a Rhodamine 123 molecule, we were able to resolve some fundamental questions regarding the SERS enhancement mechanism. The issue of how the nanoparticles' surface plasmon properties affects the SERS enhancement was addressed both experimentally and by calculations. Moreover, it was predicted by our calculations that when the dimers consist of large nanoparticles, a non-uniform enhancement of the different molecular modes of Rhodamine 123 should occur. This was also observed experimentally where specific peaks of the SERS spectrum were more pronounced than others.

I will begin this thesis with an introduction to the field of molecular electronics; I will review the use of different molecular clips and I will briefly describe some theoretical approaches and the experimental methods used for single-molecule measurements. I follow this by introducing the field of surface-enhanced Raman spectroscopy of single molecules. More specifically, I will describe the mechanism underlying the Raman enhancement and its relation to surface plasmons of nanoparticles. The introduction ends with a detailed description of the dimer approach and its potential use for performing transport and SERS measurements of single molecules. The results are composed of two parts: the first is related to transport through single molecules, including characterization of dimers and their contacts to the electrodes as well as transport measurements through single molecules. The second part relates to the SERS originating from dimers embedding a single molecule. Next, I will discuss the distribution of the SERS intensity as a result of the different

orientations of the dimers with respect to the laser polarization. In the final chapter of this work, I will discuss the dependence of the SERS intensity on the size of nanoparticles, and explain the results using calculations of the near-field in the dimer's junction.

Table of Contents

Abbreviations

SERS	Surface Enhanced Raman Scattering
IR	Infra Red
EM	Electromagnetic
TEM	Transmission Electron Microscope
SEM	Scanning Electron Microscope
EFTEM	Energy Filtered TEM
T4	Tetra-polythiophene
Rh123	Rhodamine 123
MCBJ	Mechanically Controlled Break Junction
OPE	Oligo(phenylene ethynylene)
OPV	Oligo(phenylene vinylene)
SAM	Self Assembled Monolayer
HRTEM	High Resolution TEM
DDW	Double Distilled Water
SET	Single Electron Transistor
MBE	Molecular Beam Epitaxy
DFT	Density Functional Theory
MIBK	Methyl isobutyl ketone
BPD	4,4'-biphenyldithiol
BPE	Bis-(4-mercaptophenyl)-ether
BDMT	1,4-benzenedimethanethiol

1. Introduction

1.1 Electrical transport through single-molecule junctions

The field of nanotechnology has undergone enormous progress over the past few years in terms of the capabilities for designing and controlling nano-sized devices and structures. In a world where semiconductor devices are increasingly miniaturized, traditional "top-down" processing methods are now gradually being replaced by emerging "bottom-up" technologies. One such approach is the use of molecules as building blocks for electronic devices, as part of the emerging field of molecular electronics. First proposed by Aviram and Ratner in 1974, a single organic molecule was predicted to behave as a rectifier [3]. Since then, many molecules functioning as electronic devices have been synthesized. However, the relatively small size of molecules, typically 1 nm, calls for novel approaches to realize a functioning single-molecule device.

A fundamental issue in the field of molecular electronics is: “what is the conductivity of a junction containing an individual molecule?” I will discuss this issue here by examining two different types of molecules: saturated and conjugated ones. I will also review the effect of the molecular binding groups and the type of electrodes on the conduction properties. I will then introduce theoretical approaches that are used to determine transport through molecules. Finally, I will review experimental techniques that are used for measuring single molecules.

Transport through saturated molecules

Saturated molecules such as alkanes have a very large gap between occupied and empty states; therefore, transport is expected to be inefficient. In general, the transport through saturated hydrocarbons can be described as coherent tunneling through a potential barrier that is formed by the molecule, thus creating an exponential dependence of the current on the molecule's length [4]:

$$I = I_0 e^{-\beta d}, \quad (1)$$

where I is the current, and d is the molecule’s length. The tunneling decay factor, β, is given by

$$\beta = 2\frac{\sqrt{2m^*\alpha(\Phi - (eV/2))}}{\hbar^2}, \quad (2)$$

where Φ is the tunneling barrier height, m^* is the effective electron mass, α is an asymmetry parameter for the potential profile across the junction ($\alpha=1$ for symmetric coupling), and $\hbar$ is Planck's constant divided by 2π. As shown, β depends on the metal involved in the tunneling, on the nature of the interface, and on the applied voltage, because the gap between the energy of injected electrons and of the frontier orbitals decreases as voltage increases [5]. This dependence was validated by experimental studies mostly in the self-assembled monolayer (SAM) configuration, and the value of β was found to be around 1 $Å^{-1}$ [6-8]. Smaller values of β values were found in highly conjugated organic bridges in the range of 0.2–0.6 $Å^{-1}$ [9, 10]. In vacuum, β values are estimated to range from 3.0 to 4.0 $Å^{-1}$ [11].

Transport through conjugated molecules

Although the transport mechanism through alkane chains is well understood experimentally and agrees well with the theory, transport through conjugated systems is much more complicated, and only a few systematic data are available. In π-conjugated systems the electrons are delocalized throughout the molecules, providing a low barrier path for electron transport. These systems have a low HOMO-LUMO gap (3-5 eV) relative to saturated molecules (8-10 eV) [12]. Indeed, the transport efficiency of conjugated molecules was found to be higher than through saturated molecules of approximately the same length [7, 13, 14].

Among the huge variety of conjugated molecules, two classes were extensively studied: oligo(phenylene ethynylene) (OPE) and oligo(phenylene vinylene) (OPV). A comparison between the two classes exhibits how the degree of conjugation affects the conductance. In OPE the phenyl rings that are connected via a carbon-carbon triple bond can rotate freely at room temperature, whereas in the OPV system the phenyl rings that are connected by a carbon-carbon double bond are at the same plane. Thus, OPV is better π-conjugated than OPE. A comparison of the charge transport through the two systems is shown in Figure 1 [15]. The conductivity of OPV was found to be fivefold larger than that of OPE, as expected from a molecule that has higher co-planarity (the butyl groups in OPV cause a steric hindrance that restricts the torsional rotation of the phenyl rings). This figure also shows the transport through the

saturated molecule (C12); as expected, its conductivity is significantly lower than that of the two conjugated molecules.

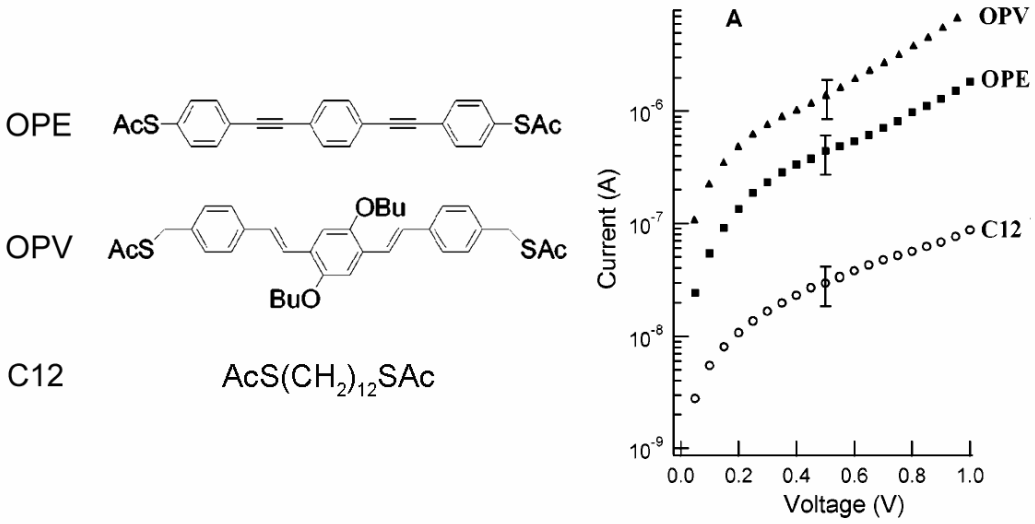

Figure 1: Molecular structure of OPE and OPV and measurements by Kushmerick *et al.* [15].

These experimental results were found to be in qualitative agreement with theoretical calculations of the conductance of these molecules. However, in many cases, there was no qualitative agreement. The predicted theoretical current values were often found to be a few orders of magnitude higher than the experimental ones. In addition, the measured spectrum of transmission peaks does not always fit the theoretical spectrum [13].

The effect of metal – molecule contact on the conductance

The molecular structure plays an important role in determining the conductance of the molecular device. However, when a molecule binds to a metal, its electronic characteristics change. Thus, it is essential to take into account the characteristics of the full system, including the metal–molecule contacts [16]. I will discuss here the types of chemical groups (clips) that are commonly used to form the molecule-metal contact, and then I will elaborate on the effect of the different metals on the conductance.

Molecular clips

The most common metal-molecule system that is used for single molecules and SAM measurements is gold-thiol. Thiols (SH) can bond to different gold surfaces, for

example, Au(111) and Au(100), resulting in "on-top" and "hollow" binding configurations, respectively. The two configurations are close in energy but have different Au-S-C bond angles, 180° for hollow and 105° for on-top [17].

The bond angle between the molecule and the surface plays an important role in the conductivity of a molecule. In general, maximum overlap and full conductance occur when the π-orbitals of the end atom of the molecule are oriented perpendicular to the surface. According to calculations done by Kornilovitch *et al.*, the conductivity of (1,4)-dithiolated-benzene for each binding configuration results in different values. Whereas the hollow position is 2 to 3 times more conductive than the on-top position, the conductivity curves are qualitatively similar [5, 18]. The effect of the angle between the measured molecule and the electrode surface has been demonstrated experimentally by comparing a conjugated molecule with thiol clips at *para* and *meta* positions relative to the rest of the molecular structure. As expected, the conductance is higher in the case of the *para* position where the molecule is perpendicular to the electrode [19].

It was shown by calculations that the thiol-gold bond is dominated by sigma orbital interactions. Although the fully π-conjugated molecules such as OPE, may enhance the electron conduction, the lack of π-orbital overlap with the metal–molecule interface (π-σ) greatly decreases the overall conductivity of the molecule [12]. However, exactly how sulfur binds to gold remains unclear. Recently, a work by Kornberg's group shed some light on this topic. Briefly, they prepared gold nanoparticles of a uniform size covered with SAMs of thiolated molecules. By X-ray diffraction analysis of the covered nanoparticles, they found that the S-Au bond length is in the range of 2.2 to 2.6 Å, and at least one of the gold atoms binds two sulfurs [20, 21].

Although thiols are the most common binding group for gold, amines were found to provide a stable bond as well [22]. Amines are not known to form stable SAMs on gold; however, they are used to passivate gold nanoparticles. The bonding between Au and amines is acquired by delocalization of the lone-pair of electrons from the amine nitrogen to coordinatively unsaturated surface Au atoms. Not all amines form a stable bond with metals; tertiary amines are weakly bound because of the added steric bulk to the nitrogen center. However, metal-molecule-metal junctions of primary amines and gold provide stable and reproducible conductance [22, 23].

Effect of metal type on the conductance

Not only the binding group (clip) of the molecule affects the conductivity of a molecular junction—the electrode's metal also affects it. Seminario *et al*. compared the *I-V* characteristics of benzene with two thiol clips connected to metals of groups 10 (Ni, Pd, and Pt) and 11 (Cu, Ag, and Au) [24]. The conductivity was found to be higher for group 10 junctions than those of group 11. This was attributed to the different angles of the metal-clip-molecule and to the orbital contribution of the metals to the bond. Seminario *et al*. showed that there is a strong *s* orbital contribution to the elements of group 11, roughly threefold higher than to the elements of group 10; group 11 elements also present stronger *p* and *d* contributions. Thus, a higher hybridization of the π-orbitals of the benzene ring with group metal 10 occurs.

In addition, in all cases of metals, the angle between the molecule and the electrode surface was smaller than 180°. However, the angle was closer to 180° for metals of group 10, resulting in a larger overlap between the metals and the molecular orbitals, and a higher conductivity.

Modeling the molecular conductance

The ability to predict the molecular conductance of a specific junction is of a great importance. Taking this into consideration, it is understandable that a comparison between the experimental results and the theoretical calculations is not straightforward because many factors can affect the molecular conduction. It was proposed that the molecule can be modeled as a small metal island between two leads, as in the single electron transistor (SET) configuration.

Single Electron Transistors

The configuration of a SET is shown in the scheme of Figure 2. It consists of two tunnel junctions sharing one common island. When a voltage difference is applied to two electrodes ($V_{source\text{-}drain}$), an electron can travel from the source to the drain by going through the island via a tunneling process.

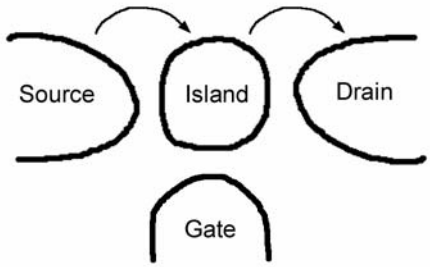

Figure 2: Scheme of a single electron transistor. Electrons tunnel from the source electrode to the drain electrode through an intermediate island. A gate electrode is located nearby; it is used to tune the electrical potential of the island.

Adding a charge to an island requires energy of

$$E = \frac{Q^2}{2C} - QV_g , \quad (3)$$

where C is the total capacitance between the island and the system, Q is the charge of the island, and V_g is the gate voltage.

When the Fermi energy of the leads is placed in the middle of the gap between the different states, then adding a charge Q to the island requires energy of $Q^2/2C$. Since one cannot add less than one electron, the flow of current requires an electrostatic energy of $e^2/2C$. Hence, there is a threshold voltage of V=e/2C above which current will flow. This voltage barrier is called the *Coulomb blockade* [25] and can be observed if the thermal energy is smaller than the charging energy ($k_BT \ll e^2/2C$). If the island is small enough, the presence of an electron on the dot creates an electrostatic barrier that prohibits a second electron from tunneling into the island until a new threshold is reached.

The charging energy levels of the island are evenly spaced and depend on the island capacitance, which has the following form (neglecting capacitance to the leads):

$$C = 4\pi\varepsilon_0 R , \quad (4)$$

where R is the island radius and ε_0 is the permittivity. It can be seen from Equations 3 and 4 that as the island gets smaller, the energy level spacing gets larger.

The electrical potential of the island can be tuned by a third electrode (gate) that is positioned nearby. When a positive voltage is applied to the gate electrode, the energy levels of the island electrode are lowered, as shown in Figure 3a. The electron (green 1) can tunnel onto the island (2), occupying a vacant energy level at the island. From there it can tunnel onto the drain electrode (3) where it inelastically scatters and reaches the drain electrode Fermi level (4). The described process is periodic with the

gate voltage, leading to the phenomenon of the *"Coulomb blockade oscillations"*. Mapping the conductance through the island by varying both the source drain voltage and the gate voltage yields the *Coulomb blockade* diamond plot, illustrating the opening and closing of channels in the island (Figure 3b).

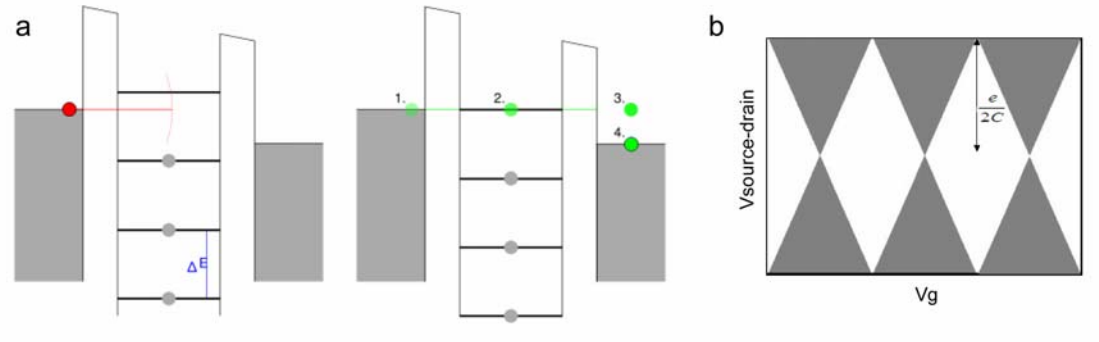

Figure 3: a) Energy levels of the SET. On the left, when a voltage difference between the source and the drain is applied, an electron can tunnel through the island only when its energy level is aligned with that of the island. When a positive voltage is applied to the gate electrode, the energy levels of the island electrode are lowered and aligned with the source, allowing tunneling from source to drain (right). b) A plot of *Coulomb blockade* diamonds. The white area represents the stability regions at which there is no conductivity through the island. Conduction takes place in the gray regions.

Modeling the transport through molecules

The conductance through a molecular junction can be described in a similar manner to that through an island. An electron is transmitted through the molecule only if it has sufficient energy to reach the molecular energy level. Therefore, calculating the energy levels of a molecule connected to two metal electrodes is needed to determine the conduction through it.

The conductance through a molecular junction can be described using the Landauer formalism, which was originally used to describe the coherent electron transport through small metallic junctions [26]. In this formalism, current electrons are elastically scattered between two leads. In this coherent limit, energy is dissipated in the lower potential lead; no energy dissipation occurs in the molecule itself. The conductance is given by:

$$G = \frac{2e^2}{h} M T_s T_d , \quad (5)$$

where T_s and T_d represent the average transmission probabilities from the source to the molecule and from the molecule to the drain, respectively. M is the transmission coefficient of the molecule and $2e^2/h$ is the contact resistance.

The electrons that contribute to the current are those located near the Fermi level of the leads. Hence, the conductance will be highly sensitive to where the Fermi level lies. Upon interaction between a molecule and metal leads, charge flows and is rearranged; consequently, the electronic states of the molecule and the leads hybridize. This will typically lead to a broadening of the molecular energy levels and also to the appearance of new energy states in the molecular energy gap. The voltage division of the applied bias across the molecule is also crucial in determining the conductance spectrum. As a result, two molecules with identical energy levels can give rise to totally different conductance spectra.

Calculation of the transmission function of a molecule poses a real challenge. In a full calculation, the electrons must be described as quantum particles and the electron energy is calculated by using the many-body Schrödinger equation including electron-electron interactions. It is generally very difficult to solve exactly, except for extremely simple cases of single-electron systems. Thus, approximation methods are used for such calculations. A full description of the various calculation methods is beyond the scope of this introduction; however, I will briefly introduce the principles of density functional theory (DFT), a method that is commonly used for such calculations. In this method, electrons are described as non-interacting particles moving in an effective potential that is created by other electrons [27]. The effective potential depends on the average position of the other electrons and needs to be determined using a self-consistent loop with the following steps:

$$\hat{H}_{1el} = -\frac{\hbar}{2m}\nabla^2 - V^{eff}[n](r) \quad (6)$$

$$\hat{H}_{1el}\Psi_\alpha(r) = \varepsilon_\alpha \Psi_\alpha(r) \quad (7)$$

$$n(r) = \sum_{\varepsilon \le \mu} \Psi_\alpha(r) \quad (8)$$

Equation 6 defines the one-electron Hamiltonian, where the first term describes the kinetic energy and the second describes the effective potential energy that depends on the electron density, n. From the one-electron Hamiltonian, one can determine the one-electron eigenstates by solving Eequation 7. Finally, the electron density is determined by summing all occupied one-electron eigenstates (that have an energy below the chemical potential of the system μ), following Equation 8. The flowchart of the self consistent loop is described in Figure 4.

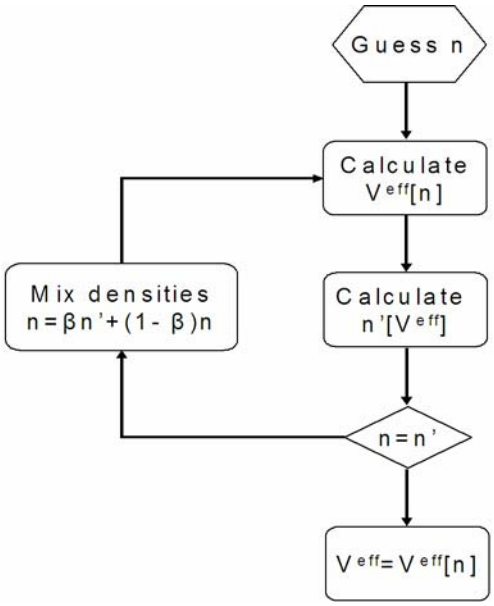

Figure 4: Flowchart of the self-consistent loop of DFT [27].

A molecular junction problem is usually treated in two parts, an "extended molecule", consisting of the actual molecule and a few electrode atoms at each end, and the remaining the electrodes. The latter are represented in terms of their surface Green's functions, and act as source and drain, and the electronic structure of the extended molecule is solved by DFT.

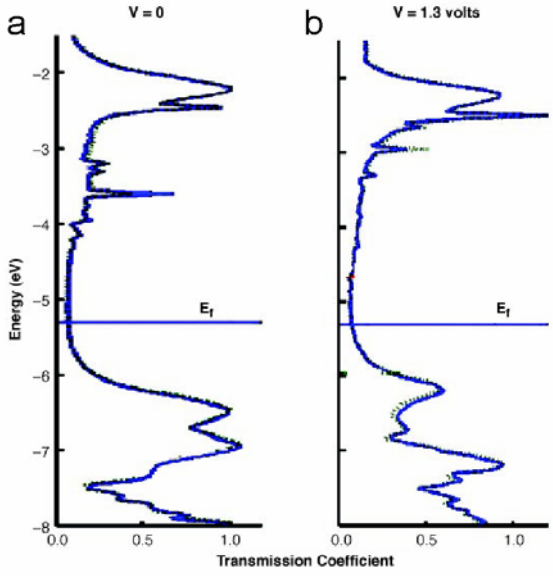

Figure 5: Computed transmission coefficient of the benzene dithiol junction, using DFT, for a) zero bias, and for b) 1.3 volts. The transmission varies with applied voltage, because of changes in the electronic states of the molecule [28].

The DFT method is extensively used in the field of molecular electronics, enabling the examination of basic questions such as the alignment of the molecular orbitals

with the electrode's band [29], as well as the effect of the type of molecular clip, and its binding site on the electrode, on the conduction [5, 24, 30]. It has also been used to study the nonequilibrium electron distribution under applied bias, as shown in Figure 5 [28].

The DFT calculation is a mean field theory; it is therefore applicable only in cases where electron-electron correlations do not play an important role. However, it will be applicable if the connection of the molecule to the leads is good. In the Coulomb blockade regime, where the connection is essentially through a tunnel barrier, it will no longer apply. In a recent paper by Lindsay and Ratner, it was shown that with small molecules, such as the ones studied in this work, the experimental results do not fit DFT calculations [31].

Techniques for contacting single molecules

In order to conduct electrical measurements at the single molecule (or a few molecules) level, one needs to generate an electrical contact in a reliable way. Although conceptually simple, this goal is hard to achieve. The length of molecules is typically of the order of 1 nm, which makes contacting a technological challenge. A variety of techniques for contacting and determining the electronic transport through single molecules has been used; each technique has its own advantages and disadvantages [32]. In the following sections, a few methods are briefly discussed.

Fixed electrode techniques

There are a few variations for using this direct approach in which two electrodes separated by a few nanometers are constructed on a solid substrate and then bridged by molecules. In the first example, a thin layer of two closed strips of amorphous carbon are deposited utilizing electron beam deposition in the SEM [33]. These strips are used as a protecting mask during an etching procedure that results in a very narrow gap. A second example is the use of shadow evaporation to bridge the gap of electron beam-defined electrodes to a few nanometers [34, 35]. Another method for creating nanometer gap-sized electrodes is *electromigration* (Figure 6a, b) [36]. The formation of a nanometer-sized gap is achieved by breaking fabricated nanowires by a controlled passage of current. In this method, low temperature measurements and

gating are straightforward. However, it is difficult to control the gap and to ensure the existence of a molecule in the gap.

Mechanically controlled break junctions (MCBJs)

In this technique a small electrode gap is formed by bending a thin metal wire positioned on a flexible substrate until the metal wire breaks [19, 37, 38]. The electrodes are then covered by a self-assembled monolayer and are slowly pushed back until electric contact is obtained (Figure 6d). This technique is very reliable but gating is not readily achieved and the contact area is not well defined. Moreover, cooling down is barely possible because of the different thermal expansion coefficients of the materials used, which results in a controlled drift of the electrode spacing. Nevertheless, Reichert *et al.* [39] demonstrated low temperature measurements by adsorbing the molecules at room temperature, then pulling them apart by tearing some gold atoms with the molecule edge, and then cooling down the system and recovering the contact.

Scanning probe measurements

In this technique, contact with the molecule is achieved by using the metal tip of an atomic force microscope (AFM) or a scanning tunneling microscope (STM) [40-43]. The molecules are adsorbed on a conductive surface and electronic transport measurements can be performed, as shown in Figure 6c. Although this is a direct approach for conducting molecular measurements, the minimum number of measured molecules is limited by the tip dimensions. A way of overcoming this limitation is to insert dithiolated molecules into a monolayer of mono-thiolated molecules; the free thiol groups at the top of the film were bonded to gold nanoparticles. By attaching the tip to a single gold nanoparticle, one could perform transport measurements through single molecules [42, 43]. However, measurements of current can be very sensitive to applied stress by the tip and to the system's asymmetry. Often the electrical connections to the molecules are not via a chemical bond but by mechanical contacts, a fact that can dramatically affect the results.

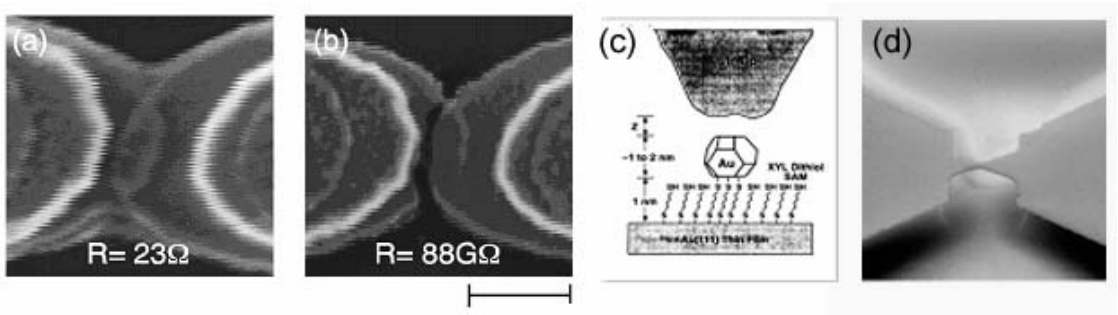

Figure 6: a-b) SEM image of a representative *electronmigration* method (a) before and (b) after the breaking procedure; the scale bar is 200 nm [36]. c) Schematic illustration of measurement systems using STM and Au nanoparticles showing contact with only a few molecules [43]. d) SEM image of electrodes created using the MCBJ technique [19].

The main difficulty with single-molecule measurements is the low statistics and the large variability of the results. However, Tao's group overcomes this limitation using a different approach. More specifically, they used both AFM and MCBJ to fabricate and measure molecular junctions [44]. They repeatedly moved the AFM tip (or opened the MCBJ) in and out of contact, in a controllable way. During the process of pulling out the tip, the current flow between the tip and the substrate was recorded, showing a change in conductance in discrete steps. Each discrete step is accompanied by a decrease of force that corresponds to a molecular break. Thus, one can collect extensive statistics and by creating a histogram of all the data, assign a clear value to the low bias conductance of the molecule. This method has been successfully used to characterize the conductance of the H_2 molecule [38, 45], to measure the conductance of alkanes and bipyridine molecules at room temperature [46], and recently to show the dependence of conductance in biphenyl molecules on the angle between the two Benzene rings [23].

1.2 Surface-enhanced Raman scattering of a dimer structure

The Raman Effect

Raman spectroscopy is a very powerful technique that provides rich structural information on the vibrational energies of molecules and thus qualitatively identifies the sample. When photons interact with a molecule, most of them are elastically scattered. This process is called Rayleigh scattering, in which the scattered photon has the same wavelength as the incident photon (Figure 7).

In Raman Spectroscopy the photons are inelastically scattered by molecules [47]. This effect was discovered in 1928 by C.V. Raman, who demonstrated that inelastic collisions may cause the molecule to undergo a quantum transition to a higher vibrational level. Subsequently, a transition to a lower vibrational level occurs and the scattered photon has a lower energy than the incident photon (Stokes line). If the molecule is already in a vibrational level above its lowest level, a transition to a lower energy level might occur (anti-Stokes line). The Stokes and anti-Stokes lines are thus shifted from the laser line in the frequency of the characteristic molecular vibration energy. These scattering events involve a "virtual" level, as shown in Figure 7. The only condition needed for Raman scattering to occur is that the energy of the incident photon must be larger than the energy difference between the final and initial levels of the actual transition.

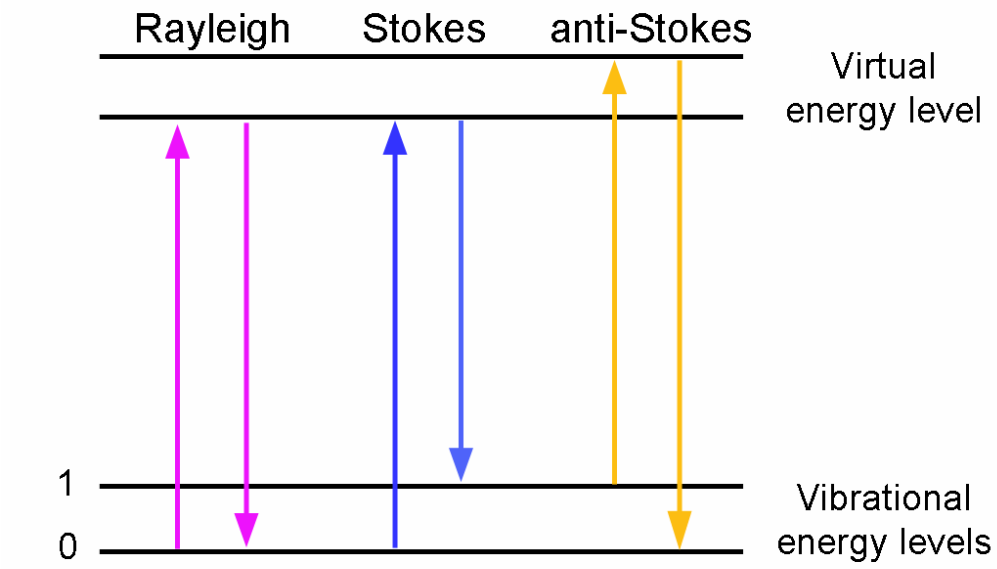

Figure 7: Schematic illustration of the excitation of Rayleigh, Stokes, and anti-Stokes lines. The transitions are shown in colored lines with arrows, indicating the excitation and the emission.

The basic selection rule for Raman scattering is that there must be a change in the polarizability of the molecule when the transition occurs. This condition is fulfilled when the transition moment integral is nonzero:

$$P_{nm} = \int \Psi^m \alpha \Psi^n , \quad (9)$$

where α represents the polarizability of the molecule. The symbols Ψ^m and Ψ^n represent the initial and final time-dependent wave function states, respectively. In contrast, for a vibrational motion to be infra red (IR) active, the dipole moment of the molecule must change. For example, a symmetric stretch in a carbon dioxide molecule is Raman active because the polarizability of the molecule changes, whereas it is not IR active since there is no change in the dipole moment.

The Raman effect is very weak; it comprises a very small fraction of the incident photons in comparison to Rayleigh scattering. However, when the frequency of the excitation laser is close to the frequency of the electronic transition of the molecule, the scattering is enhanced up to six orders of magnitude. This is the so-called *resonance Raman* effect [48].

Surface-Enhanced Raman Scattering

Although Raman spectroscopy is a powerfull tool that provides a fingerprint of molecules, it was not used for ultra-sensitive detection of molecules. This is because of the extremely small cross section, which in turn, requires a large number of molecules to achieve an adequate conversion rate from the excitation laser to the Raman photons.

In 1977, Van Duyne and Jeanmaire [1] and independently, Albrecht and Creighton [2] discovered the novel phenomenon of a strongly increased Raman signal from molecules attached to rough silver surfaces. The effect was first observed in 1974 by Fleischman and coworkers [49], but it was attributed to the increased surface area of the rough substrate. This effect, known as surface-enhanced Raman scattering (SERS), shows a Raman signal enhanced by 14-15 orders of magnitude. This was occurs when molecules are adsorbed on surfaces with features on the 10-100 nm length scale, as provided by gratings, metal spheroid assemblies produced by lithography, and nanometer-sized metallic structures [50, 51]. The extremely large Raman cross sections, on the order of 10^{-17} to 10^{-16} cm^2 per molecule, in SERS

experiments used for dyes adsorbed on colloidal silver, enable single-molecule detection [52, 53].

SERS Enhancement Mechanisms

The enhancement mechanisms of SERS can be divided into two different effects: an electromagnetic and a chemical one [50]. The chemical enhancement results from broadening of the molecular orbitals of the adsorbate molecule by its interaction with the conduction electrons of the metal substrate [54, 55]. Resonances whose energies lie near the Fermi energy are only partially filled, whereas those that are situated well below are completely filled. The inclusion of metal states in chemisorption introduces new possibilities for resonance excitation at frequencies much lower than those of the intrinsic intramolecular excitations of the free molecule. There are two possibilities for new excitations: electrons can be excited from the filled adsorbate orbitals to unfilled metal orbitals above the Fermi level (molecule-metal charge transfer), or metal electrons can be excited to the partially filled adsorbate affinity level (metal-molecule charge transfer). Chemical enhancement factors are traditionally assumed to be in the range of 10-100, although recent studies suggest that these factors can be as high as 5 orders of magnitude in some cases [56].

It is generally agreed that most of the SERS enhancement is caused by the electromagnetic (EM) effect [50, 57]. EM enhancement is due to the unique interaction between the electromagnetic radiation and mobile surface charges, typically the conduction electrons in metals. For particles with a diameter much smaller than the wavelength of the exciting light, the interaction of metal with light can resonantly excite collective electron oscillations, the so-called *localized surface plasmons*. As a result, a strongly enhanced electric *near-field* localized at the particle surface is formed. The *near-field* on one particle can interact with that of an adjacent particle, leading to oscillation coupling, which is the basis of the enhancement phenomena of the SERS [58].

The field enhancement occurs twice. Initially, the field enhancement magnifies the intensity of incident light, which excites the Raman modes of the molecule being studied, consequently increasing the signal of the Raman scattering. The Raman signal is then further magnified by the same mechanism as the incident light was, resulting in a larger increase in the total output signal of the experiment.

The enhanced local field inside a sphere (E_{loc}) with an applied electric field (E_{inc}) is calculated by solving Laplace's equation with proper boundary conditions at the surface of the sphere:

$$E_{loc} = E_{inc} \frac{3\varepsilon_m}{\varepsilon + 2\varepsilon_m} \quad , (10)$$

where ε is the dielectric function of the sphere and ε_m is the dielectric function of the medium [59]. The two-process emission of Raman radiation near a metallic nanoparticle can be described as follows [60]:

1. Excitation of the molecule. The excitation field is enhanced with respect to the incident field due to the resonance behavior of the inner field in the particle; its increase is then given by the enhancement factor derived from Equation 10, $3\varepsilon_m(\omega_i)/(\varepsilon(\omega_i)+2\varepsilon_m)$, where ω_i is the frequency of the incident light.
2. Emission from the molecule. The emitted field is, again, enhanced by the resonance of the metal particle by $3\varepsilon_m(\omega_R)/(\varepsilon(\omega_R)+2\varepsilon_m)$, where ω_R is the frequency of the Raman-scattered light.

Hence, the total enhancement factor for scattered intensity, ρ, is

$$\rho(\omega) = \left| \frac{E_{loc}(\omega_i)}{E_{inc}(\omega_i)} \frac{E_{loc}(\omega_R)}{E_{inc}(\omega_R)} \right|^2 = const. \left| \frac{\varepsilon_m(\omega_i)}{\varepsilon(\omega_i)+2\varepsilon_m} \frac{\varepsilon_m(\omega_R)}{\varepsilon(\omega_R)+2\varepsilon_m} \right|^2 \quad (11)$$

The dielectric function of the sphere is given by

$$\varepsilon(\omega) = \varepsilon_1(\omega) + i\varepsilon_2(\omega) = 1 - \frac{\omega_p^2}{\omega^2+\Gamma^2} + i\frac{\omega_p^2}{\omega(\omega^2+\Gamma^2)} \quad , (12)$$

where ω is the laser frequency and $\omega_p = (ne^2/\varepsilon_0 m_e)^{1/2}$ is the Drude plasma frequency. The relaxation constant, Γ, can be related to the electron mean free path l by $\Gamma = v_F / l$, where v_F is the Fermi velocity. For $\omega >> \Gamma$, the real and imaginary parts of $\varepsilon(\omega)$ for free electron metals can be written as

$$\varepsilon_1(\omega) = 1 - \frac{\omega_p^2}{\omega^2} \quad , \quad \varepsilon_2(\omega) = 1 - \frac{\omega_p^2}{\omega^3}\Gamma \quad (13)$$

Since $\omega_i - \omega_R << \omega_i$, ω_R, one can substitute $\varepsilon(\omega_i) \sim \varepsilon(\omega_R)$ in Equation 11; thus the enhancement is given by

$$\rho(\omega) = const. \left| \frac{\varepsilon_m(\omega_i)}{\varepsilon(\omega_i)+2\varepsilon_m} \right|^4 = const. \left| \frac{\varepsilon_1^2 + 2\varepsilon_1\varepsilon_m + \varepsilon_2^2 + i2\varepsilon_2\varepsilon_m}{(\varepsilon_1+2\varepsilon_m)^2+\varepsilon_2^2} \right|^4 \quad (14)$$

The enhancement is maximized at a frequency where the denominator, $(\varepsilon_1 + 2\varepsilon_m)^2 + \varepsilon_2^2$, is minimized. The condition for maximum enhancement is fulfilled for a negative ε_1 (that also determines the resonance position together with ε_m) and a small damping (small ε_2) at the resonance frequency. Note that with small spherical metallic particles, the second denominator in Equation 14 also appears in the expression for the optical absorption cross section.

A comparison between the enhancement of gold and that of silver reveals higher enhancement of the latter for two reasons [50]. The first one is the difference between the dielectric functions of the two metals. At the range of the surface plasmon frequency of silver, ε_2 is small enough to enable a sharp resonance. In contrast to silver, the resonance of gold does not coincide with the minimum ε_2 as a result of high damping; this in turn results in less pronounced resonance.

The second reason concerns the resonance position of silver. In most metals the spectral dependence of ε_1 is derived from a free electron mode. However, in the case of noble metals such as silver and copper, the situation is different. The inter-band transition from the 4d to the 5sp band of these metals approaches the surface plasmon energy and shifts it from the free electron value to about 3.6 eV. As a result, the surface plasmon resonance of silver has contributions from both the *d* and the conduction electrons. This results in a better coupling to light at the visible regime, and in a larger enhancement [60]. From the above, it is obvious that the field enhancement of silver nanoparticles is much larger than that of gold; thus silver nanoparticles are much more commonly used in SERS measurements.

Surface Plasmons

In 1908 Gustav Mie developed a complete analytical solution of Maxwell's equations for the scattering of electromagnetic radiation by spherical particles [61]. Mie applied Maxwell's equations with appropriate boundary conditions in spherical coordinates using multiple expansion of the incomimg electric and magnetic fields. Mie's theory yielded the *far-field* and *near-field* scattering and extinction cross sections far away from a spherical particle.

This chapter deals with the aspect of the nanoparticles' size and its effect on the surface plasmon properties. The mathematical description can be divided into two regimes: small and large nanoparticles.

The regime of small nanoparticles (λ>>2R) is called the *quasi-static* regime. In this regime, the phase shifts (retardation effects) of the electromagnetic field over the diameter of the nanoparticle are negligible. This means that the generally multipolar excitations of Mie's theory are restricted to the dipolar mode. The optical properties of small spheres in the *quasi-static* regime are illustrated in Figure 8a by comparing the extinction (Q_E), absorption (Q_{ABS}), far field scattering (Q_{SCA}), and near-field (Q_{NF}) scattering efficiencies for a small silver sphere (22 nm) [62]. In this regime, the four spectra are simple and peak at the same wavelength that satisfies the dipolar surface plasmon resonance condition.

However, large spheres are beyond the *quasi-static* regime; in this case, retardation and multipole surface plasmon resonances must be taken into account. The wavelength dependencies of Q_E, Q_{ABS}, Q_{SCA}, and Q_{NF} for a large sphere (100 nm) are shown in Figure 8b. The depicted spectra are considerably more complicated and do not all peak at the same wavelength. Moreover, additional peaks (500 and 380 nm) appear in the spectra, and the peak associated with dipolar surface plasmon resonances is pulled to a longer wavelength (406 nm). In fact, this peak decreases significantly in magnitude compared with that of the small sphere peak.

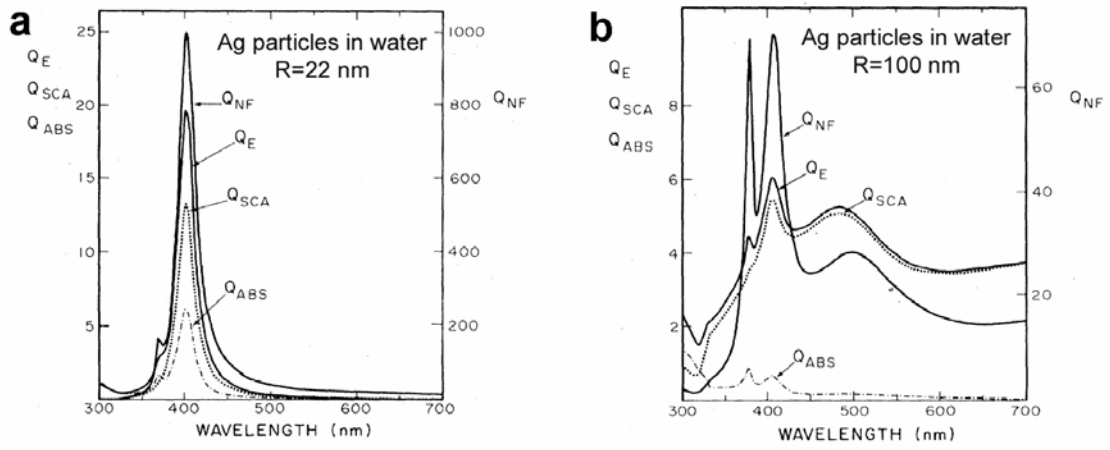

Figure 8: Scattering efficiencies for silver spheres of a) a 22-nm radius and b) a 100-nm radius immersed in water [62].

The effect of nanoparticle coupling

A minimalist model for a SERS hot spot is a junction formed between two nanoparticles, as created in a dimer structure. Why is a junction between two nanoparticles a hot spot? As two nanoparticles approach each other, the *near-field* on one particle interacts with that on an adjacent particle, coupling the surface plasmon

oscillations together. This coupling yields a significantly stronger *near-field* in the junction, compared with that around a single particle (larger by as much as 5 orders of magnitude) [58, 63].

In order to qualitatively explain phenomena related to nanoparticle coupling, I will use a simple dipole-dipole interaction model, as shown in the scheme of Figure 9 [64]. Because of the confinement of the plasma electrons in the nanoparticle, the electric field of the irradiated light creates surface charges (Figure 9a). When another particle is nearby, the positive charges of the left particle face the corresponding negative charge of the right particle. Because of the attractive forces between these two particles' distributions of charges, the resonance frequency of this mode is lowered and a red shift occurs. One would expect that the red shift would be larger as the coupling of the two spheres becomes stronger, manifested by the distance between the two spheres decreasing [60, 64-68]. In contrast, when the driving field is normal to the long axis of the dimer (Figure 9c), the dipole-dipole interaction is repulsive. Thus, the resonance frequency of this mode is raised and blue shifts.

Indeed, Jain *et al.* showed experimentally that under parallel polarization, the surface plasmon resonance red shifts as the interparticle gap is reduced: a shift of 80 and 25 nm occurs when two gold disks are separated by 2 and 12 nm, respectively (Figure 10) [68]. Conversely, they showed that there is a very weak blue-shift with a decreasing gap for orthogonal polarization.

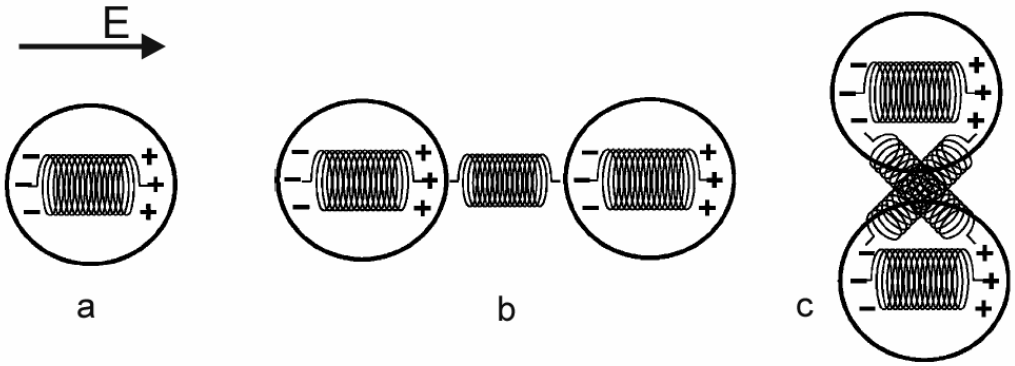

Figure 9: Schematic illustration of the electromagnetic interaction between closely spaced nanoparticles, a) an isolated particle, b) a dimer with the polarization of the incident field parallel to the long particle pair axis, and c) orthogonal to the long axis of the dimer [64].

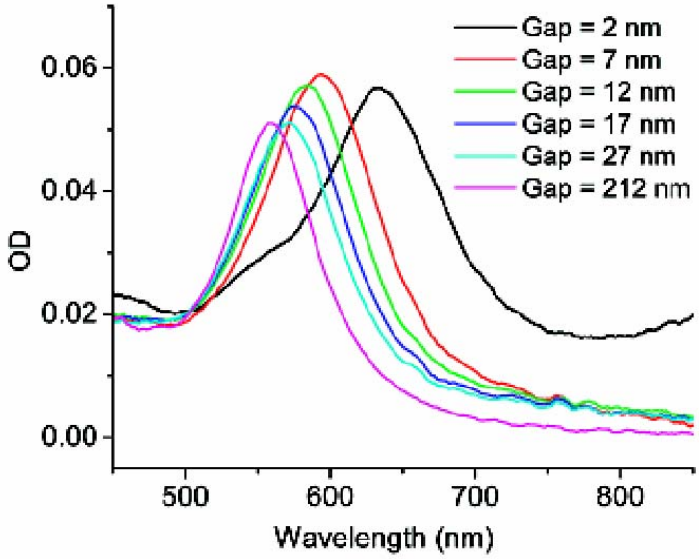

Figure 10: Absorption of gold nanodisc dimers for varying the inter-particle separation gap for incident light polarization in a direction parallel to the inter-particle axis [68].

The polarization effect of the incident field with respect to the dimer long axis on the *near-field* was calculated, as shown in Figure 11 [69]. The *near-field* variation is highest at the junction between the two particles. It is enhanced tremendously for polarization parallel to the dimer axis (Figure 11a) and is excluded from the inter-particle region for perpendicular polarization, as shown in Figure 11d.

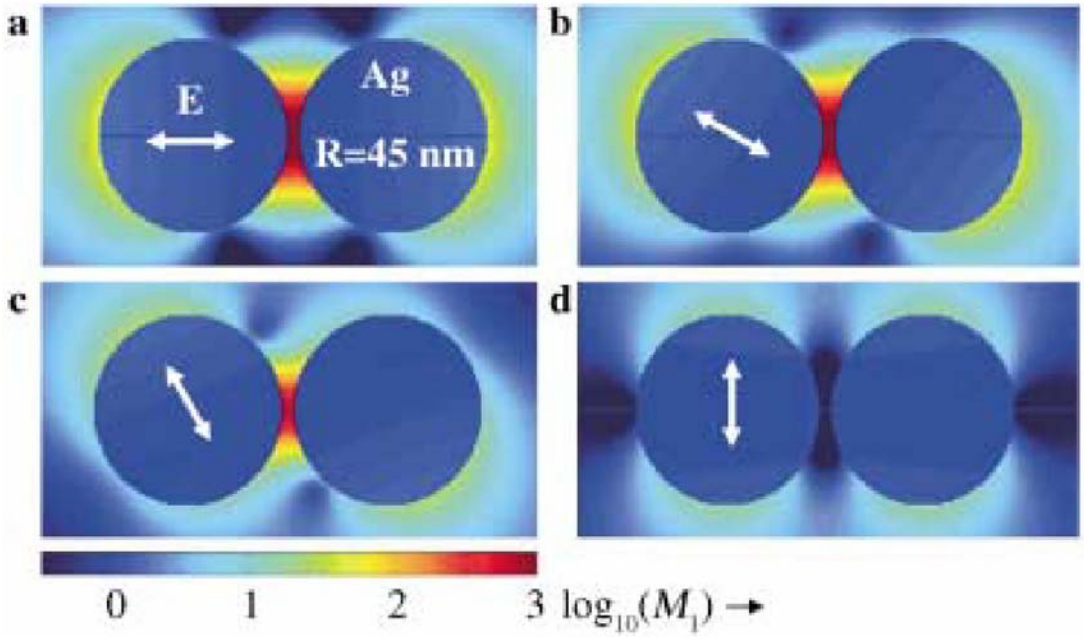

Figure 11: Local intensity enhancement $(E_{loc}/E_0)^2$ in logarithmic scale versus incident polarization [69]: a) 0°, b) 30°, c) 60°, and d) 90°. The arrows represent the different polarizations. The intensity is color coded, with red and blue depicting high and low intensity, respectively.

When discussing SERS enhancement of a molecule in a dimer structure, all the considerations mentioned above should be taken into account. According to Equation 11, the electromagnetic enhancement is the product of a gain at the incident laser frequency times a gain at the Raman frequency. A maximum SERS signal is expected to occur when both frequencies approach the surface plasmon resonance frequency [70]. Thus, the shift of the resonance has a strong influence on the SERS signal intensity. We will see later, in the results section, that polarization of the excitation with respect to the dimer axis greatly affects the SERS enhancement. Moreover, a surface plasmon shift caused by the nanoparticles' size also has an enormous effect on the SERS enhancement and potentially can be used to tune it.

Recently, there has been an effort to correlate the SERS response with specific individual structures of nanoparticles. In some of these studies, several methods were used such as atomic force microscopy (AFM), transmission electron microscopy (TEM), scanning electron microscopy (SEM), and optical traps [63, 71-75].

The first attempt to observe the effect of coupled nanoparticles on the SERS enhancement in real time was done by Svedberg *et al.*, who used optical tweezers to manipulate a single nanoparticle toward an immobilized one and simultaneously measured the SERS spectrum of molecules adsorbed on it [74]. They found that as a nanoparticle moves closer to an immobilized one, the SERS signal increases to the maximum of a factor of 22, owing to dimerization.

Additional experimental evidences for enhancement by dimeric structures are revealed in a study by Hongxing *et al.*, who used hemoglobin molecules adsorbed on Ag nanoparticles to study the source of SERS enhancement [75]. They found that most of the SERS signal was obtained from dimer and trimer structures.

Talley *et al*. also measured and calculated the SERS intensity originating from individual nanoparticles and dimeric nanoshells [63]. Utilizing AFM, they found that the highest intensity SERS corresponded to dimeric structures. Moreover, the Raman response for isolated Au nanoparticles was not observable. The measured SERS intensities of the dimeric structures varied greatly, probably because of the random orientation of the dimeric structures with respect to the polarization of the incident light.

1.3 The dimer approach for single-molecule measurements

My thesis is divided into two parts. The first part presents transport through single molecules, and is devoted to understanding the effect of the degree of conjugation on the molecular conductance. Part Two explores SERS of single molecules, and the mechanism underlying the SERS enhancement. Both parts are based on the dimer approach for measuring single molecules.

In the introduction, several methods for measuring single molecules were introduced. Although these methods are quite successful in measuring molecular transport, they provide little control over the number of molecules bridging the gap, or the properties of the metal-molecule contact. We propose a novel method (the scheme is shown in Figure 12a) for contacting molecules by combining a "top down" approach for creating electrodes with a separation of a few tens of nanometers, with a "bottom up" approach that consists of connecting a single molecule between two metallic nanoparticles (this construct is called a *dimer*) [76].

In the first part, transport measurements of the dimers are performed (Figure 12b). To bridge the gap between two electrodes, the dimer is trapped between them by modifying the electrostatic trapping method, and measurements are made using conventional transport techniques. This method provides us with the technological advantage of a straightforward way for creating many electrodes using a parallel processing technique, combined with the experimental advantage of a well-characterized, controlled way of connecting a single molecule to well-defined gold contacts. Furthermore, it provides a straightforward way to gate the molecules and to perform temperature-dependent measurements.

In the second part, I show that dimer structures are not only attractive for conductance measurements on single-molecule devices - they could also serve as efficient antennas that greatly enhance the electromagnetic field at the center of the dimer, where the molecule resides. Thus, dimers provide a basic experimental model for studying the fundamentals of SERS enhancement, which are not well understood (Figure 12c).

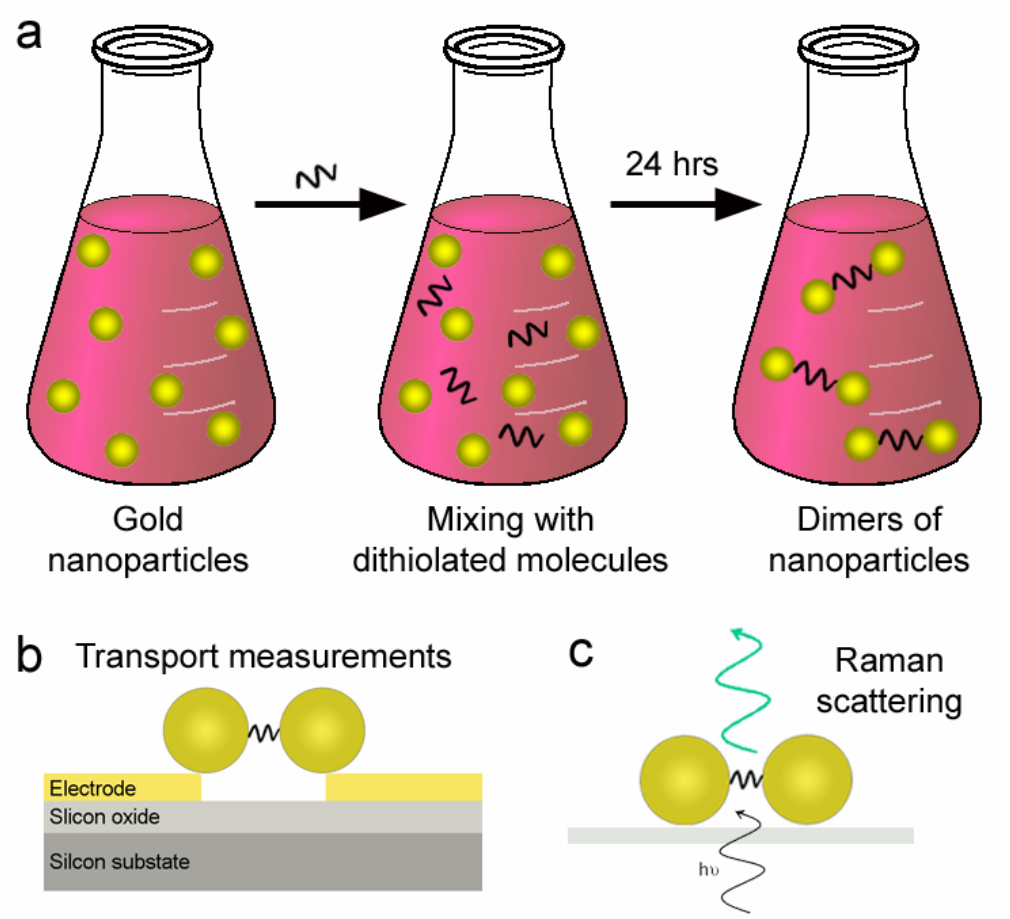

Figure 12: a) Schematic representation of the dimer method. We start with a solution of gold nanoparticles that are then mixed with dithiolated molecules to form dimers. b) The transport measurement configuration. The dimers are positioned between two close electrodes, and the conductance of the molecules is measured. c) The SERS experiment scheme. The dimers are excited with light, and the scattered Raman spectrum of the molecules is collected.

2. Electron transport through single molecules

2.1 Experimental

2.1.1 Creation of Dimer structures

a) Synthesis of gold colloids

Colloidal gold nanoparticles with a diameter of 30 nm were prepared using a method described by Grabar *et al*. with slight modifications [77]. Briefly, a solution of "seed colloids" (2.6 nm in diameter) was prepared by adding 1.0 ml of 10mg/ml aqueous $HAuCl_4 \bullet 3H_2O$ to 100 ml of double distilled water (DDW) while stirring. One minute later, 1.0 ml of 10 mg/ml aqueous Na_3citrate was added followed, 1 minute later, by 1.0 ml of freshly prepared 0.75 mg/ml $NaBH_4$ in 1% Na_3citrate, and the mixture was stirred for 5 min.

Larger colloids, 30 nm in diameter, were prepared by adding 0.2 ml of 10 mg/ml Na_3citrate and 130 μl of the Au "seed colloids" solution to 50 ml of boiling aqueous solution of $HAuCl_4 \bullet 3H_2O$ (0.1 mg/ml) while stirring. Refluxing was continued for 10 min, or until a change to a reddish color was observed. The solution was cooled to room temperature and stored in a dark bottle at 4°C. A typical absorption spectrum of gold nanoparticles in solution is shown in Figure 13a. By measuring the absorption of particle solutions of different concentrations, a calibration curve can be achieved by a series of dilutions (Figure 13b) and is followed the Beer-Lambert law:

$$A = \alpha l C \quad (15)$$

where A is the absorption, l is the distance that the light travels through the material, C is the concentration of the sample. The absorption coefficient α is given by $\alpha = 4\pi k / \lambda$ where k is the extinction coefficient and λ is the wavelength of the light. From the calibration curve, the concentration of an unknown nanoparticles' solution can be calculated.

This procedure resulted in citrate-stabilized well-dispersed in water gold colloids having a narrow size distribution [78]. The colloids were imaged in a FEI Tecnai T12 transmission electron microscope (TEM) operated at 120KV (Philips). Gold colloid concentration was calculated based on the mean particle diameter measured by TEM and the weight of $HAuCl_4$ used in the reaction [79].

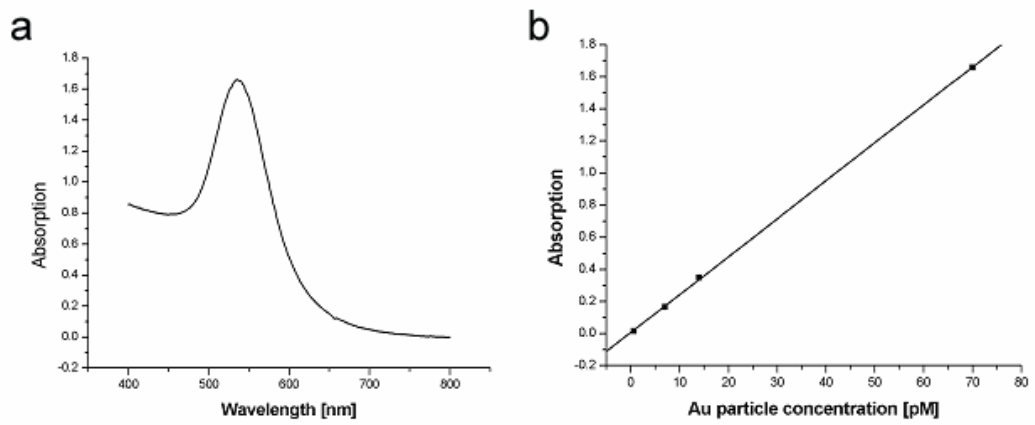

Figure 13: a) Absorption spectrum of 40 nm Au particle solution, b) calibration curve. The absorption value at the maximum wavelength (536 nm) is plotted as a function of the concentration of the nanoparticles.

b) Synthesis of dimer structures

The dimer preparation consisted of several stages. First, the colloidal gold solution was concentrated. This was achieved by centrifuging 10 ml of the solution at $9.7x10^3$g for 5 min and discarding the supernatant. The precipitate was resuspended in 2.5 ml of 1 mM NaOH and centrifuged again as above, leaving about 0.4 ml of concentrated solution. Three molecules were used: 1,4-benzenedimethanethiol (BDMT), 4,4'-biphenyldithiol (BPD), and Bis-(4-mercaptophenyl)-ether (BPE) as shown in Figure 14. The spacer molecules were dissolved (BDMT in DMSO, BPD and BPE in 10 M NaOH) and diluted with 1 mM NaOH to the desired concentration. This solution was mixed with an equal volume of the concentrated colloidal gold solution containing 10-fold molar excess of colloids and incubated for 24 hr at 4°C. The mixture (0.5 ml) was loaded on a 10% - 75% glycerol gradient (using a Gradient Master of Biocomp) in water and centrifuged at 9,000 rpm for 10 min in a Beckman SW41 rotor. After centrifugation, the tube was pierced at the bottom and the solution was extracted from it slowly by pumping 10% glycerol through its top at a rate of 1 ml/min. The solution was divided into different fractions of 0.5 ml each and these were kept at 4˚C until they were ready to be used.

The fractions were characterized by TEM; the fraction that was found to contain the highest percentage of dimers (around 60%) was centrifuged and resuspended in 1 mM NaCl.

Dimers consisting of 10 nm gold nanoparticles were prepared in a similar approach, apart from the separation step that was carried out using a gradient of 10-40% of sucrose.

It turns out that the process of dimer formation is complicated and sensitive to factors that are not well understood by us. In a few cases we were not able to produce dimers for unknown reason. Apparently parameters such as pH, salt concentration, and stabilizing agent of the colloids can affect dimer formation. Further work should be done in order to be able to control the process well. The results in this thesis are based on successful attempts of dimer formation.

2.1.2 Fabrication of electrodes with nanometer size gap

A metal electrode system consisting of source and drain with a minimal gap of 25 nm was formed on a p-type Si substrate with 100 nm SiO_2 on top, using electron beam (e-beam) and optical lithography techniques. A double-layer electron resist system consisting of PMMA 200K (5,000 rpm, 60 sec, baked for 1 hr at 180ºC) and PMMA 495K (8,000 rpm, 60 sec, baked for 1 hr at 180ºC) was used for resist patterning by e-beam writing. A 120 kV electron beam was irradiated on the resist system (Jeol JBX-9300 FS) and the irradiated resist was developed (1 min) using a 1:3 mixture ratio of MIBK (methyl isobutyl ketone) and isopropanol. Subsequently, electron beam evaporation was carried out to form 7 nm Ni and 23 nm Au. The metal films were subsequently lifted-off by soaking the sample in acetone, rinsing it with isopropanol, and drying with nitrogen gas. The e-beam fabricated electrodes were connected to bonding pads defined by photolithography. Image reversal photo resist AZ5214E was used for patterning (spin coating 5,000 rpm, 40 sec, pre-baking at 100ºC for 1.5 min). The wafer and the contact pads' optical lithography mask was aligned and exposed to 415 nm light at 15 mW for 6 sec, then post-baking of 2 min and flood exposure of 1.5 min. The pattern was developed with AZ726 developer for 30 sec. The contact pads were fabricated by thermal evaporation of a Ti (10 nm) adhesion layer followed by 200 nm Au layer and lift off. The electrodes were examined using a scanning electron microscope (SEM) and tested electrically to verify the existence of a gap.

Gating of the samples is allowed by using the Si substrate as a back gate. The contact to the gate is formed by etching holes in the oxide and exposing the silicon in

buffered hydrofluoric acid for 2 minutes, followed by evaporation of a thick aluminum layer (1 μm) and annealing at 460˚ for 30 minutes. This procedure forms Ohmic contacts to the silicon that conduct at 4 degrees Kelvin with a typical resistance of 10-100KΩ at a 1V bias. After annealing a layer of gold is evaporated on top of the aluminum to improve bonding to the pads.

2.1.3 Positioning the dimers between the electrodes

It is crucial that the contact area of the electrodes and the nanoparticles is not contaminated. Thus, prior to positioning of dimers, the electrodes were cleaned from photo-resist traces during the lithography process. The cleaning procedure was as follows: the electrodes were washed with warm acetone and methanol for 5 min each, followed by ozone stripping for 7 minutes at 70ºC. Finally the samples were rinsed in ethanol while stirring gently for 8 minutes. This final step is necessary to remove the unstable gold oxide layer, which is formed during the ozonation process [80]. Failure to remove this layer results in non-conductive samples. After cleaning the samples were taken to a home built probe station, where the electrostatic trapping took place. The probe station used is made of Karl Suss PH150 probes mounted on a platform, which are connected to an arbitrary signal generator (Agilent 3120A) via very short coaxial cables to minimize parasitic capacitance.

Electrostatic trapping was performed in the probe station; a 0.35 μL drop of the dimer solution (containing typically 45-55% dimers, 40-50% single colloids and a few percents of higher conjugates) was placed on the electrodes surface. Next an AC voltage of 800 mV at 10 MHz was applied between the electrodes for 30-90 seconds. The sample was then cleaned in DDW, and blow dried with nitrogen. The devices were tested on the probe station, glued to a 24-pin header with photoresist and the ones that showed conductivity were bonded and measured in a liquid helium container. Bonding was done at room temperature to avoid damage to the trapped molecules by heating. Great care needs to be taken to ground anything that comes in contact with the samples after trapping is complete; the samples are extremely sensitive to electrostatic discharges, which cause the electrode edges to peel near the gap. After the measurement the devices were imaged in a SEM to determine the type of colloidal structure that was trapped.

2.1.4 Transport Measurements

Low temperature (4K) transport measurements were performed by connecting the 24-pin header sample to a rod and dipping it in a liquid helium dewar. Conductance and current were measured simultaneously using lock-in as follows: a small AC signal from a lock-in (EG&G 7260 DSP) was added to the source drain voltage from a DC source (Yokogawa 7651) connected to the source electrode. The drain electrode was connected to a current amplifier (Keithley 428) and from there to a multimeter (HP 34401A) to measure the DC current and back to the lock-in amplifier to measure the in phase response of the molecule to the AC excitation. The frequency of the excitation was chosen to avoid the frequencies, at which the system has much noise, checked with a spectrum analyzer. We measured at 67 Hz, avoiding the 50 Hz frequency of the electric lines and a 15 Hz disturbance found in our system.

2.2 Results

2.2.1 Dimers formation and separation

The dimer synthesis is performed by mixing a solution of dithiolated molecules (schemes shown in Figure 14) with that of gold nanoparticles, keeping their respective ratio below 1:10. The nanoparticles are stabilized with Na_3citrate [77]. In making the bridged nanstructures, the thiols on the bridging molecule displace citrate anions to form a stable Au-S bond [79]. If more than one molecule binds to a certain colloid, trimers, tetramers and higher oligomers can be formed. Based on their relative mass, the dimeric colloids are separated from monomeric colloids and higher oligomers by centrifugation through glycerol or sucrose density gradients. Each structure propagates as a different band along the centrifuged tube, and is easily distinguished because of its reddish color. An example for the separation of different sizes of gold nanoparticles is shown in Figure 15a.

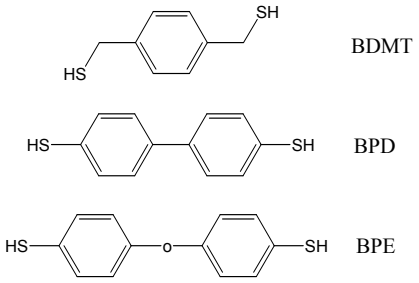

Figure 14: The structure of the three molecules that we studied: 1,4-benzenedimethanethiol (BDMT), 4,4'-biphenyldithiol (BPD), and Bis-(4-mercaptophenyl)-ether (BPE). Synthesis is described in Appendix A.

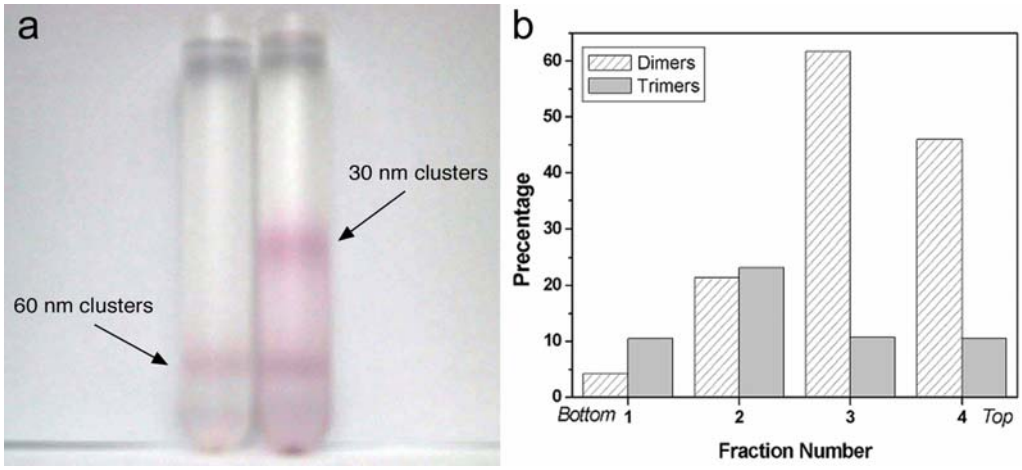

Figure 15: a) Gold colloids of different sizes separated by centrifugation in a glycerol gradient. Right: the upper band is of 30 nm gold clusters, the lower band is 60 nm gold clusters. Left: only 60 nm gold clusters. b) Histogram presentation of the percentage of dimers and trimers observed in the TEM in different fractions along the gradient tube. As a maximum dimer concentration is observed in fraction number 3, the highest trimer content appears at lower fraction.

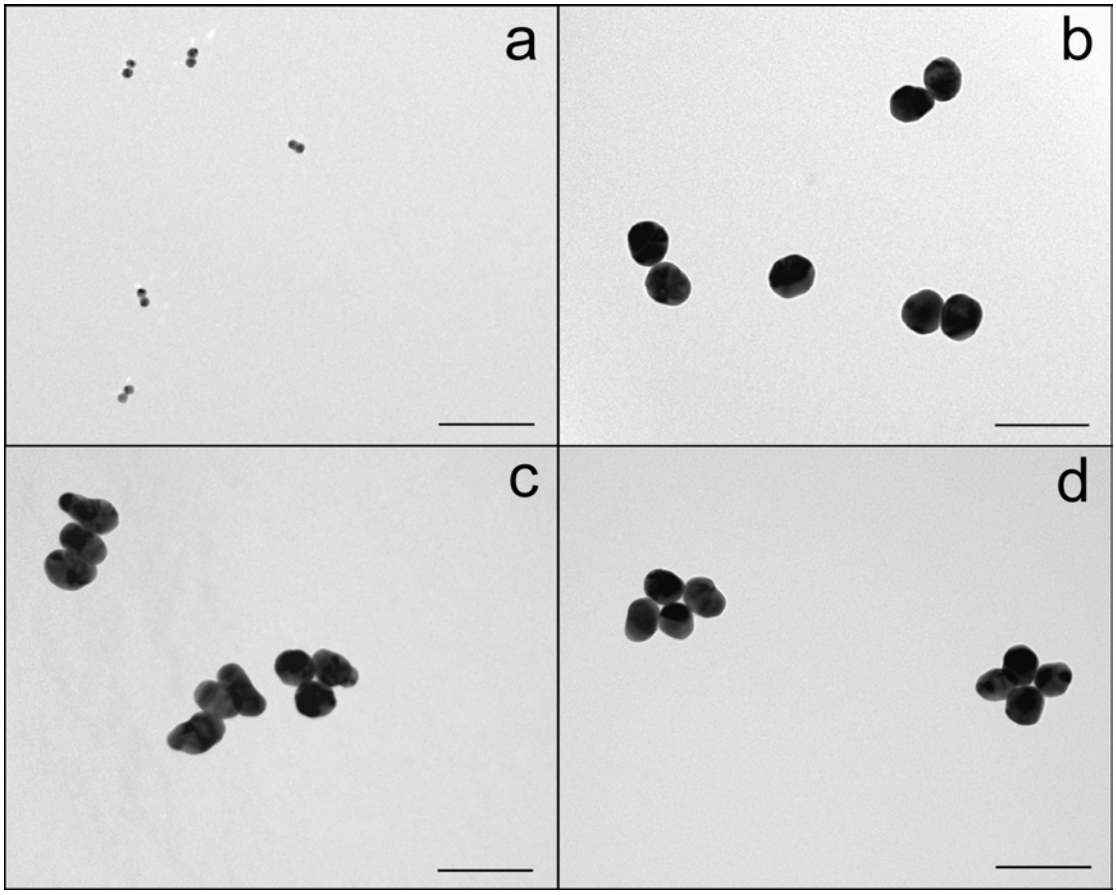

Figure 16: TEM images of gold nanoparticles oligomers of BDMT molecule. a) 10 nm dimers, b) 50 nm dimers, c) 50 nm trimers d), 50 nm tetramers. Scale bar is 100 nm.

Gradients were fractionated and inspected by TEM to select for fractions enriched in dimers (typically 50-60%). Figure 15b shows an example of the dimer and trimer contents in the different fractions along the gradient tube. In fraction number 3 the dimer percentage is the highest (60%), while for trimers the maximum appears in a lower fraction. In order to perform electrostatic trapping of dimers between two electrodes, fraction number 3 is ideal. Representative TEM images of 10 nm and 50 nm nanoparticle dimers and higher conjugates after fractionation are shown in Figure 16.

Figure 17 shows a transmission electron microscope image at higher magnification of a dimer made of two 10-nm gold colloids connected by BDMT that is synthesized in this manner. The gap between the two colloids is readily seen, and its size is in good agreement with the size of the BDMT molecule, which is approximately 0.9 nm.

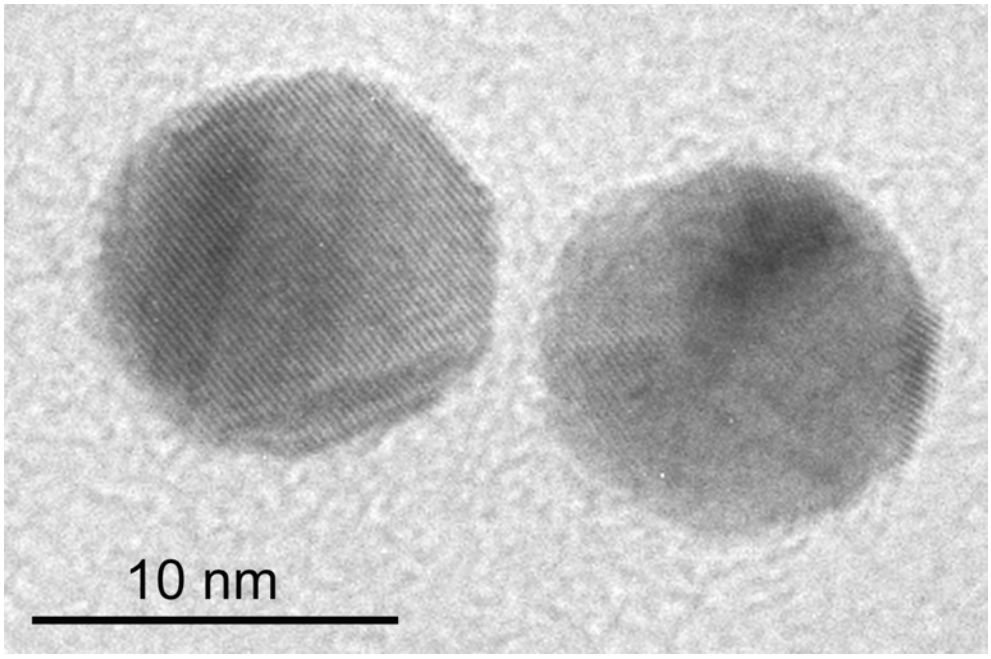

Figure 17: TEM image of a BDMT dimer made of 10 nm gold colloids. The ~ 1 nm separation between the two colloids corresponds approximately to the BDMT length (0.9 nm).

The procedure of dimers preparation is generic, it can be used for any molecule with two clips that can bond to metals, the nanoparticles can be composed of various metals (silver dimers are discussed in the next chapter) and of various size to fit a specific experimental setup. The existence of a single molecule in the dimers is discussed next.

2.2.2 Evidence for single molecule

a) Statistical study

To ensure that most of the dimeric colloids are bridged by a single dithiolated molecule, we use much smaller molecular concentration (C_m) in the reaction mixture with respect to the concentration of the monomeric nanoparticle (C_p). When a molecule meets a nanoparticle, it reacts with the nanoparticle's surface. Since there are more nanoparticles around than molecules, it is most probable that the nanoparticle-molecule conjugate will meet another nanoparticle, and not a molecule, to form a nanoparticle-molecule-nanoparticle structure. If this dimer now meets another molecule a trimer is formed. The second molecule can adsorb on different sites of the nanoparticle's surface thus different shapes of trimers can be formed as shown in Figure 16c.

In the case of low molecular concentration, when the reaction is completed, the ratio of dimers, *R*, to single unbound nanoparticles is expected to follow the relation

$$R = \frac{C_m}{C_p - 2C_m} \quad (16)$$

We measured *R* for different input concentrations of dithiolated molecules, keeping C_p fixed, as shown in Figure 18. We verified the significance of these results by applying the χ^2 test. This statistical test examines what is the population size one should sample in order to get statistical significance. For example, in order to distinguish between two populations of 5% dimers and 10% dimers, with a confidence of 95%, one should sample 480 objects from each population [81]. For that reason, each point in the graph represents the results of 700-900 nanoparticle counts. Figure 18 shows that the relation represented in Equation 18 holds for C_m:C_p ratios that are lower than 1:10. For that reason, this ratio was used to the preparation for single molecule dimers.

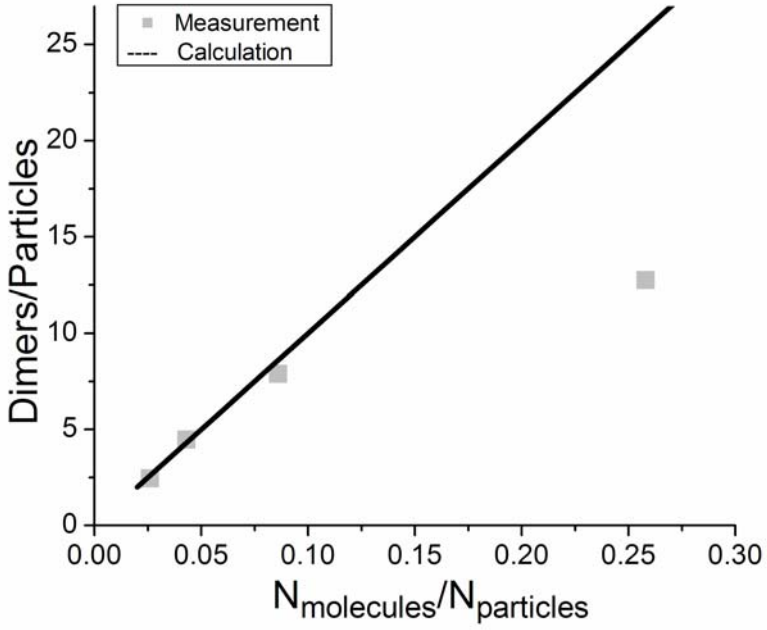

Figure 18: Dimer content as a function of molecules added to the nanoparticles solution. Up to a ration of 1:10 molecules:nanoparticles there is a good match with the prediction of a single molecule per dimer.

b) SERS of dimers

To further establish the presence of a molecule in the dimer we conducted Raman scattering measurements on dimers with silver nanoparticles [75]. This experiment is

discussed in great details in sections 3.2.3 and 3.2.4. The main results of the experiment are a clear Raman spectrum of the molecule originating from the dimer structure, and the characteristic of temporal blinking of a single molecule.

2.2.3 Electrostatic trapping

In order to perform conductivity measurements of the molecules, we position the dimer in between two electrodes using the method of electrostatic trapping [33, 82-84]. By applying a voltage between the electrodes a dipole moment is induced in the nanoparticle, as a result, it is attracted to the point of strongest electric field, i.e. the gap between the two electrodes, by dipole-dipole interaction (Figure 19).

The gold electrodes are defined on a silicon substrate with a thin (25-100 nm) oxide layer using electron beam lithography (Figure 20) with a minimum gap of 25 nm. The oxide layer operates as a barrier between the conductive Si substrate and the gold electrodes; it allows applying a gate voltage up to 40V without any noticeable leakage. The substrate can thus be used as a back gate to control the conductance through the system in a standard single electron transistor configuration.

In most of our studies we use dimers with 30 nm diameter gold colloids. Hence, the electrodes are made with 40-50 nm separation, which is below the dimer size and larger than the single colloid diameter. The electron beam lithography electrodes are first cleaned to remove metal oxide from the surface [80] and then inserted in a probe station where the electrostatic trapping is performed.

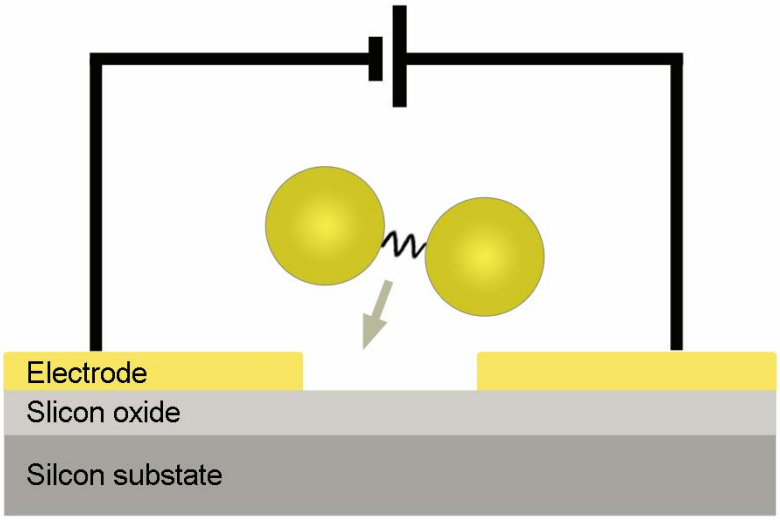

Figure 19: Schematic representation of the electrostatic trapping method.

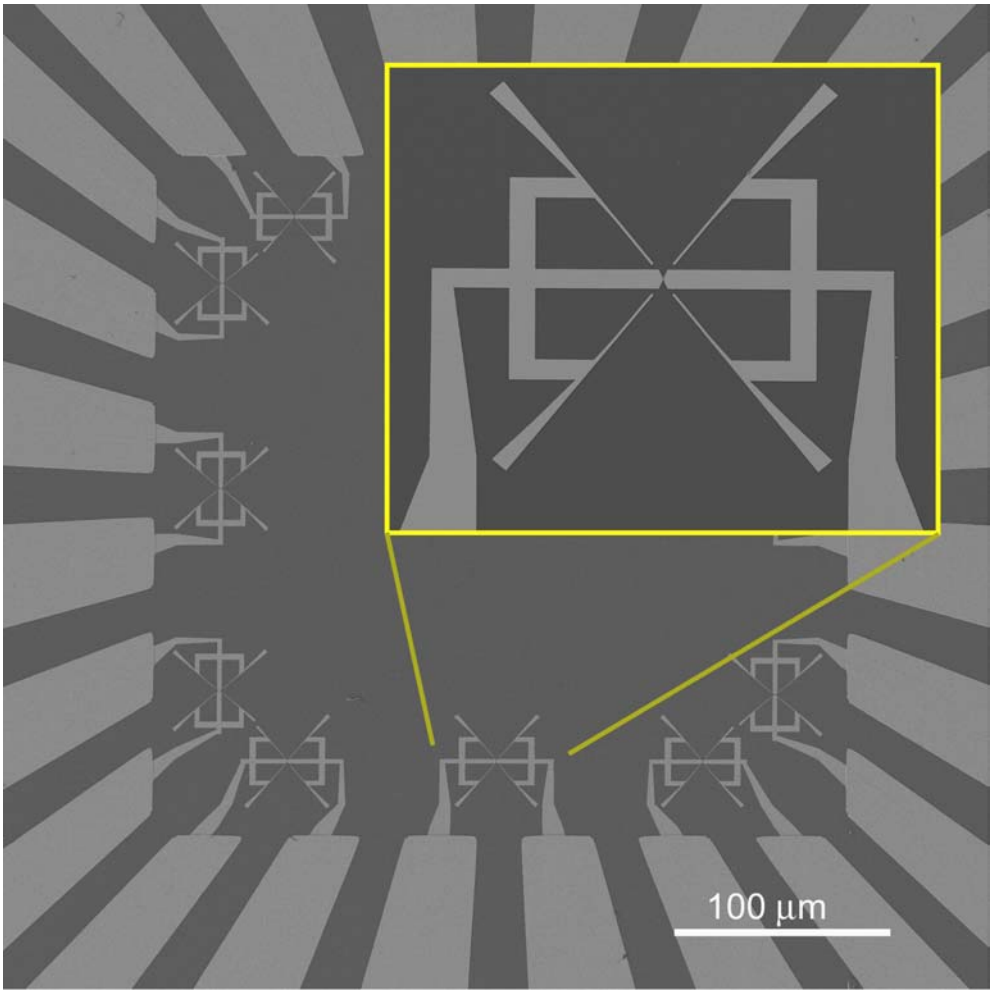

Figure 20: SEM image of the electron-beam electrodes design. Twelve gold electrode pairs are pattered on p-type Si wafer with a silicon oxide on top.

We first determined the parameters for single nanoparticles' trapping. We studied the effects of DC voltage, AC voltage, frequency, and trapping time on the trapping process using a solution of 40 nm Au nanoparticles at a concentration of 70 pM. Trapping nanoparticles by applying DC voltage was done by Bezryadin *et al.* [33]. In our case DC voltage caused the nanoparticles to be attracted to one of the electrodes as shown in Figure 21a. This is a result of the negative charge of the gold nanoparticles that leads to an attractive Coulomb force to the negative electrode rather than to the gap. We overcome this undesired effect by applying an AC voltage between the two electrodes [84].

An additional difficulty arises from the induced motion of fluid near the electrodes caused by the existence of electric field. The non-uniform field along the electrode causes the ion double layer on top (from the solution) to flow in a direction that

prevents them to reach the electrode gap. The fluid flow near such electrodes has been shown by Ramos et al. [85] to be frequency dependent usually reaching a maximal value in the KHz range, and decaying after that, the effect of this motion can be seen in Figure 21b-d. When the frequency is increased the nanoparticles are better attracted to the central region in between the electrodes, giving the best results at f = 50 kHz. The number of trapped particles is also determined by the gap size. When the gap between the electrodes is larger than the particle's size, more than one particle is bridging the electrodes. Figure 22 shows a trapping of a single nanoparticle.

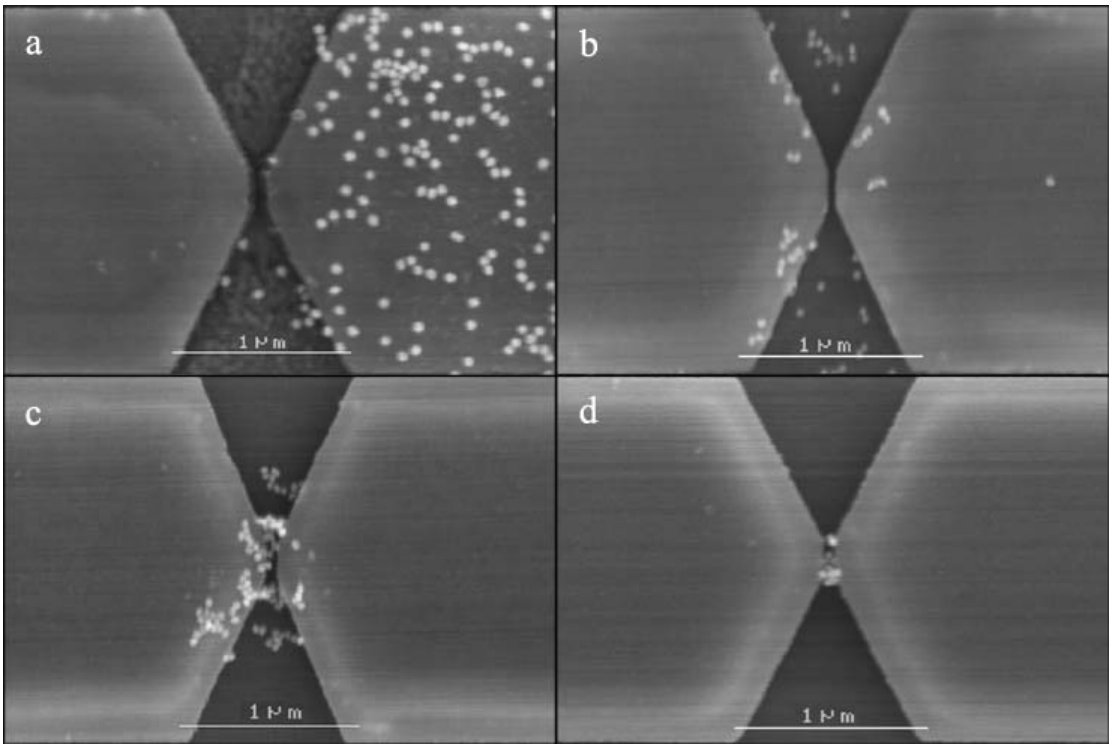

Figure 21: SEM images of trapped Au nanoparticles under various trapping conditions a) DC trapping. b) AC trapping at 2 V and 1 kHz. c) AC trapping at 2 V and 10 kHz. d) AC trapping at 2 V and 50 kHz.

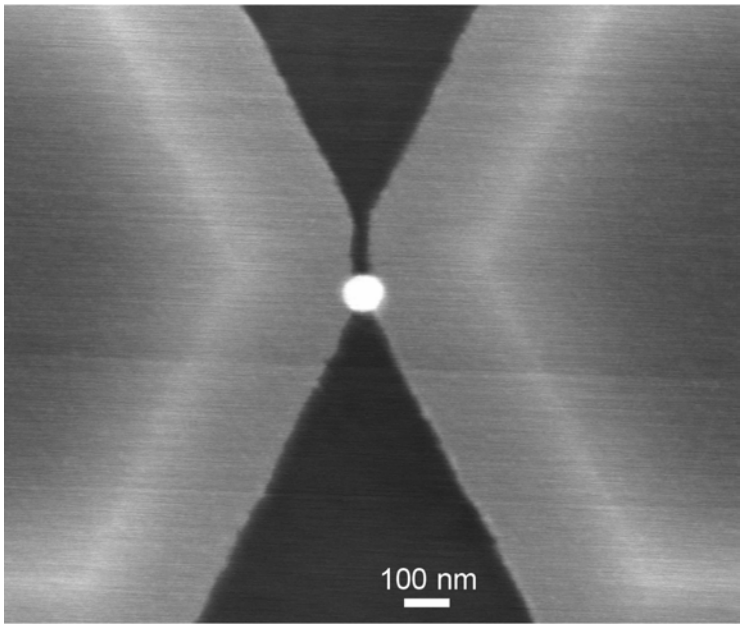

Figure 22: SEM image of nanoparticle of 60 nm in diameter trapped between two electrodes.

We also found that for applied voltages well below V=800mV no particles are attracted to the gap, for all tested frequencies and trapping times up to several minutes. At a voltage of V=800mV, nanoparticles start to appear in the vicinity of the gap. This indicates that there is a threshold value in electric field strength, which may depend on the viscosity of the liquid and the size of the particles.

We used the same method to trap dimers. The AC field causes the dimers to align their long axis, with the larger dipole moment, with the electrodes. We have found that this effect is more pronounced the higher the frequency of the applied trapping voltage, up to a frequency of 10 MHz.

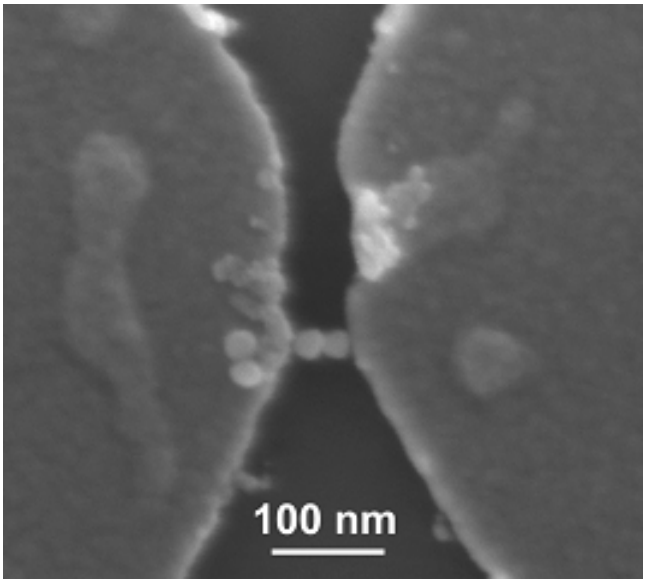

Figure 23: SEM image of a dimer trapped between two electrodes.

Due to the two effects of directionality and the double layer flow we chose to use a frequency of 10MHz, were we have been able to obtain effective trapping with as little as 800mV applied to the electrodes, and a good alignment of the dimers with respect to the gap as can be seen in Figure 23.

The trapping parameters (voltage, frequency and time) of dimers differ slightly from one dimer batch to the other, as a result of the concentration and the viscosity of each dimers solution. Therefore we tuned the trapping parameters for each batch and observed the samples in the SEM. The success rate of the electrostatic trapping was relatively high, and reached ~50% when the impedance of the dimer solution was high enough, such that the dipole-dipole interaction between the electrodes and the colloids was not screened. An analysis of the trapping events reveals that in 55% of the cases the gap is bridged by one colloid only. In 45% of the cases we get a dimer between the two electrodes (Figure 23): In 35% the conductivity is too low to determine the conductance features (10^{-10}-10^{-11} Siemens). We find in SEM imaging that the brightness of the gold nanoparticles of these dimers is low (Figure 24), probably due to a poor conductivity between one of the colloids to the electrode [86]. In 10% of the trapping events we obtain high conductivity dimers (~10^{-8} Siemens).

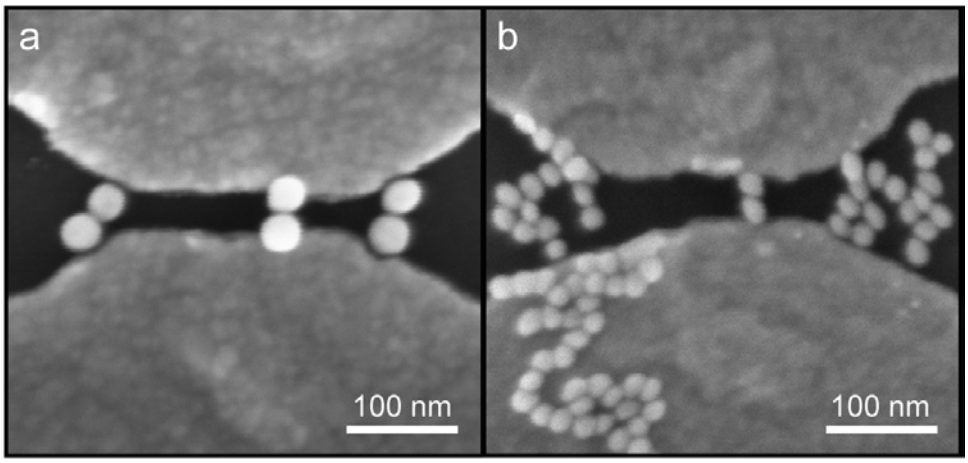

Figure 24: SEM images of bright and dark dimers, a) A bright dimer that conducted a current of 7 nA at 1V source drain bias. b) A trapped dimer and few other aggregates, all dark, that conducted a current of 100 pA at 1V.

2.2.4 Measurements of single nanoparticles

Measuring the conductance of single nanoparticles between two closely spaced electrodes allows us to study the characteristics of the contacts with the advantage that the physics of this system is well understood. Since the nanoparticles are covered by stabilizing citrate molecules (to protect from aggregation), a full contact with the

leads is prevented. Thus, electrons must tunnel to get from one electrode to another. This configuration is known as a single electron transistor (SET).

Transport measurements of single nanoparticles were performed for two sizes of nanoparticles, 10 and 40 nm in diameter. Au nanoparticles of 40 nm were trapped and measured using electron-beam defined electrodes (Figure 20). In the case of 10 nm nanoparticles we used different electrodes configuration because the resolution limit of the electron-beam lithography could not produce such small electrode gaps. In this electrode configuration, the gap size was determined by the thickness of a molecular beam epitaxy (MBE) grown layer embedded in a sandwich structure (Figure 25). This layer is selectively etched and after metal evaporation a gap is formed where the layer was removed; gaps of 10 nm were produced [82]. The different geometry of the two types of electrodes causes the capacitances of the particles to the leads to be different. As a result, different charging energies of the particles and conductance values are observed. However the general phenomena of scaling of the charging energy with particle size should be the same for both configurations.

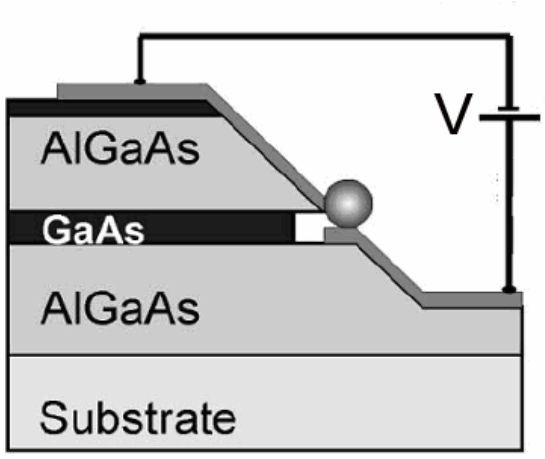

Figure 25: Schematic illustration of electrodes with nanoscale gaps: a mesa structure is defined by optical lithography and wet etching followed by selective etching of the GaAs layer, and metal evaporation of the electrodes [82].

Transport through a 10 nm Au nanoparticle positioned on a mesa electrodes configuration, at 4.2 K is presented in Figure 26. A clear *Coulomb blockade* behavior was observed at $V_{bias} \approx \pm 25$ mV, a Coulomb staircase is seen at higher voltages with a period of approximately 50 mV. This period fits with a capacitance of approximately 3aF, which is five times larger than the self-capacitance of a sphere of this size $C=4\Pi\varepsilon_0 R \approx 0.6$ aF. The difference is due to the fact that the capacitance defining the steps is the total capacitance including the capacitance to the electrodes.

Asymmetry in the I-V curve was observed, for positive bias voltage we find a linear rise in current at a range of 25mV<V_{bias}< 65mV, whereas for negative bias we observe a step-like feature at V_{bias}=-25 mV, which then saturates in a linear slope. This asymmetric behavior has been discussed by Hanna and Tinkham [87] assuming different tunnel resistances to the electrodes. The inset in Figure 26 shows transport measurement of another sample at different temperatures. At 4.2 K we found the *Coulomb blockade* region to be larger than in the previous sample. Clearly, also at higher temperature (77 K) a nonlinear behavior was observed.

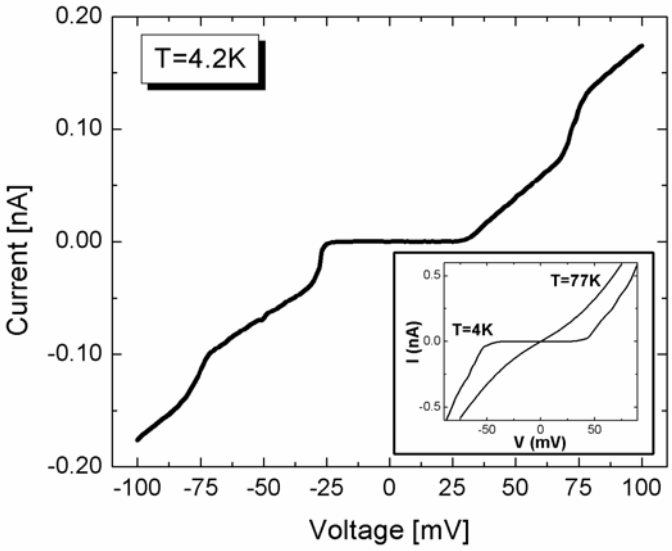

Figure 26: I-V curve of a single 10 nm Au trapped nanoparticle measured at 4.2 K. The asymmetry with respect to positive or negative V_{bias} , i.e., a linear onset at 25 mV and a step like onset at 65 mV, results from an asymmetry in tunnel resistances to the electrodes. The inset shows experimental $I-V$ curves for different temperatures of another sample.

Measurements of a single Au nanoparticle of a size of 40 nm trapped between electron-beam electrodes with a gap of 40 nm at 4.2 K give mostly ohmic behavior with a resistance of 1 kΩ. However, in some cases a nonlinear behavior is observed. Figure 27 shows *I-V* and dI/dV curves measured on a trapped 40 nm Au single nanoparticle on the electron-beam electrodes device at 4.2 K. A much smaller *Coulomb blockade* is observed compared to the 10 nm nanoparticle, up to $V_{bias}\approx\pm$10mV, in agreement with the expected Coulomb energy for a cluster of this size (C≈4.4 aF)). Step-like features are observed in the dI/dV plot, with periodicity of $V_{bias} \approx$ 20 mV.

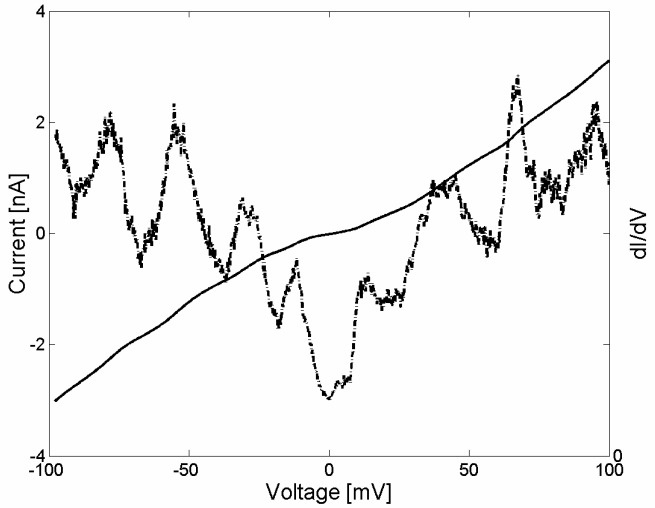

Figure 27: I-V and dI/dV curves of a single 40 nm Au trapped cluster measured at 4.2 K. The solid line corresponds to the I-V curve and the dashed line to the dI/dV curve. The asymmetry with respect to positive or negative V_{bias} (easily observed by the peaks of the dI/dV) is a result of an asymmetry in the tunnel resistance R_1 and R_2 to the electrodes.

Gating the devices was achieved by applying a voltage to the substrate. Plotting the conductance in the $V_{sd} - V_g$ plane produces a diamonds structure of a SET (Figure 3). In Figure 28 diamond plots of two different devices are presented. Figure 28a corresponds to a nearly identical input and exit tunnel barriers. Figure 28b shows a skewed diamond structure seen as a set of parallel lines, corresponding to different input and exit tunnel barriers.

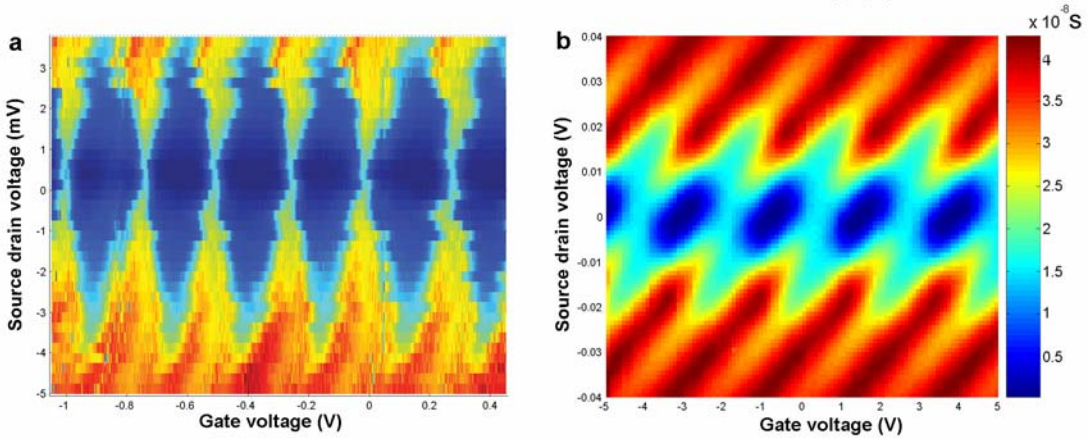

Figure 28: Measurements of the conductance of single nanoparticles shown in the V_{sd}–V_g plane. The conductance is color coded, with red and blue depicting high and low conductivity, respectively. a) The familiar diamond structure is seen, corresponding to a nearly identical input and exit tunnel barriers. b) A skewed diamond structure seen as a set of parallel lines, corresponding to different input and exit tunnel barriers. The different charging energies of the two are due to the different size of the colloids (Equation 4): 40 nm diameter in (a) and 30 nm in (b).

2.2.5 Transport measurements through single conductive molecules

Effect of conjugation

The electrical conduction through three short organic molecules, whose structure is depicted in Figure 29, was studied. The three molecules consist of benzene rings and two thiol groups that allow contacting the Au nanoparticles. However, they differ by their conjugation level in the following way: 4,4'-biphenyldithiol (BPD) is a fully conjugated molecule, Bis-(4-mercaptophenyl)-ether (BPE) in which the conjugation is broken at the center by an oxygen atom, and 1,4-benzenedimethanethiol (BDMT), where the conjugation is broken near the contacts by a methylene group. The samples that we refer to in the following sections are: 15 BPD devices, 13 BPE devices and 15 BDMT devices.

The electrical transport measurements through the dimer structures are performed using an AC voltage with amplitude of a few mV superimposed on a DC voltage, and the current as well as the differential conductance (*dI/dV)* are measured simultaneously. Figure 29 shows a comparison of the differential conductance of the three molecules at 4.2 K. These are representative curves from more than ten devices of each of the molecular species that were studied. The BPD dimers clearly show a series of conductance peaks. These peaks cannot be attributed to charging of the gold colloids – their typical spacing is a few hundred mV, more than an order of magnitude larger than the gold nanoparticles charging energy. In fact, in some cases we could resolve the *Coulomb blockade* oscillations superimposed on the large conduction peaks (see Figure 30). The oscillation period is very similar to that observed in a single colloid measurement (see comparison at the previous section). We note that the conductance through a single trapped nanoparticle is substantially higher than that of a dimer, typically by one to two orders of magnitude. Hence, the tunnel barriers between the metal electrodes and the gold colloids act as a small series resistance, carrying only a minute fraction of the applied voltage, while most of it drops on the molecule.

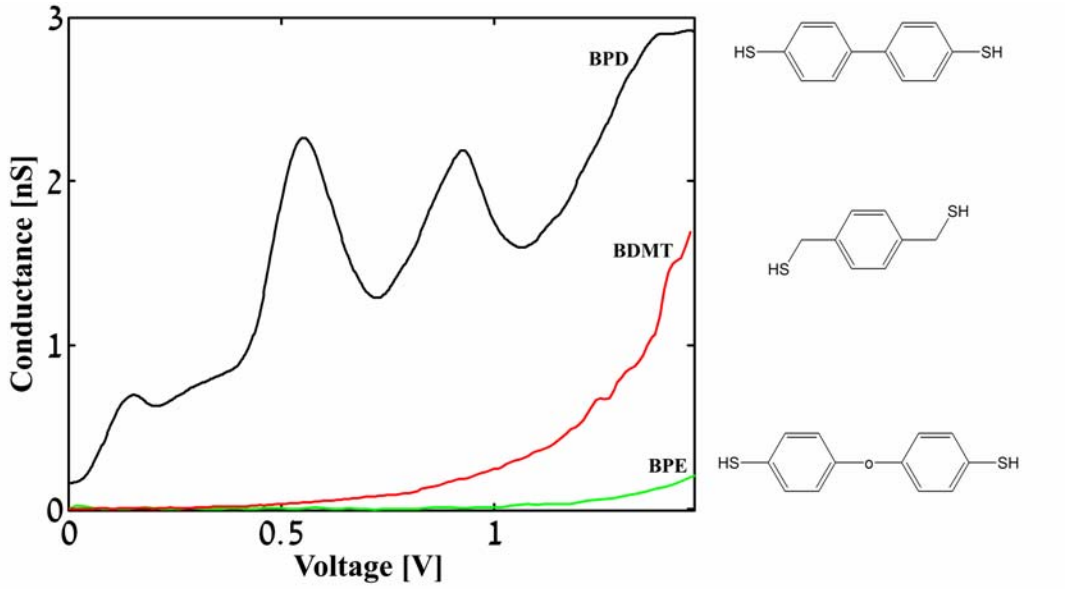

Figure 29: Differential conductance as function of voltage measured for dimers of BPD, BDMT and BPE dimers at 4.2 K.

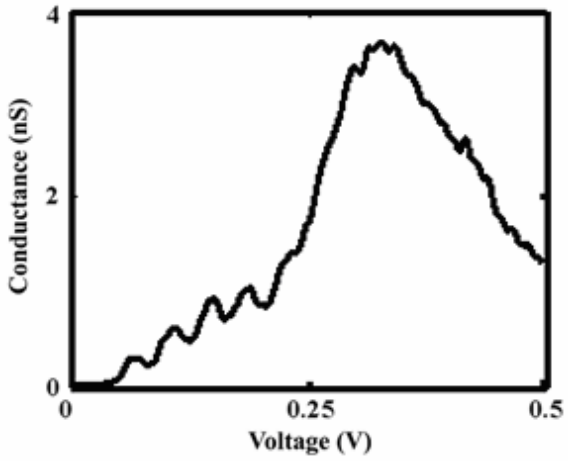

Figure 30: *Coulomb blockade* oscillations of the gold nanoparticles which are superimposed on the conduction peak of the BPD measured at 4.2 K.

Adding localizing groups to the molecule is expected to suppress its conductivity as discussed in the introduction. Indeed, the BPE and BDMT dimers show remarkably different behaviors. It is clearly seen that the conduction through the dimers formed from these molecules turns on at much higher voltages (typically larger than 0.5V) and one cannot resolve any peak structure. The systematic difference between the three molecules that is related to their conjugation further confirms that the measured differential conductance is of molecular origin. The apparent gap and exponential turn-on of the differential conductance in the case of the BPE and BDMT suggest that adding localizing groups interferes with the conjugated aromatic system and suppresses the overall conductance through the molecule. This assertion is nicely

demonstrated when comparing the BPE with the BPD molecule, where the addition of an oxygen atom between the conjugated rings suppresses the conductance almost entirely below 1V. A similar effect takes place in the BDMT dimers where the methylene groups suppress the overlap of the molecular backbone orbitals with the contacts [88].

Recent calculations compared the conductivity of the three molecules, BPD, BDMT and BPE as shown in Figure 31. These calculations, done by using greens function method, are with qualitative agreement with our measurements in terms of the relative conductivity of the three molecules; BPD has the highest conductivity followed by BDMT and BPE. On the other hand the peaks in this calculation are spread significantly more than in our measurements. The units used are of e=h=c=1, meaning that the current is in the range of 10^{-7}A, about an order of magnitude higher than that typically observed in our measurements.

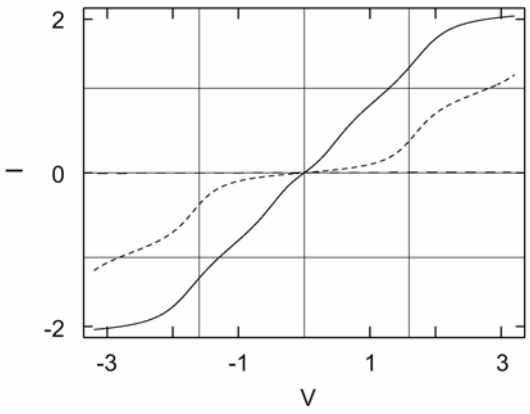

Figure 31: Calculations of the current as a function of applied voltage for BPD (solid line), BDMT (dotted) and BPE (dashed), from Santanu Maiti [89].

Random gating of BPD

Focusing on the peak structure of the BPD dimers we find that while the main features of the conductance spectrum are highly reproducible, there are temporal fluctuations as well as variations between different devices. Figure 32a shows a compilation of 130 measurements of the conductance of one dimer taken over a period of a few hours. Strong temporal fluctuations in peak position, which could be as large as a few hundreds mV, are evident. We find that the conductance spectrum shifts rigidly, namely – all peaks at positive and negative voltages move to the same direction by approximately the same value. This is demonstrated in Figure 32b, where we shift all spectra such that their peaks at -0.2V coincide. It is seen that this

operation causes all other peaks to be aligned as well. Such behavior is typical of electrostatically gated *Coulomb blockaded* systems with different input and exit capacitances as discussed in the introduction [25]. Plotting the conductance in the V_{sd}-V_g plane one obtains a skewed diamonds structure (see Figure 28). It can be seen that under these conditions the conductance peaks at positive and negative drain-source bias indeed move rigidly upon application of a gate voltage. Since the gold nanoparticles are very effective in screening the effect of remote potentials we conclude that charge movement in close vicinity to the molecule gives rise to the observed rigid shift of the spectrum. These temporal fluctuations can therefore be considered as evidence for gating of the molecule, which occurs randomly. We note that the temporal frequency of this random gating depends on the voltage sweep rate, *dV/dt*, and the voltage range of the measurement. It could be substantially minimized by working at low sweep rates and within a limited voltage range, such that stable and reproducible measurements can be conducted over hours.

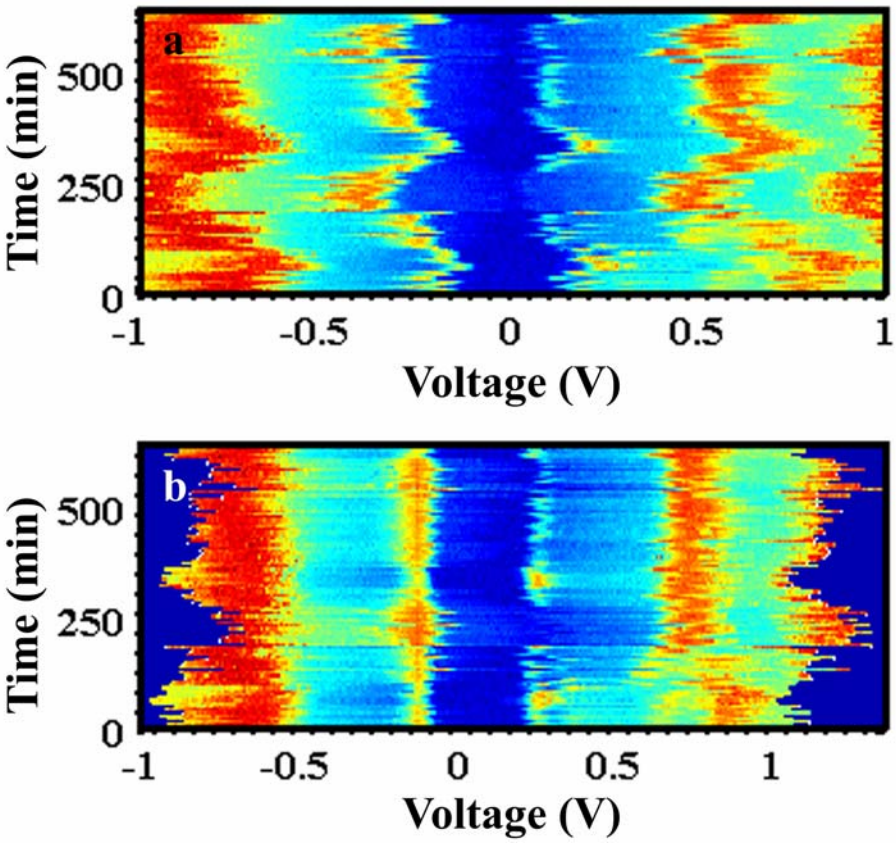

Figure 32: Temporal fluctuations and temperature dependence of the dimer conductance. a) A compilation of 130 measurements of the differential conductance spectrum of one BPD dimer, taken over a period of a few hours. The conductance values are represented by a color scale, which changes from blue (0 nS) to red (3 nS). b) The spectra of Figure 18a shifted such that their peaks at - 0.2 V coincide, thus demonstrating the rigid shift nature of the temporal fluctuations.

Reproducibility of the transport through BPD

Comparing the conductance of 15 BPD dimer-based devices shows that the variations between devices in the peak position and their relative strengths cannot be explained only as a rigid shift. This is demonstrated in Figure 33a, which compares the spectra of two BPD dimers. We can see that while the main features appear at approximately the same voltages, one cannot align the two spectra by a simple shift operation. We note also that there are differences in the value of the conductance between the various devices, which can be as large as an order of magnitude. To statistically quantify this variability we construct a histogram of peak positions (Figure 33b). This is done by converting each spectrum to a set of peaks, each represented by a block of unit height, a width which is the full width at half maximum, and is centered on its maximum. A rigid shift of each spectrum was allowed to accommodate the temporal fluctuations. It is seen that the peak structure survives the averaging over many molecules, indicating that the variability in peak position is smaller than the peak spacing.

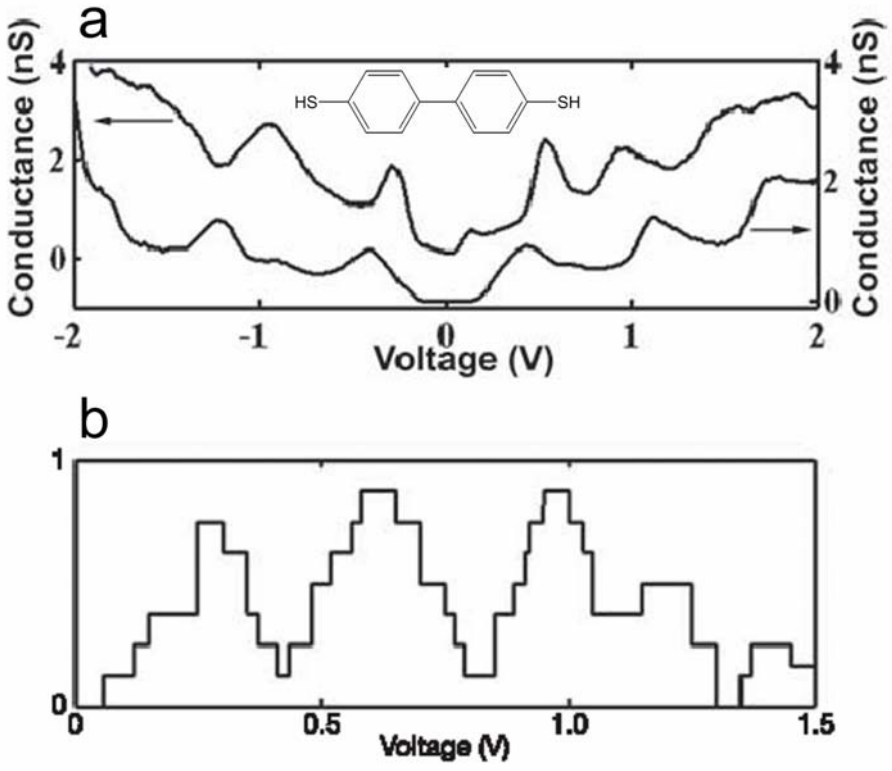

Figure 33: The reproducibility of the conductance spectra measurements of different BPD dimers. a) Comparison of the differential conductance spectrum of two different BPD devices (The upper curve is shifted upwards for clarity). b) Histogram of the conductance peak positions collected from nine BPD devices. Each spectrum was converted to a set of peaks of unit height and a width which is the full width at half maximum. A rigid shift of the spectrum by up to 50 mV was allowed.

The peak positions determined from the histogram agree very well with measurements done on self assembled monolayers of BPD shown in Figure 34a [90]. However, such agreement is lacking when comparing the measured spectra with recent calculations of molecular conduction [29, 91]. In particular, the measured turn-on voltage is significantly lower than theoretically predicted, and the conductance peak positions appear a higher voltage, as shown in Figure 34b. Moreover, the predicted conductance is several orders of magnitude higher than observed.

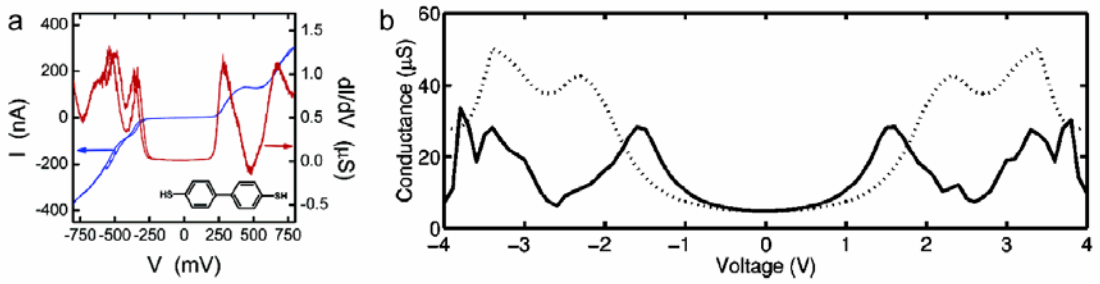

Figure 34: a) Conductance and current as a function of applied voltage of BPD at 4.2K measured by Lee *et al.* [90]. b) Calculated conductance as a function of voltage for BPD molecule, done by Xue *et al*. [29]. The dotted line is obtained assuming the transmission-energy to be bias independent.

3.Surface-enhanced Raman scattering of dimers

3.1 Experimental

3.1.1 SERS experimental setup and measurement routine

A Raman spectrometer was used for performing SERS measurements (Figure 35). Samples were mounted on an inverted microscope (IX70, Olympus) and were excited using a CW frequency-doubled Nd^{2+}-YVO_4 laser operating at 532 nm (Coherent, Verdi). Some experiments were carried out utilizing a 488-nm laser (CW). The laser beam was expanded by means of a long-focal length lens and directed to the sample through a 100x NA=1.3 oil immersion objective. The back-reflected scattered light was collected by the same objective lens and passed through a dichroic mirror (540dclp, Chroma) and a long-pass filter (hq545lp, Chroma), which was used to discriminate the Stokes scattering from the Rayleigh scattering. Next, the light was focused on the entrance slit of the spectrograph attached to a side port of the microscope. A resolution of 10-20 cm^{-1} was achieved using a diffraction grating of 600 grooves/mm, which was enough for our purposes. The spectra were collected by a thermoelectrically cooled CCD camera.

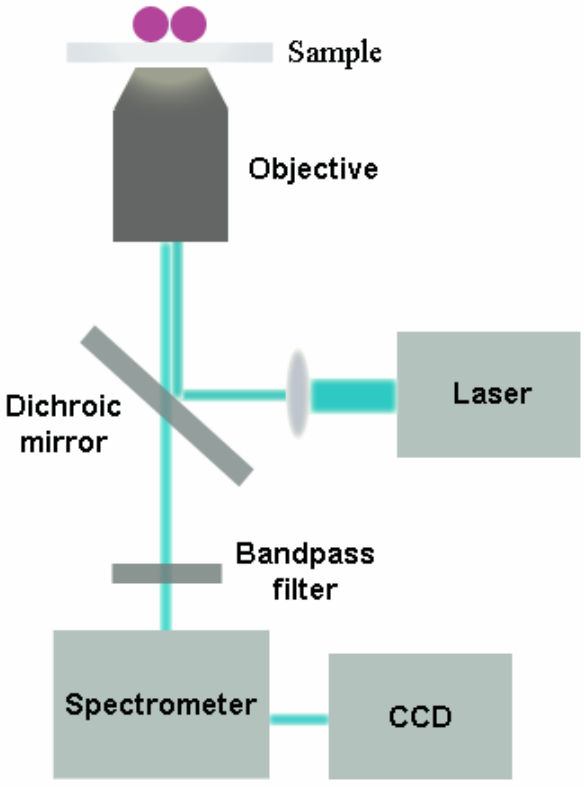

Figure 35: SERS experimental setup.

3.1.2 Raman measurements

Raman measurements were performed by using FT-Raman (Bruker Optics) with Nd:YAG laser source at 1064 nm.

3.1.3 Silver colloid synthesis

a) Lee-meisel colloids

This procedure is very common for synthesizing silver nanoparticles for SERS experiments [92]. Briefly, 50 ml of a 1-mM solution of $AgNO_3$ in DDW was boiled under reflux, followed by adding 1 ml of 1% aqueous Na_3citrate, dropwise with vigorous stirring. The reaction was stirred under reflux for 1.5 hours.

It was impossible to control the size of the nanoparticles produced by this method. As shown in Figure 36, the average size of the resulting nanoparticles does not exhibit a clear dependence on the amount of sodium citrate added. Furthermore, two synthesis reactions performed under the same conditions may give particles whose average sizes differ by more than 10 nm. Characterization of the nanoparticles was carried out using TEM. The size distribution of the particles is usually very broad (a standard deviation of more than 20%), and particles of different shapes and even rods were obtained under these solutions.

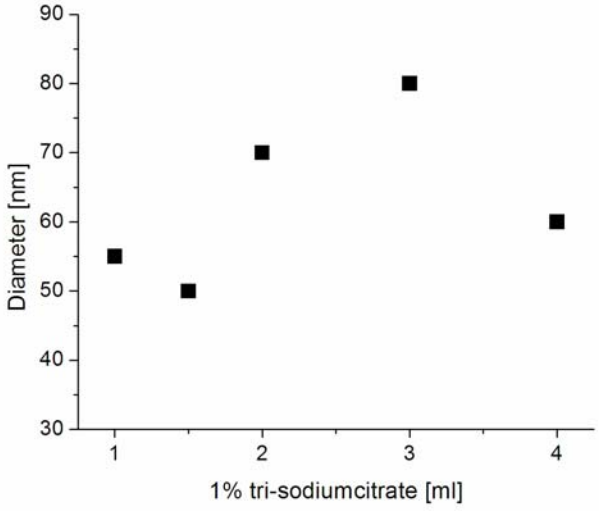

Figure 36: Diameter of silver nanoparticles as a function of the amount of 1% Na_3citrate used in the reaction.

b) Gold-silver core-shell nanoparticles

Nanoparticles of narrow size distribution were prepared utilizing a two-step synthesis method. In the first step, mono-dispersed gold seeds were synthesized [93], followed by a second step of silver shell growth on top of the gold cores.

Synthesis of gold seeds: The procedure of Slot and Geuze [93] for preparation of gold nanoparticles is very reproducible. The nanoparticle diameter is controlled by the amount of tannic acid added to the reaction, as shown in Figure 37, and can be in the range of 5-19 nm. Briefly, a solution containing 1 ml of 1% $HAuCl_4$, in 79 ml of DDW (solution A) and a solution containing 4 ml of 1% Na_3citrate, 16 ml of DDW, and varied amounts of 1% Tannic acid (solution B) were each heated to 60ºC. Next, solution A was added to solution B while stirring. After a change of color to red, the solution was boiled, cooled to room temperature, and stored in a dark bottle at 4°C. To obtain 13- and 18-nm gold nanoparticles, 50 and 10 µl of tannic acid, respectively, were added to the reaction. The typical standard deviation of the nanoparticle diameters was below 10%.

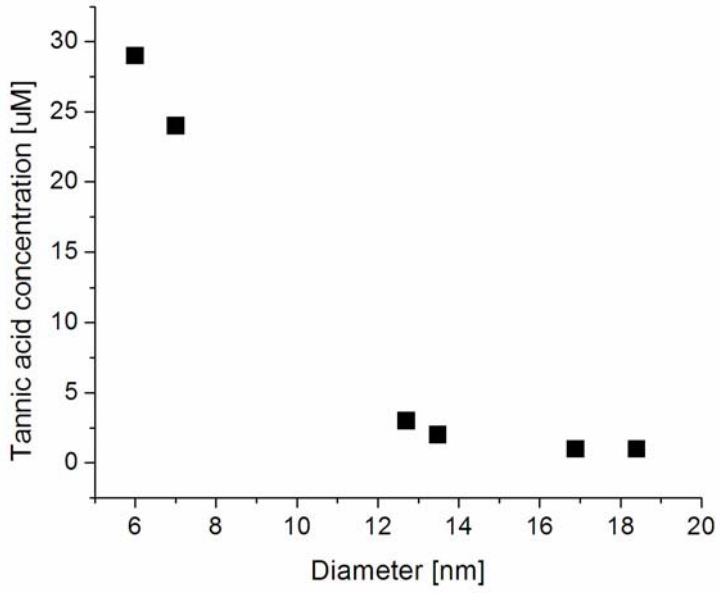

Figure 37: Diameter of gold nanoparticles as a function of Tannic acid in the reaction.

Silver shell growth: The shell width was controlled by the amount of gold seeds and $AgNO_3$ in the reaction. A solution containing 50 ml DDW and a varied amount of 1% $AgNO_3$ (Table 1) was heated to 70ºC in a reflux setup while mixing. Then, the gold seeds solution was added. When the temperature reached 70ºC again, 4 ml of 1% Na_3citrate was added. The reaction solution changed its reddish color to yellow after

20 minutes. The nanoparticles were characterized in FEI Tecnai F-30 TEM (Eindhoven, the Netherlands) operating at 300 kV. Standard deviations of less than 15% were obtained for the colloid diameters.

Table 1: Reaction Conditions for core-shell synthesis

$AgNO_3$ [mM]	Au Colloids [nM]	Au Core Diameter [nm]	Colloid Diameter [nm]	STD of Overall Diameter [nm]
0.26	1.05	12.7	22	15
0.48	0.95	12.7	17	14
0.24	0.95	12.7	14	13
0.43	0.86	12.7	13	12
0.10	0.95	12.7	10	9
0.76	0.45	18.4	24	13
0.19	0.45	18.4	16	10
0.08	0.45	18.4	12	9

Figure 38 shows representative high-resolution TEM (HRTEM) images of gold-core/silver-shell nanoparticles. The gold core is darker due to its higher atomic number. Element mapping of silver was performed by using energy filtered TEM (EFTEM); detection was performed in the energy range of 377-407 eV (insets of Figure 38). The bright shell indicates that the scattered electrons from that region have the typical energy of silver.

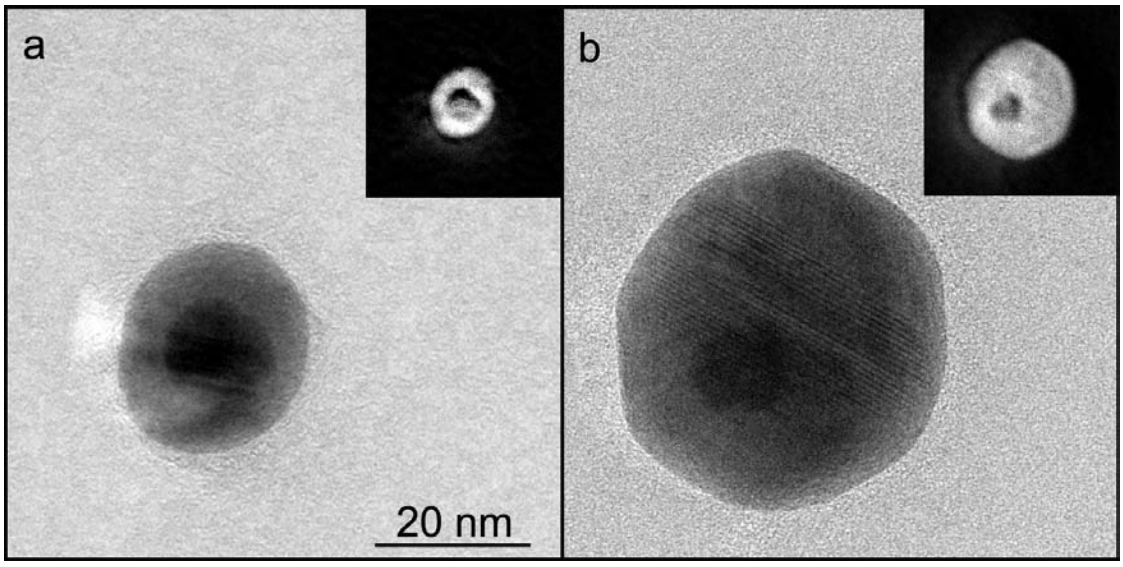

Figure 38: a) TEM images of representative [core-shell] nanoparticles of (a) [12.4, 24] diameter and (b) [12.8, 44], insets: silver maps of the nanoparticles; the bright areas were attributed to silver in the shell region.

c) Linear optical properties

The localized surface plasmon resonance of the nanoparticles strongly depends on their size, shape, and composing materials. Each of these parameters influenced the optical properties that responded to the electromagnetic field. Characterization of the optical properties of the core-shell nanoparticles was performed by measuring the UV/Vis absorption spectra, as shown in Figures 39 and 40.

The local surface plasmon energy (the wavelength at the maximum absorption) of the Au gold core nanoparticles was at 520 nm. However, the maximum of the core-shell nanoparticles ranged from 400 nm to 440 nm (depending on the size). This implies that the optical properties of gold-core/silver-shell nanoparticles are dominated by the silver shell [94], and thus could potentially give rise to a high signal in the SERS experiment. The local surface plasmon energies were red shifted with increasing particle size, from 404 nm to 419 nm for 10-nm and 22-nm nanoparticle radii, respectively. At this regime of nanoparticle dimensions, retardation of the fields across the nanoparticle occurs, which causes a red shift of the local surface plasmon energies with increasing size. The red shift influences the SERS intensity of the molecule, as we will see later on.

The absorption cross section for spherical particles, obtained from Mie theory [60], is expected to linearly depend on the third power of the nanoparticle radius. In Figures 39b and 40b, the maximum absorption of each core series was plotted as a function of the radius cubed. A linear dependence is observed for the two core series.

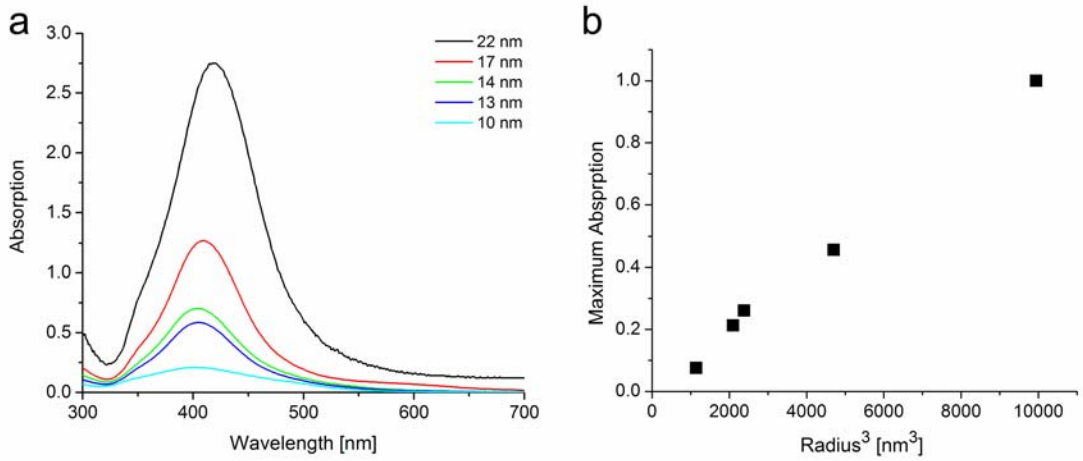

Figure 39: a) Absorption spectra of the core shell nanoparticles with a 12.7-nm Au core diameter, normalized to a concentration of 0.15 nM. b) The extinction coefficient versus the radius of the nanoparticles cubed.

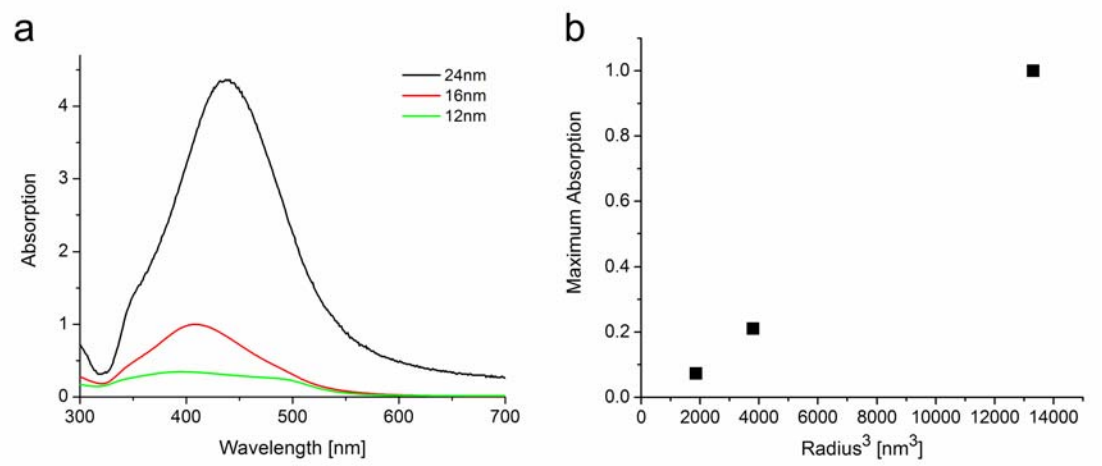

Figure 40: a) Absorption spectra of the core shell nanoparticles with an 18.4-nm Au core diameter, normalized to a concentration of 0.15 nM. b) The extinction coefficient versus the radius of the nanoparticles cubed.

3.1.4 Reaction with dye molecules - Dimer preparation

Silver dimers were obtained for two different molecules (the schemes are shown in Figures 41, 44), Rhodamine 123 (Rh123), and Polythiophene (T4). The T4 molecule was synthesized by Iris Tam from Columbia University [95]. Rh123 was purchased from Sigma.

Preparation of the T4 dimers:

The T4 molecule has two thiol end groups, which are protected in the form of thioesters. Prior to the reaction with nanoparticles, a de-protection step was carried out. A small amount of protected-T4 was dissolved in THF. Next, the thioesters were cleaved by incubation in ammonium hydroxide for an hour. Afterwards, acetic acid was added (equivalent to base) for neutralization. Unprotected T4 solution was diluted in DDW to the desired concentration. It was then mixed immediately with the Ag colloid solution. A mixture of 390 μL of DDW, 10 μL of 100 mM NaCl, and 500 μL 0.2 nM Ag nanoparticles was prepared. Thereafter, 100 μL T4 molecule (0.1 nM) was added and was mixed immediately. In the reaction the ratio of bridging molecules to nanoparticles was maintained at 1:10, respectively, in order to ensure bridges of single molecules. The reaction solution was incubated at 4°C for 24 hours prior to use.

Preparation of the Rh123 dimers:

A small amount of Rh123 was dissolved in ethanol; its concentration was determined by its maximum absorption at 510 nm and its extinction coefficient of 85,000 mol^{-1} cm^{-2}. The Rh123 solution was diluted in DDW to the desired

concentration. The reaction for the formation of silver dimers was as follows: a mixture of 390 μL of DDW, 10 μL of 100 mM NaCl, and 500 μL 0.2 nM Ag nanoparticles was prepared. Next, 100 μL of Rh123 molecule (0.1 nM) was added and was immediately mixed. In the reaction that followed, the ratio of bridging molecules to NA nanoparticles was maintained at 1:10, respectively, in order to ensure bridges of single molecules. The reaction solution was incubated at 4°C for 24 hours prior to use.

The reaction between the molecules and the nanoparticles created oligomers that contain molecules. However, under the reaction conditions that were used, salt was added. This addition was found to increase the probability of the formation of nanostructures such as dimers and trimers due to the reduction of counter ions surrounding the nanoparticles. A statistical study of the dimer content of a solution that contained the Rh123 molecule and of a solution without the molecules, revealed the same dimer content. Thus, apparently under these reaction conditions, the formation of dimers is mostly due to the existence of salt. However, a small fraction of the dimers do contain molecules, which enabled us to perform the SERS measurements.

3.1.5 Sample preparation for SERS measurements

Samples for SERS measurements were prepared using micro cover glasses (Thomas) with dimensions of 18x18 mm and 1.5-mm thickness. Each glass was first washed with ethanol followed by DDW, and then blow dried with air. The glass was then glued to a Teflon holder using nail polish. Polylysine (1 mg/ml) was adsorbed on the glass for 30 minutes and then washed with DDW and blow dried with air. The sample solution was adsorbed for about 10 minutes (while keeping it in darkness), and washed with DDW and then blow dried with air.

3.1.6 Grid substrate preparation

Identifying the source of the SERS hot spots was done using a predefined substrate that was prepared by using optical lithography. Image reversal photo resist AZ5214E was used for patterning (spin coating 5,000 rpm, 40 sec, baked at 100ºC for 5.5 minutes). The glass and the grid's electron beam-defined mask were aligned and exposed to 415-nm light at 15 mW for 5.5 sec, then baked (1 minute at 120ºC) and

flood exposed for 1.5 min. The pattern was developed with developer AZ726 for 25 sec, followed by thermal evaporation of a Ti (5 nm) adhesion layer and a 200-nm Au layer and lifted off.

The reaction solution was prepared according to section 3.1.3, followed by a mild centrifugation step in order to enrich its content with dimers (to about 30%). Polylysine (1 mg/ml) was adsorbed on the glass for 30 minutes and then washed with DDW and blow dried with air. The sample solution was adsorbed for about 10 minutes (while keeping it in darkness), and washed with DDW and blow dried with air. The sample was coated before the SEM with a 2-nm layer of titanium to increase the quality of the SEM images by avoiding excessive charging by the electron beam.

3.2 Results

3.2.1 SERS measurements of single T4 and Rh123 molecules:

a) Comparison between Raman and the SERS spectrum of T4 and Rh123

Choosing the right molecule for a controlled SERS measurement is not straightforward. On the one hand, a resolved spectrum with distinguishable peaks of the molecule is essential; on the other hand, the quantum efficiency should be high. These two requirements are relatively easy to achieve with the available off-the-shelf molecules. However, for our experiments, a molecular clip, which is located on both ends of the molecule, with a high affinity for bonding to silver nanoparticles, is essential. Such molecules could not easily be found. Nevertheless, after an extensive search, we used two different molecules for this study, which are shown in Figures 41 and 44.

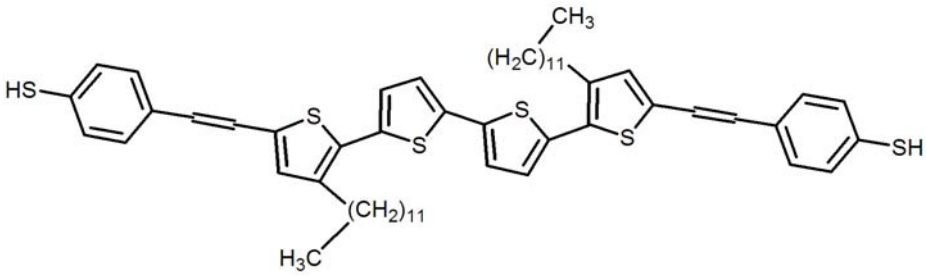

Figure 41: The chemical scheme of the oligothiophene molecule (T4)

The first molecule we investigated was T4, which contains four thiophene rings in series connected to thiolated benzene at its two thiol ends. The molecule was designed to have two dodecane chains on two of the thiophene rings in the series, as shown in the scheme of Figure 41. This molecule is fully conjugated and its thiols provide the bonding group to a silver nanoparticle.

We measured the SERS spectrum (an adsorbed molecule on silver nanoparticles) and the Raman spectrum of the T4 molecule (the free molecule), as shown in Figures 42 and 43, respectively. It has been shown that small differences between the free and adsorbed molecule are expected, due to the different environment the molecule experiences [96]. However, it can be seen (Table 2) that the pronounced modes of the adsorbed molecule (1444 and 1482 cm^{-1}) and of the free molecule (1455 and 1489 cm^{-1}) are well correlated. These vibrations originate from inter-ring collective motions in which C-C skeletal bonds participate. In the normal modes of 1444 and 1455 cm^{-1}, the contribution of the S atom of the thiophene ring is significant. The other mode is assigned as the effective conjugation coordinate mode that results from the linear

combination of the C-C and C=C skeletal bonds involved in the delocalization path of the π-electrons [97].

Table 2: A Comparison between SERS and Raman spectrum

SERS peaks [cm^{-1}]	Raman peaks [cm^{-1}]
1390	1381
1411	1443
1444	**1455**
1482	1489
1548	1534
1586	1591
	2200

The major difference between the free molecule and the SERS spectra is the additional peak of the free molecule at 2200 cm^{-1}. This peak probably originates from the acetyl-S groups that protect the thiols (to prevent di-sulfide formation); they were removed prior to the SERS measurements of T4. Moreover, the peak of the thiol groups in the adsorbed molecule should probably move to a lower energy level as a result of bonding to the relatively heavy silver atoms. However, this low-energy peak is very close to the energy of the excitation laser and does not appear in the SERS spectrum in Figure 42, due to laser cutting by the notch filter.

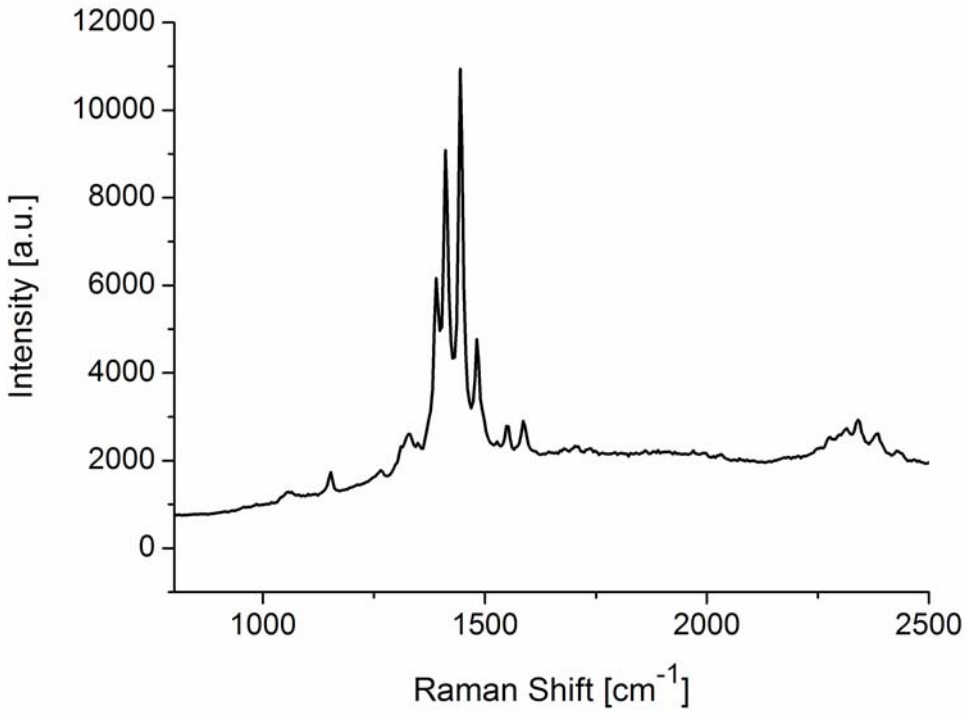

Figure 42: A typical SERS spectrum of a T4 molecule that was adsorbed on silver nanoparticles, using a 532-nm excitation laser.

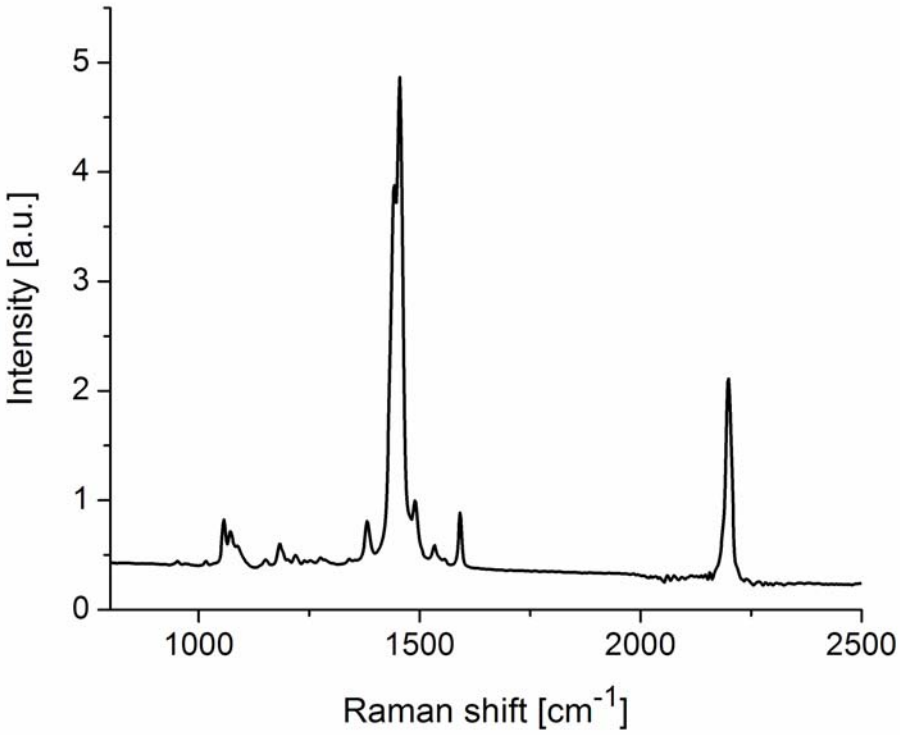

Figure 43: Raman spectrum of a T4 molecule in a powder form (free molecule).

A comparison between the Raman spectrum of T4 and the spectrum of similar molecules in the literature reveals similar features. To the best of my knowledge, the Raman spectrum of the same T4 molecule does not exist in the literature. Nevertheless, the Raman spectrum of a T4-like molecule, which also contains four thiophene rings in series but lacks the long alkane chains, has been measured and calculated [96, 98]. The common vibrations of our T4 and the T4-like molecules are the two strong bands originating from the collective motions of the C-C skeletal. In the T4-like molecule, they appear at 1461, 1506 cm^{-1}, whereas in our Raman measurements they appear at 1455 and 1489 cm^{-1}.

Unfortunately, the intensity of a SERS spectrum of a T4 molecule was not sufficiently high. Increasing the signal by using higher laser power caused a fast decay of the signal, which will be discussed later on. To overcome this problem, we used Rhodamine, which is known for its high SERS signal. Rhodamine is a dye molecule commonly used in SERS experiments because of its high quantum yield. The basic building blocks common to all Rhodamines are the dibenzopyrene chromophore (xanthene) and a derivative of a benzoic acid molecule (carboxyphenyl group) that is linked in para-position to the center ring of the xanthene. The

Rhodamines are singly charged, positive ions; there is no static electric dipole moment along the long axis of the molecule in either the ground or the excited state, and the positive charge is located symmetrically mainly on the two amino groups [99]. The π-electron system extends symmetrically between the two amino groups with mirror symmetry through the center ring, which leads to strong absorption and fluorescence in the visible spectral range. Rhodamines are especially suited to investigate the role of resonance enhancement in SERS, since a single unit consists basically of two linked chromophores that are sensitive to different spectral regions of electromagnetic radiation. One chromophore is the positively charged xanthene ion, which is strongly attracted to the metal surface by Coulomb interactions (via the amine groups) and has a strong absorption in the visible region. The other chromophore, which is conjugated to the xanthene, is the carboxyphenyl or benzoic acid group that absorbs in the near-UV region.

Although Rhodamine 6G is the most commonly used form of Rhodamine in SERS, it has tertiary amines that are known to attenuate binding to metals by adding steric bulk to the nitrogen center. Thus, we used Rh123 (Figure 44b), which has the advantage of having primary amines that are known to bind to metals via their lone pair of electrons [22].

Figure 44a shows a typical SERS spectrum of Rd 123 at a concentration of 1×10^{-8} M absorbed on silver colloids excited by a 532-nm laser. This spectrum was compared to the Raman spectrum of Rh123 in its powder form. It was found to be similar, as shown in Figure 44, except for the absence of the low-energy peaks in the SERS spectrum, which could not be measured due to the cutting of the signal at this wavelength regime.

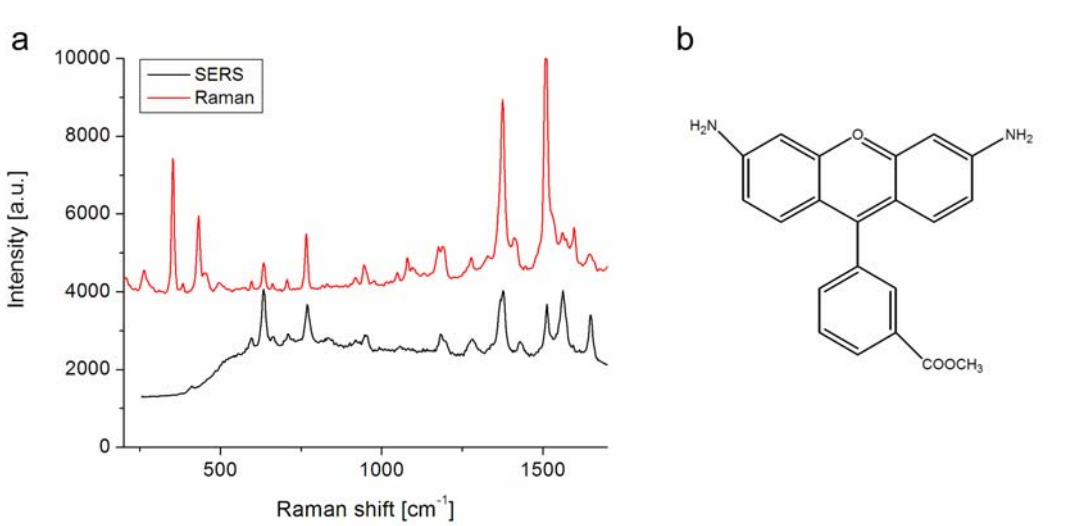

Figure 44: a) SERS spectrum of Rh123 adsorbed on silver nanoparticles (black line), Raman spectrum of Rh123 in a powder form (red line). b) Scheme of Rh123.

Rh123 was also measured by others [99, 100]; the reported spectrum (shown in Figure 45) is almost identical to ours (Figure 44). The assignment of the Rh123 peaks is shown in the table in Figure 45.

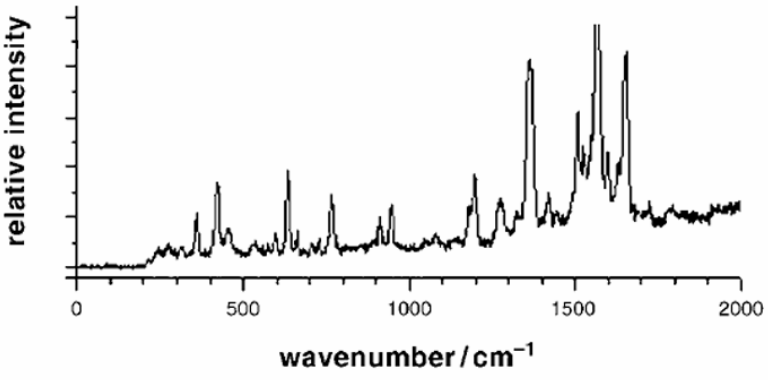

Assignment	R 123
	359 (w)
	419 (m)
C–C–C ip bend.	634 (m)
C–H oop bend.	768 (m)
	911 (w)
	949 (w)
C–H ip bend.	
	1200 (m)
ν C–O–C	1276 (m)
ν arom. C–C	1363 (vst)
ν arom. C–C	1507 (st)
ν arom. C–C	1569 (vst)
ν arom. C–C	1648 (vst)

Figure 45: SERS spectrum of Rh123 and a table showing its peak assignment, taken from Vosgrone *et al.* [99].

b) Tuning the laser excitation wavelength

In order to acquire high SERS signals, one should choose the appropriate experimental conditions that are specific for each molecule. As was discussed in the introduction, when the frequency of the excitation laser approaches the frequency of the electronic transition of the molecule, Raman scattering is enhanced. This

resonance Raman effect can be achieved when the excitation wavelength corresponds to the molecular absorption.

The absorption spectrum of the T4 molecule is shown in Figure 46. It is obvious that excitation wavelength at the peak range will result in a high SERS signal. Therefore, it was not surprising that a 532-nm excitation laser attained a low signal, owing to the lack of coupling to the molecular absorption. In order to obtain higher and more stable SERS signals, a 488-nm excitation laser was used. As Figure 46 shows, at this wavelength the laser overlaps the molecular absorption and it is separated by ~70 nm from the absorption peak. Indeed, at this excitation wavelength, the signal increased by a factor of 15. That was a great improvement; however, the signal was still low in comparison with other dye molecules. To further increase the signal, we tried to increase the laser intensity. As a result, the signal vanished after a short period of time, probably due to photobleaching, and it was not possible to perform long measurements.

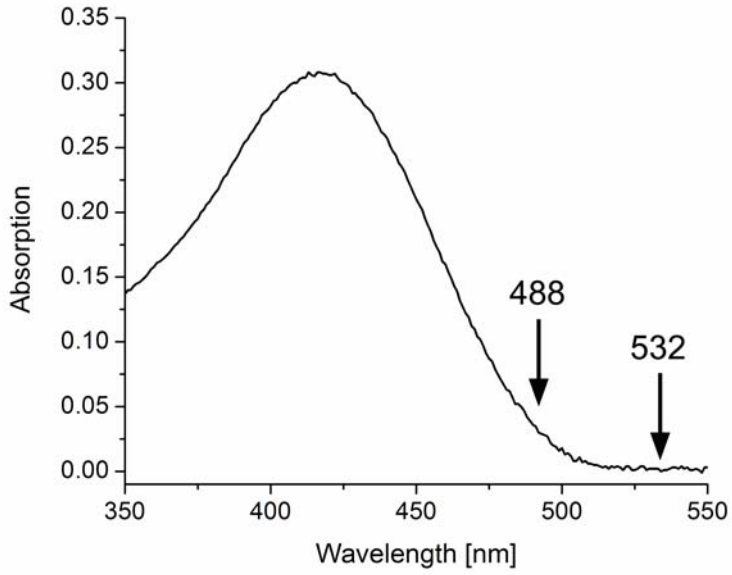

Figure 46: Absorption spectrum of a T4 molecule (1×10^{-5} M) dissolved in THF. The arrows indicate the position of excitation lasers.

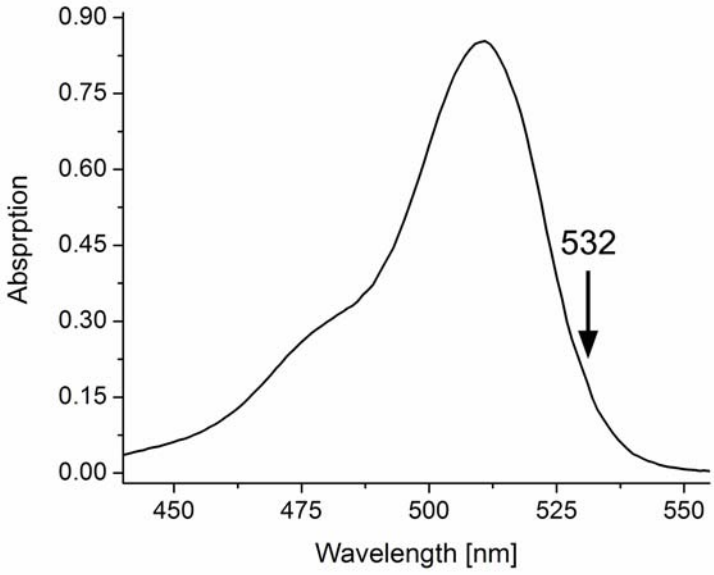

Figure 47: Absorption spectrum of Rh123 ($1x10^{-5}$ M) dissolved in ethanol. The arrow indicates the position of the excitation laser.

Because of the difficulties in using the T4 molecule, which were described above, we examined a different molecule, Rh123. The absorption spectrum of Rh123 is shown in Figure 47; its maximum absorption appears at 515 nm. The 532-nm laser is separated only by 17 nm from the maximum absorption. This separation is much smaller than that of the T4 molecule from the 488-nm laser line. And as a result, a higher and more stable signal was achieved. In conclusion, in comparing the two molecules, Rh123 has significant advantages: it is better coupled to the laser, and as a result, a lower laser intensity is needed and its life time is longer. For the above reasons, Rh123 was chosen for conducting most of the following experiments.

c) SERS with different metal nanoparticles

The SERS enhancement factor does not only depend on whether the excitation is in resonance with the electronic transition of the molecule (absorption) - it also depends on its coupling to the surface plasmon resonance of the nanoparticles. Thus, after choosing the excitation energy for each molecule, as described in the previous section, one should also consider the type of nanoparticles to be used. In the following section, I will examine the use of silver and gold nanoparticles.

As was shown in the introduction, the position of the surface plasmon of nanoparticles depends on the dielectric function of the material, and it is manifested in their excitation spectrum (see Equation 14). The maximum excitation of silver

nanoparticles is at 410 nm, whereas the maximum for gold is at 530 nm (Figures 13 and 39). For that reason, one would expect that excitation at 532 nm would result in better coupling to gold nanoparticles than to silver nanoparticles. But this is a bit more complicated, because the enhanced field is created in a junction between two close nanoparticles, and in that case, a coupling to the surface plasmon of a dimer should be taken into account. As mentioned in the introduction, the surface plasmon resonance of a single nanoparticle shifts to lower energy while coupled to another nanoparticle. Unfortunately, we could not measure the exact shift of the absorption of the dimer solution owing to its low concentration. Nevertheless, a shift of 80 nm was measured for dimers consisting of gold disks separated by 2 nm, as shown in Figure 10 [68]. The red shift is expected to get larger as the distance between the two disks becomes smaller. In our dimers the separation is approximately 1 nm (corresponding to the molecular length); hence, a larger shift is expected. As a result of the red shift, the surface plasmon resonance of silver nanoparticles gets closer to the excitation laser (532 nm), whereas that of the gold nanoparticles becomes farther away. The surface plasmon resonance of nanoparticles is also influenced by their size; this will be discussed in detail later on.

An additional factor that causes silver nanoparticles to achieve a better enhancement is its pronounced surface plasmon peak compared with gold, which results from the lack of damping in silver at the surface plasmon resonance regime.

Taking the above considerations into account, silver nanoparticles are better suited for our experiment. Indeed, SERS measurements of the T4 molecule revealed low signals with gold nanoparticles (that could not be recorded), compared with a significantly higher signal with silver nanoparticles. Thus, all the results that are presented here were collected using silver nanoparticles with a 532-nm excitation laser.

3.2.2 Correlating between the SERS hot spots and dimers

In this part of this work the SERS signal of the measured molecules was correlated with the presence of dimers. In principle, the measured SERS spectra could originate from molecules assembled in the dimer structures, but also from molecules that were adsorbed on the sample surface, or on single nanoparticles. In order to examine the source of the SERS signal, we conducted a SERS experiment by adsorbing dimers (of

T4 or Rh123 molecules) on top of a predefined substrate (Figure 48) and correlated the location of the SERS signal with the SEM images.

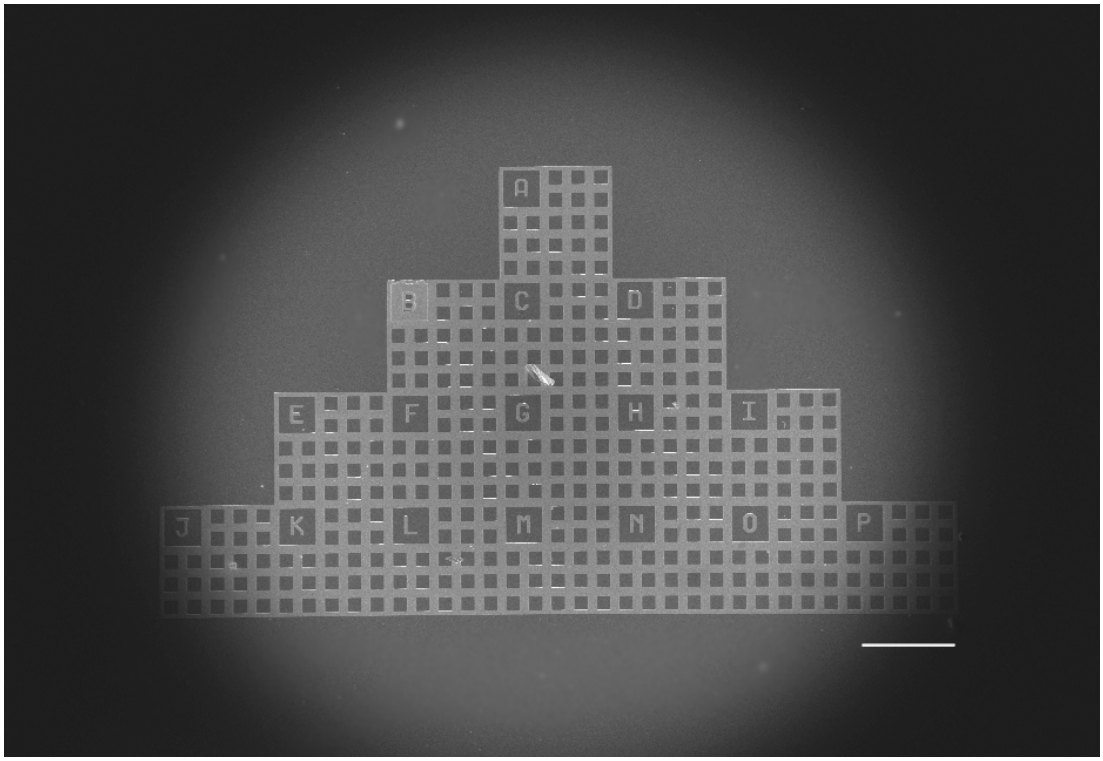

Figure 48: SEM image of a glass substrate marked with a grid pattern that was prepared using optical lithography. The dimensions of the squares are 10 x 10 μm.

A solution that contains about 30% T4 dimers was adsorbed on a predefined glass substrate with a patterned grid, as shown in Figure 48. Each square was illuminated with a laser beam of 15-μm diameter, so all potential molecules in the square could yield a Raman signal simultaneously. The measurement procedure was as follows: we first recorded the image of the illuminated square that contains the SERS hot spots using the CCD. We then quickly introduced a grating and collected the SERS spectrum from the hot spots. Later on, the sample was examined in the SEM; the grid pattern enabled us to navigate through the sample, and to take a high-resolution SEM image of the structure at the same position of the SERS spot that was measured. An example of an image of a square that depicts a single Raman hot spot (which appears as a bright spot) is shown in Figure 49. The SEM image revealed that the source of this SERS signal was a dimeric nanoparticle structure (higher magnification in the inset). All other objects in this square were single nanoparticles. More than 60 high-intensity spots were examined for T4 and Rh123, and 94% were due to dimeric structures. The remaining spots were due to higher order conjugates. Single nanoparticles did not give rise to a SERS hot spot. This result is in agreement with the

experiments done by Xu and coworkers [69, 75]. They showed that aggregation of nanoparticles is a necessary condition for obtaining a Raman spectrum from single hemoglobin molecules and identified the SERS hot sites to be mostly dimers and trimers. However, the formation of dimers in their case is not controlled by specific chemicals binding to the nanoparticles.

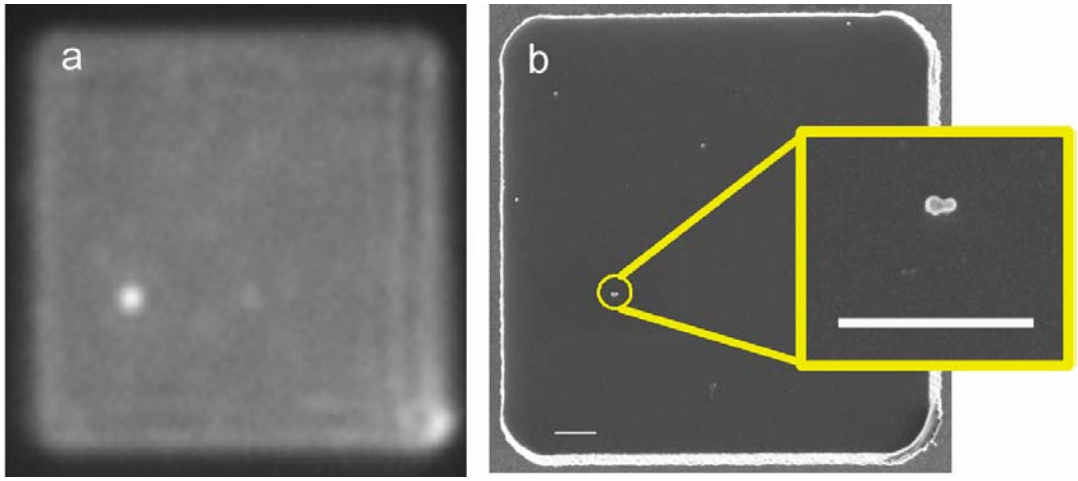

Figure 49: a) An image of one of the squares of the predefined sample that contained a single SERS signal (the bright spot). b) SEM image of the same square. In the same location of the SERS signal spot a clear dimer was observed (inset), all other objects in this square were single nanoparticles. The scale bar is 1 μm.

3.2.3 Temporal fluctuations in SERS

The common signature of single-molecule spectroscopy is spectral fluctuations. These fluctuations are characterized by a reversible decrease or the disappearance of the emission, taking place in a time scale of microseconds to seconds, which is referred to as blinking. Blinking is most often light induced and can result from processes such as transient populations of non- or low-emissive states, such as excited triplet states [101], photo-isomerization [102], or conformational changes that modify the absorption and/or emission properties of the molecule [103]. Time-dependent SERS spectra of nanoparticle dimers bridged by single molecules of T4 and Rh123 are shown in Figure 50. The blinking seen in the time-dependent spectra implies that a single molecule was bridging the nanoparticle structure.

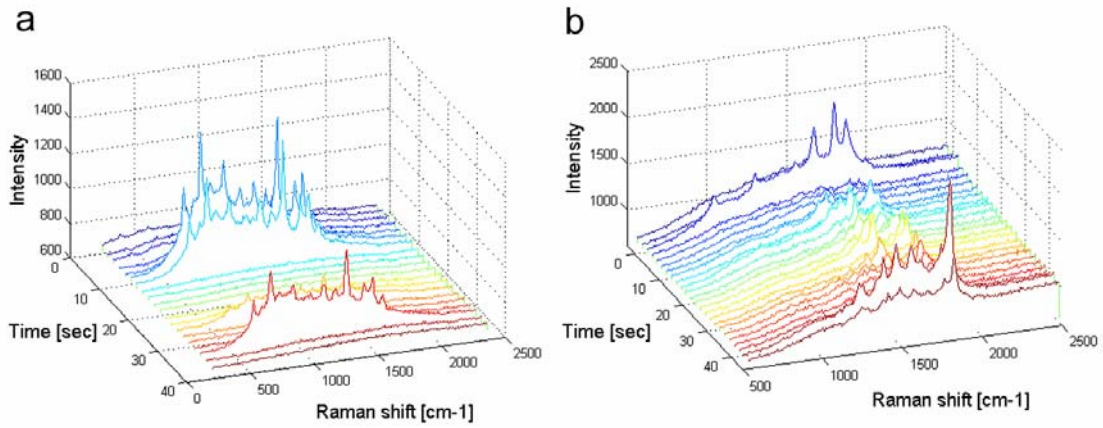

Figure 50: Blinking of the SERS spectra of a) a Rh123 molecule and b) a T4 molecule. The molecules were mixed with an excess of 10-fold silver nanoparticles over molecules.

3.2.4 Core-shell gold-silver nanoparticles

The experimental results so far revealed that most of the SERS signal originates from dimer structures and that these structures are very likely to contain a single molecule. To further study the effect of nanoparticle surface plasmons on the SERS signal, silver nanoparticles with well-defined dimensions are required as building blocks for the dimers. For that purpose, we used the core-shell nanoparticles of gold-silver. The absorption spectra of the core-shell nanoparticles (Figures 39 and 40) reveal that the optical properties of the gold-core/silver-shell nanoparticles are dominated by the silver shell [94], and thus could potentially lead to a high signal in the SERS experiment. Indeed, we found that these nanoparticles yield high SERS enhancement. For that reason, these nanoparticles were used in the following experiments.

3.2.5 Effect of laser polarization

Using the uniform core-shell nanoparticles, we were able to perform a systematic study of the effect of nanoparticle size on enhanced electro-magnetic field. In this experiment, Rh123 dimers with various nanoparticle diameters were measured. A representative histogram of the distribution of the intensity measurements of dimers consisting of a 33.5 nm diameter is plotted in Figure 51a. It can be seen that a large variety of intensities exists for the same size of nanoparticles. In order to estimate the SERS intensity for each size of nanoparticles, one needs to understand the reason for that distribution.

In our experimental setup, the dimers are randomly oriented on the surface. For a given incident EM field (E_0), each dimer exhibits a different field (E). This field depends on the angle (θ) between the incident field and the main axis of the dimer (Figure 51b inset) according to the following relation

$$E = E_0 \cos\theta \quad (17)$$

The SERS intensity (I) depends on the angle θ as

$$I = I_{\max} \cos^2 \theta \quad (18)$$

Taking into account an equal probability for all angles (θ), the intensity distribution is defined by

$$\frac{d\theta}{dI} \propto \frac{1}{\sqrt{I / I_{\max} - \left(I / I_{\max}\right)^2}} \quad (19)$$

This analysis leads to an intensity distribution that has a high probability for low and high intensities and a low probability for the middle intensities, as plotted in Figure 51b. A comparison of the two histograms, presented in Figure 51, reveals agreement in the distribution shape at the low intensity regime. Note, however, that the theory deviates from the experimental histogram at the high intensity regime. This is presumably due to the difference in the local field strength between dimers that are oriented parallel and perpendicular to the direction of the laser polarization. In the parallel orientation, the local field is much stronger, as was shown in the introduction (Figure 11), which leads to a short life time of the molecule. As a result, the higher intensity signals were measured relatively infrequently due to the finite time required to make the measurement (on the order of a minute) versus the time of decay of the signal (on the order of seconds).

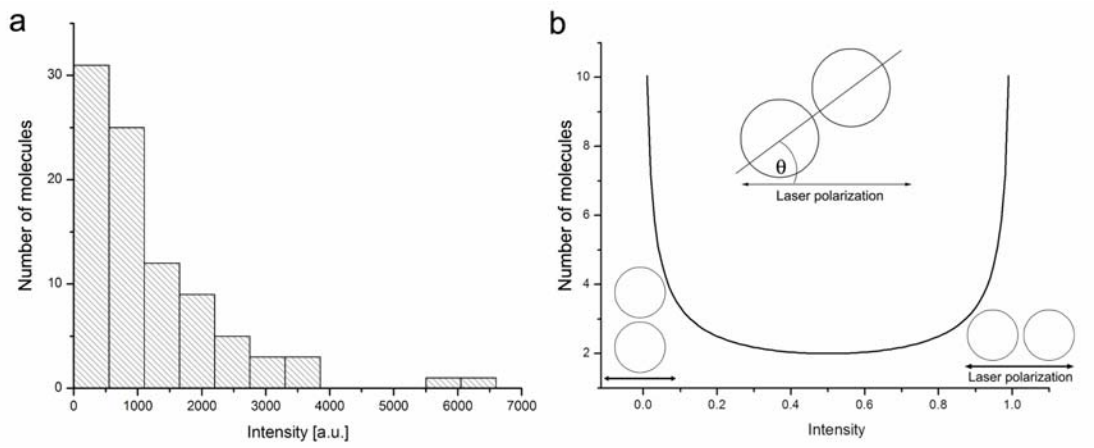

Figure 51: a) A histogram of the SERS intensity measured for 33.5-nm diameter nanoparticles. b) SERS intensity distribution, as derived from the model (Equation 19) of different angles between the dimer and the laser polarizability. The intensity is related to the angle θ (Equation 18); it is high for the parallel configuration and low for the vertical configuration.

3.2.6 Intensity of SERS signal as a function of nanoparticle sizes

Understanding the variation of the signal intensity enabled us to calculate the characteristic SERS intensity for each nanoparticle size. Because it was not possible to collect the high intensity Raman signals (for the reason described above), the SERS intensities were extracted from the low Raman intensity data. Figure 52 shows the measured SERS intensities of dimers as a function of the nanoparticle's radius for three sets of nanoparticles (each has a different core size). The intensity values were extracted from the histograms by calculating the *Imax* of its first columns using Equation 19; each point in the graph represents a datum that was collected from 20 to 70 hot spots. The three sets of nanoparticles show the same trend: as the nanoparticle grows, the SERS signal increases.

This behavior can be explained by calculating the *near-field* at the junction of a dimer for different sizes of nanoparticles; this will be discussed in detail in the next section.

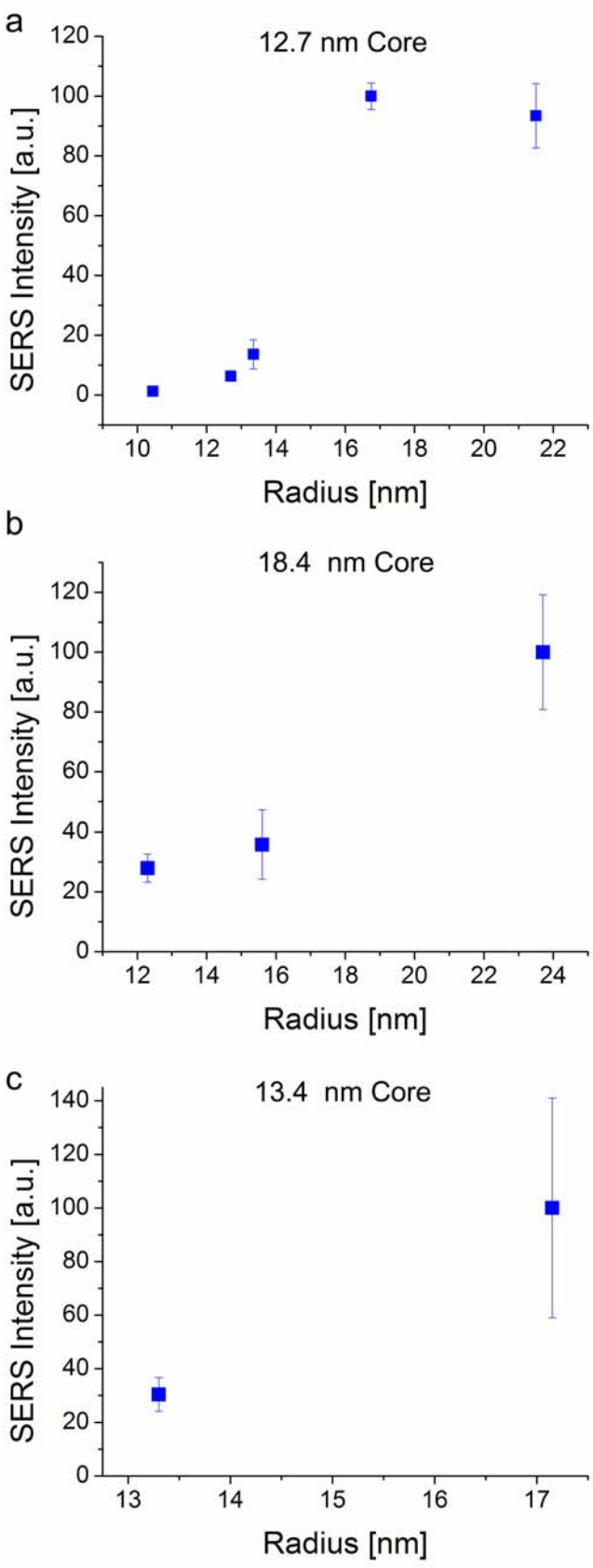

Figure 52: Measured SERS intensity as a function of the total radius of the nanoparticle for different sizes of gold cores a) 12.7-nm core diameter, b) 18.4-nm core diameter, and c) 13.4-nm core diameter.

3.2.7 Calculations of the near-field in the junction of a dimer

The SERS hot spot is generated by the interaction between electromagnetic radiation and localized surface plasmon resonances. In a dimer the highest field, namely, the hot spot, is at its junction, as was shown in Figure 11. In order to interpret the experimental results above, we calculated the *near-field* at the junction of a dimer for various conditions.

The calculations were performed by Garnett Bryant from NIST using the boundary element method in a full electromagnetic calculation including retardation [104]. The *near-field* is at the junction between two nanoparticles generated as a response to the applied electromagnetic field; it is shown in Figure 53.

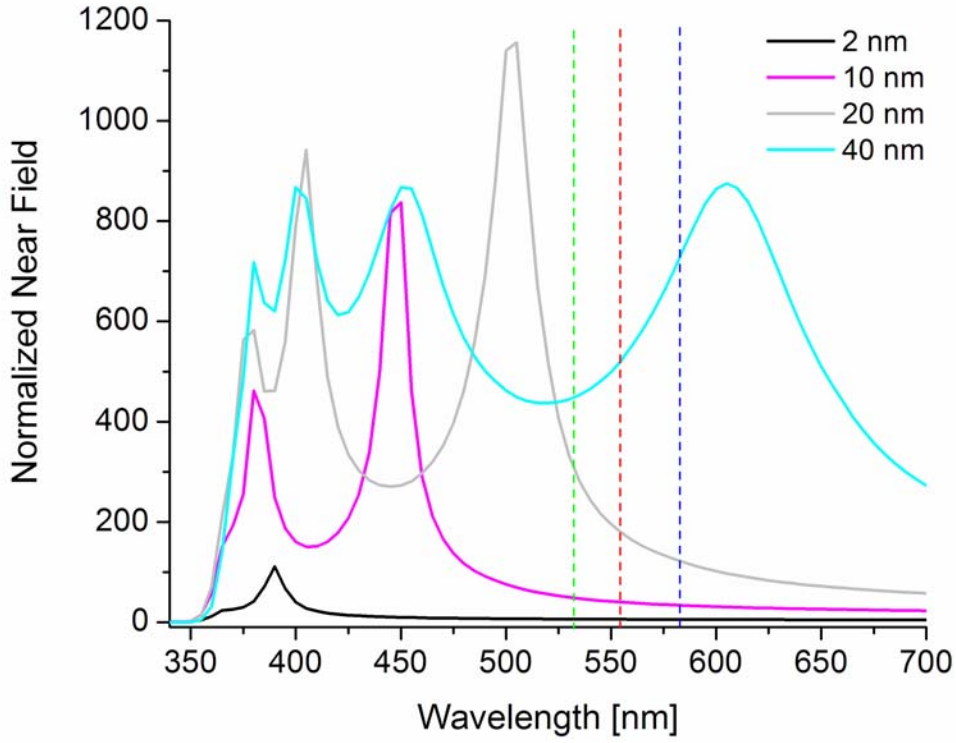

Figure 53: Calculation of the *near-field* at the junction of a dimer (with a gap of 1 nm) as a function of the nanoparticles' radius. In these calculations the effective dielectric constant is 1.5 (of the substrate). As the nanoparticle gets bigger, its spectrum spreads through a wider range of wavelengths. The green, red, and blue dashed vertical lines represent the excitation (532 nm) and emission wavelengths of Rh123 (554 and 582 nm, which correspond to the Raman lines of 634 and 1648 cm^{-1}, respectively), respectively.

The calculation was done for an excitation by an incident plane wave polarized parallel to the long axis of a dimer with a gap of 1 nm (corresponding to the molecular length of Rh123). Dimers consisting of small nanoparticles (radius 2 nm) exhibit a

single *near-field* peak (resonance), as expected from small particles that are in the *quasi static* regime that is satisfied by the dipolar surface plasmon resonance condition. When the nanoparticles get larger, retardation and multipole surface plasmon resonances are also dominant, as was shown in Figure 8. Indeed, it can be seen in Figure 53 that the *near-field* spectrum of large nanoparticles turns out to be more complicated, as more peaks appear in the spectrum.

SERS enhancement is the product of the enhanced fields at the excitation wavelength and at the emission wavelength, following Equation 14. As was discussed in the introduction, the better the excitation and the emission that are coupled to the surface plasmon resonance of the nanoparticles, the larger the SERS enhancement.

In order to understand the results of Figure 52, we will focus on the reddest surface plasmon peak of the dimer and its coupling to the excitation and emission (dashed vertical lines in Figure 53). For the small nanoparticles (2- and 10-nm radius), the surface plasmon spectrum does not overlap the excitation and emission; thus, low enhancement is expected. As the nanoparticle's size increases from 20 nm to 40 nm, the red peak of its surface plasmon spectrum shifts to a longer wavelength and crosses both excitation and emission. When the surface plasmon peak is positioned between the excitation and emission, the highest enhancement is expected. After the crossover, the enhancement is expected to be reduced, leading to a peak-shaped enhancement spectrum.

Figure 54 shows the calculated size dependence of the enhancement of the two extreme Raman lines of Rh123 (634 and 1648 cm^{-1}) when excited by 532 nm (denoted by dashed lines), following Equation 11: $\rho \sim E^2(\lambda_{excitation}) \cdot E^2(\lambda_{emission})$.
It can be seen that in the NP-size range studied in our experiment (10-24 nm radii), both Raman lines get stronger as the NP size increases. This explains, at least qualitatively, the observed behavior in Figure 52. One should note, however, that this dependence does not persist for larger particle sizes. Rather, a maximum is reached at a certain NP size, which depends on the wavelength of the Raman line; the longer the wavelength of the Raman line, the maximum appears at a larger NP size.

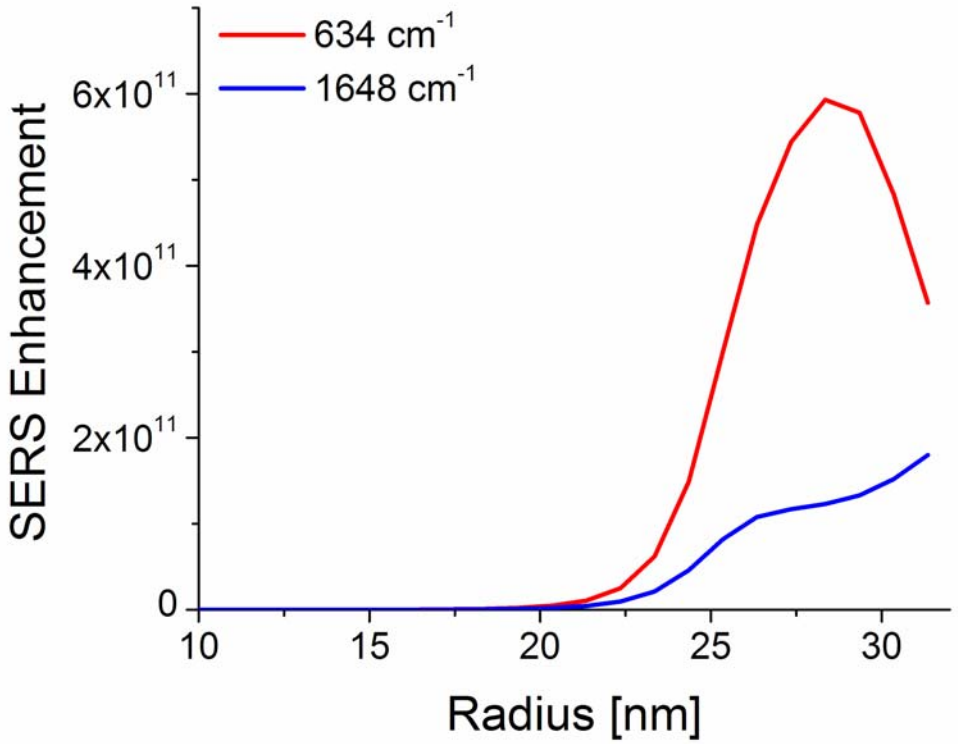

Figure 54: Calculation of the SERS enhancement as a function of a nanoparticle's radius, at a junction of a dimer consisting of two core-shell nanoparticles (Au core of 6.35-nm radius and varied Ag shell) with a separation of 1 nm. The calculation followed the equation $E^2(\lambda_{excitation})\cdot E^2(\lambda_{emission})$, for $\lambda_{excitation}$=532 nm and for $\lambda_{emission}$=554 and 582 nm (it corresponds to 634 and 1648 cm^{-1}, respectively) with an effective dielectric constant of 1.5.

An interesting aspect of the coupling between the surface plasmons and Raman scattering was found when calculating the enhancement of different vibrational modes of Rh123 as a function of nanoparticle size (Figure 54). We chose to compare the enhancement of two vibration modes that are at the extreme of the Raman spectrum of Rh123: 634 and 1648 cm^{-1}. Whereas the enhancement of the 634 cm^{-1} emission mode exhibits a maximum at this size regime, the enhancement of the 1648 cm^{-1} mode monotonically increases. Thus, the vibrational modes of Rh123 of a lower wavelength could be more pronounced when it is adsorbed on nanoparticles of a larger size, giving rise to a tilt of the spectrum.

Examination of the experimental SERS spectrum of Rh123 for different nanoparticle radii (14 and 22 nm) is shown in Figure 55. The two discussed modes are denoted by arrows. The relative intensity of the two emission modes is significantly different for the two nanoparticle sizes. In the case of small nanoparticles, the intensity of the two modes is similar, whereas the 634 cm^{-1} mode is much more

enhanced in the case of large nanoparticles. This result is in good agreement with the above calculations shown in Figure 54, and it was observed for 16 different molecules.

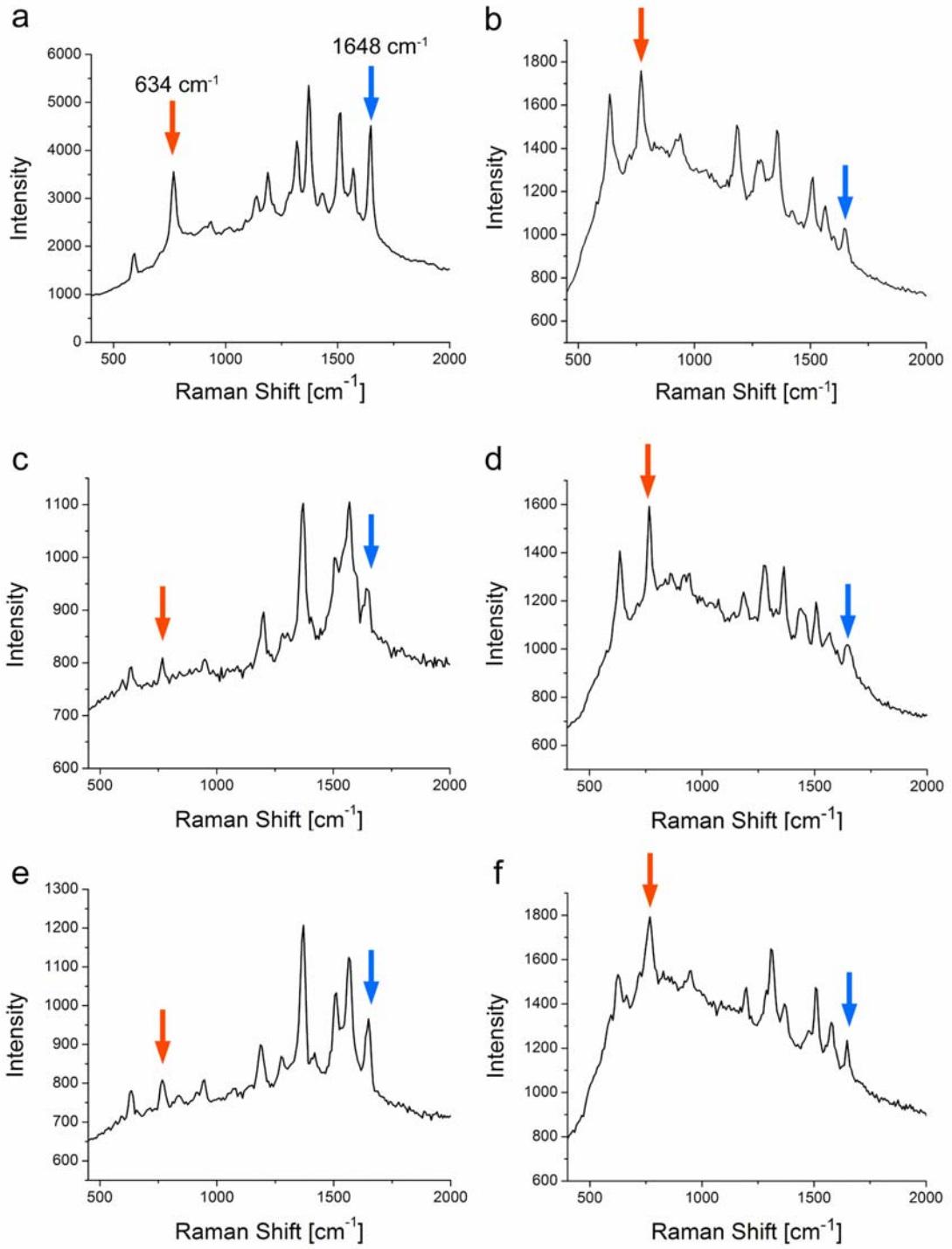

Figure 55: SERS spectra of various Rh123 dimers that consist of two nanoparticle sizes: 14 nm radius (a, c and e) and 22 nm radius (b, d, and f). The red and blue arrows identify the 634 and 1648 cm^{-1} Raman modes, respectively.

The finding implies that the fact that the SERS signal increases with particle size is not general - it manifests the red shift of the plasmon resonance towards the

wavelength of the laser and Raman lines with increasing particle size. In fact, when the excitation laser wavelength is chosen to be shorter than the dipole plasmon resonance, one would observe an opposite effect, of decreased SERS intensity with increasing particle size.

4. Summary and Outlook

This thesis focused on the electronic and spectroscopic characterization of single molecules. In the first part, the dimer method for contacting a single molecule was introduced. The dimer structure consists of two gold nanoparticles connected by a single dithiolated organic molecule; it is synthesized by mixing molecules that have two clips with a solution of nanoparticles. The presence of a single molecule in the dimer structure is ensured by using a much lower molecular concentration in the reaction mixture with respect to the concentration of the nanoparticles (a tenfold excess of nanoparticles). It was also verified by counting the percentage of dimers in the solution as a function of the amount of molecules in the reaction.

The electrostatic trapping method was used to position the dimers between two electrodes with a small gap. It was found that the parameters that affect the yield of this process are the trapping time, the applied AC voltage, and its frequency; when the frequency is increased, the nanoparticles are attracted more and are better aligned between the electrodes. The contacts of our system without the molecule were characterized by measuring the conductance of a single nanoparticle. In these measurements, single-electron transistor behavior was observed with a typical charging energy that scales with the nanoparticle's size, as expected. Gating measurements were also performed, yielding the typical diamond structure of a SET.

The electrical conduction of three short organic molecules was studied; a fully conjugated molecule, 4,4'-biphenyldithiol (BPD), Bis-(4-mercaptophenyl)-ether (BPE) in which the conjugation is broken at the center by an oxygen atom, and 1,4-benzenedimethanethiol (BDMT), where the conjugation is broken near the contacts by a methylene group. It was found that the electrical conduction through BPE and BDMT is significantly lower than through the BPD molecule. The apparent gap and exponential turn-on of the differential conductance in the case of the BPE and BDMT suggest that adding localizing groups interferes with the conjugated aromatic system and suppresses the overall conductance through the molecule. This assertion was demonstrated when comparing the BPE with the BPD molecule, where the addition of an oxygen atom between the conjugated rings suppresses the conductance almost entirely below 1V. A similar effect takes place in the BDMT dimers, where the methylene groups suppress the overlap of the molecular backbone orbitals with the contacts.

The conduction through BPD showed not only high conductivity but also a peak structure. This conductance spectrum was highly reproducible; however, temporal fluctuations of the peak position were observed. These temporal fluctuations are considered as evidence for gating of the molecule, which occurs randomly and depends on the voltage sweep rate and the voltage range of the measurement. However, it could be substantially minimized by working at low sweep rates and within a limited voltage range, such that stable and reproducible measurements can be conducted over hours.

The reproducibility of the conduction measurements of the BPD molecule was confirmed by plotting a histogram of all measured BPD spectra, resolving a typical peak structure that agrees well with other experimental measurements.

To summarize, the dimer method provides a generic tool box for studying electron conductance through single molecules; it has the following advantages:

- It allows studying any type of molecule with two clips such as thiols and amines.
- Different metal nanoparticles or even semi-conducting nanoparticles can be used for the formation of the dimers. Thus, the effect of the metal on the molecular conductivity can be studied.
- The distance between the two electrodes can be easily varied, allowing the use of different sizes of nanoparticles.
- The devices can be imaged in a SEM to verify the existence of a dimer.
- Gating of the molecular junction is achievable in this system in a relatively straightforward way.
- Temperature-controlled measurements can also be performed.

Since our work was published, a few theoretical studies have described the conduction characteristics by which our measurements were done [89, 105]. The effect of the torsion angle, between the two benzene rings in the BPD molecule, on the molecular conductance has also been demonstrated, showing that the non-coplanarity configuration of the two phenyl rings reduces the electron transport through the molecule [106]. Recently, Jeong-Seok Na *et al*. were able to perform conductance measurements of OPE molecules by using our dimer method [107].

In the second part of the work, the dimers were used to perform single-molecule SERS measurements. When an electromagnetic field interacts with nanoparticles, SERS is created, manifested by hot spots at the junctions between nanoparticles. In order to study the fundamental phenomenon of SERS systematically, nearby objects should be produced (from a distance of a few nanometers and shorter). As the resolution of nanolithography reaches the limit of a few nanometers, dimer structures provide intra-particle distance that is controlled by the molecule length, which can be decreased to a sub-nanometer scale.

In this study, the SERS of the measured molecules was correlated with the presence of dimers. It was shown that 94% of the signals originated from dimers; the remaining spots were due to higher-order conjugates. Single nanoparticles did not give rise to SERS hot spots. Furthermore, temporal fluctuations of the molecular spectrum, which represent the signature of single molecules, were observed. Later on, the dimers were used to study the enhancement mechanism of SERS. For this study, we synthesized uniform core-shell nanoparticles of gold-silver. These nanoparticles exhibit optical properties similar to silver nanoparticles, resulting in high SERS enhancement. It was shown that the enhancement is significantly dependent on the nanoparticles' size; as the size increased, the signal was significantly enhanced. This was attributed to the better coupling of the surface plasmon resonance of the dimer to the excitation and emission, in the case of large nanoparticles. The near-field at the junction of a dimer was calculated as a function of the nanoparticle's size to further understand the underlying mechanism. The experimental results were found to be in good agreement with these calculations.

Another way of predicting these calculations was that vibrational modes that are better coupled to the surface plasmon of the dimers will be more pronounced. In our case, the low-energy Raman peaks were better enhanced when the dimers consisted of large nanoparticles (22 nm radius), giving rise to a tilt of the spectrum.

In order to find the optimal conditions for a specific experimental system, one needs to consider the right combination of excitation energy, molecule, nanoparticle material, and size. This work shed light over the experimental factors that affect the SERS enhancement mechanism, and provided some theoretical knowledge of this mechanism.

The dimer toolbox can provide a platform for simultaneously performing both SERS and transport measurements of single molecules. Such an experiment can

provide us with important information regarding the coupling between electron transfer through a molecule and its vibration modes and also about the influence of the external electric field on the molecular vibrations levels.

Appendix A

Synthesis of the BPD and BPE molecules

The synthesis of the two molecules was carried out by Veronica Frydman from the Chemical Services unit at the Weizmann Institute, following the procedure of Baron [108].

Synthesis of biphenyldithiol (BPD)

Stannous chloride dihydrate (75 g, 0.33 mol) and biphenyl-4,4'-disulfonyl chloride (11.7 g, 0.033 mol) were suspended in ethanol (120 mL) and cc HCl (120 mL). The mixture was heated at reflux with vigorous stirring for 18 h, cooled to room temperature and the solid was collected by filtration. The crude solid was dissolved in 5% aq. NaOH (200 mL) and reprecipitated by filtering into cold cc HCl (50 mL). The solid was collected by filtration and this purification procedure was repeated 3 more times. The yellow solid was finally dried under vacuum (5 g, 69%).

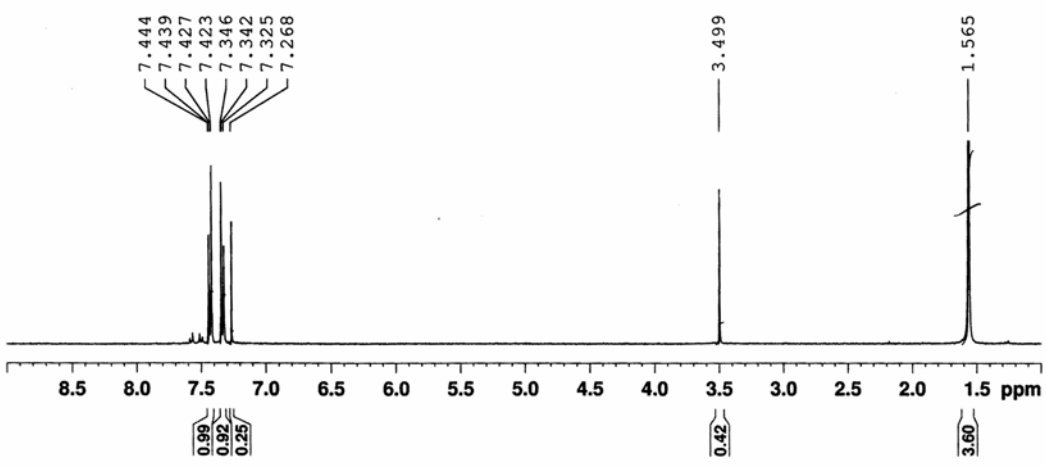

Figure S1: NMR spectrum of BPD dissolved in Cl_3CD.

Synthesis of 4,4'-dimercaptodiphenyl ether (BPE)

Stannous chloride dihydrate (30.69 g, 0.136 mol) and 4,4'-bis(chlorosulfonyl)diphenyl ether (5 g, 0.0136 mol) were suspended in ethanol (50 mL) and cc HCl (50 mL). The mixture was heated at reflux for 6 h, cooled to room temperature and poured into cold cc HCl (123 mL). The solid was collected by filtration, dissolved in 5% NaOH (82 mL) and reprecipitated by filtration into cold cc HCl (21 mL). This purification procedure was repeated 3 more times. The yellow solid was dried under vacuum (1.2 g, 40%) and stored at -4°C.

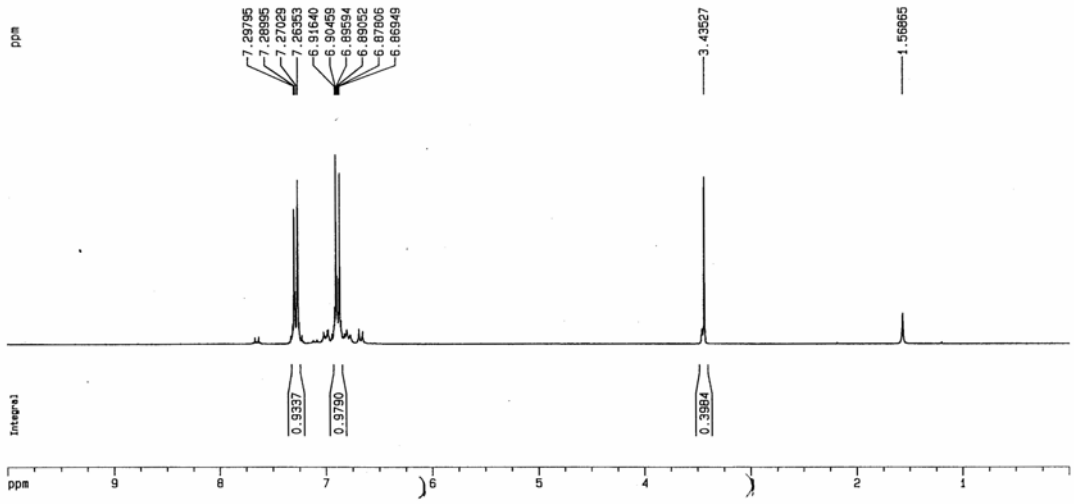

Figure S2: NMR spectrum of BPE dissolved in Cl_3CD.

References

1. Jeanmaire, D.L. and R.P. Van Duyne, *Surface Raman spectroelectrochemistry. Part I. Heterocyclic, aromatic, and aliphatic amines adsorbed on the anodized silver electrode.* Journal of Electroanalytical Chemistry and Interfacial Electrochemistry, 1977. **84**(1): p. 1-20.
2. Albrecht, M.G. and J.A. Creighton, *Intense Raman spectra at a roughened silver electrode.* Electrochimica Acta, 1978. **23**(10): p. 1103-5.
3. Aviram, A. and M.A. Ratner, *Molecular rectifiers.* Chemical Physics Letters, 1974. **29**(2): p. 277-283.
4. Nitzan, A., *Electron transmission through molecules and molecular interfaces.* Annual Review of Physical Chemistry, 2001. **52**: p. 681-750.
5. Basch, H., R. Cohen, and M.A. Ratner, *Interface Geometry and Molecular Junction Conductance: Geometric Fluctuation and Stochastic Switching.* Nano Lett., 2005. **5**(9): p. 1668-1675.
6. Rampi, M.A. and G.M. Whitesides, *A versatile experimental approach for understanding electron transport through organic materials.* Chemical Physics, 2002. **281**(2-3): p. 373-391.
7. Holmlin, R.E., et al., *Electron Transport through Thin Organic Films in Metal-Insulator-Metal Junctions Based on Self-Assembled Monolayers.* Journal of the American Chemical Society, 2001. **123**(21): p. 5075-5085.
8. Xu, B. and J. Tao Nongjian, *Measurement of single-molecule resistance by repeated formation of molecular junctions.* Science, 2003. **301**(5637): p. 1221-3.
9. Tour, J.M., *Conjugated macromolecules of precise length and constitution. Organic synthesis for the construction of nanoarchitectures.* Chemical Reviews, 1996. **96**(1): p. 537-553.
10. He, J., et al., *Electronic Decay Constant of Carotenoid Polyenes from Single-Molecule Measurements.* J. Am. Chem. Soc., 2005. **127**(5): p. 1384-1385.
11. Onuchic, J.N., et al., *Pathway Analysis of Protein Electron-Transfer Reactions.* Annual Review of Biophysics and Biomolecular Structure, 1992. **21**: p. 349-377.
12. Mantooth, B.A. and P.S. Weiss, *Fabrication, assembly, and characterization of molecular electronic components.* Proceedings of the Ieee, 2003. **91**(11): p. 1785-1802.
13. Salomon, A., et al., *Comparison of electronic transport measurements on organic molecules.* Advanced Materials, 2004. **16**(6): p. 1881-1890.
14. Wold, D.J., et al., *Distance dependence of electron tunneling through self-assembled monolayers measured by conducting probe atomic force microscopy: unsaturated versus saturated molecular junctions.* Journal of Physical Chemistry B, 2002. **106**(11): p. 2813-2816.
15. Kushmerick, J.G., et al., *Effect of Bond-Length Alternation in Molecular Wires.* J. Am. Chem. Soc., 2002. **124**(36): p. 10654-10655.
16. Kushmerick, J.G., et al., *Metal-Molecule Contacts and Charge Transport across Monomolecular Layers: Measurement and Theory.* Physical Review Letters, 2002. **89**(8): p. 086802.

17. Sellers, H., et al., *Structure and binding of alkanethiolates on gold and silver surfaces: implications for self-assembled monolayers.* J. Am. Chem. Soc, 1993. **115**(21): p. 9389-401.
18. Kornilovitch, P.E. and A.M. Bratkovsky, *Orientational dependence of current through molecular films.* Physical Review B, 2001. **64**(19): p. 195413/1-195413/4.
19. Mayor, M., et al., *Electric current through a molecular rod - relevance of the position of the anchor groups.* Angewandte Chemie, International Edition, 2003. **42**(47): p. 5834-5838.
20. Whetten, R.L. and R.C. Price, *Nano-Golden order.* Science, 2007. **318**(5849): p. 407-408.
21. Jadzinsky, P.D., et al., *Structure of a Thiol Monolayer-Protected Gold Nanoparticle at 1.1 .ANG. Resolution.* Science, 2007. **318**(5849): p. 430-433.
22. Venkataraman, L., et al., *Single-Molecule Circuits with Well-Defined Molecular Conductance.* Nano Letters, 2006. **6**(3): p. 458-462.
23. Venkataraman, L., et al., *Dependence of single-molecule junction conductance on molecular conformation.* Nature, 2006. **442**(7105): p. 904-907.
24. Seminario, J.M., C.E. De La Cruz, and P.A. Derosa, *A Theoretical Analysis of Metal-Molecule Contacts.* J. Am. Chem. Soc., 2001. **123**(23): p. 5616-5617.
25. Grabert, H. and M.H. Devoret, *Single Charge Tunneling*. 1992: Plenum New York.
26. Datta, S., *Electronic Transport in Mesoscopic Systems*. 1995: Cambridge University Press.
27. Cuniberti, G., et al., *Introducing Molecular Electronics. (Proceedings from the International Workshop on Advances in Molecular Electronics: From Molecular Materials to Single-Molecule Devices held in February 2004 in Dresden, Germany.) [In: Lect. Notes Phys., 2005; 680]*. 2005. 518 pp.
28. Nitzan, A. and M.A. Ratner, *Electron Transport in Molecular Wire Junctions.* Science, 2003. **300**(5624): p. 1384-1389.
29. Xue, Y. and M.A. Ratner, *Microscopic study of electrical transport through individual molecules with metallic contacts. I. Band lineup, voltage drop, and high-field transport.* Physical Review B, 2003. **68**(11): p. 115406-18.
30. Xue, Y.Q. and M.A. Ratner, *End group effect on electrical transport through individual molecules: A microscopic study.* Physical Review B, 2004. **69**(8): p. 085403.
31. Lindsay, S.M. and M.A. Ratner, *Molecular transport junctions: Clearing mists.* Advanced Materials, 2007. **19**(1): p. 23-31.
32. Selzer, Y. and D.L. Allara, *Single-molecule electrical junctions.* Annual Review of Physical Chemistry, 2006. **57**: p. 593-623.
33. Bezryadin, A., C. Dekker, and G. Schmid, *Electrostatic trapping of single conducting nanoparticles between nanoelectrodes.* Applied Physics Letters, 1997. **71**(9): p. 1273-1275.
34. Klein, D.L., et al., *An approach to electrical studies of single nanocrystals.* Applied Physics Letters, 1996. **68**(18): p. 2574-2576.
35. Kubatkin, S., et al., *Single-electron transistor of a single organic molecule with access to several redox states.* Nature, 2003. **425**(6959): p. 698-701.

36. Park, H., et al., *Fabrication of metallic electrodes with nanometer separation by electromigration.* Applied Physics Letters, 1999. **75**(2): p. 301-303.
37. Reed, M.A., et al., *Conductance of a Molecular Junction.* Science, 1997. **278**(5336): p. 252-254.
38. Smit, R.H.M., et al., *Measurement of the conductance of a hydrogen molecule.* Nature, 2002. **419**(6910): p. 906-909.
39. Reichert, J., et al., *Low-Temperature Conductance Measurements On Single Molecules.* Applied Physics Letters, 2003. **82**(23): p. 4137-4139.
40. Joachim, C., et al., *Electronic Transparency of a Single C-60 Molecule.* Physical Review Letters, 1995. **74**(11): p. 2102-2105.
41. Porath, D., et al., *Tunneling spectroscopy of isolated C60 molecules in the presence of charging effects.* Physical Review B, 1997. **56**(15): p. 9829-9833.
42. Cui, X.D., et al., *Reproducible Measurement of Single-Molecule Conductivity.* Science, 2001. **294**(5542): p. 571-574.
43. Dorogi, M., et al., *Room-Temperature Coulomb-Blockade From a Self-Assembled Molecular Nanostructure.* Physical Review B, 1995. **52**(12): p. 9071-9077.
44. Xu, B., X. Xiao, and N.J. Tao, *Measurements of single-molecule electromechanical properties.* Journal of the American Chemical Society, 2003. **125**(52): p. 16164-16165.
45. Djukic, D., et al., *Stretching dependence of the vibration modes of a single-molecule Pt-H2-Pt bridge.* Physical Review B: Condensed Matter and Materials Physics, 2005. **71**(16): p. 161402/1-161402/4.
46. Li, X.L., et al., *Measurement of electron transport properties of molecular junctions fabricated by electrochemical and mechanical methods.* Surface Science, 2004. **573**(1): p. 1-10.
47. Szymanski, H.A., *Raman Spectroscopy, Theory and Practice*. 1967: Plenum Press New York.
48. Smith, E. and G. Dent, *Modern Raman Spectroscopy, A Practical Approach*. 2005: John Wiley & Sons, Ltd.
49. Fleischmann, M., P.J. Hendra, and A.J. McQuillan, *Raman spectra of pyridine adsorbed at a silver electrode.* Chemical Physics Letters, 1974. **26**(2): p. 163-166.
50. Moskovits, M., *Surface-Enhanced Spectroscopy.* Reviews of Modern Physics, 1985. **57**(3): p. 783-826.
51. Jensen, T.R., et al., *Nanosphere Lithography: Tunable Localized Surface Plasmon Resonance Spectra of Silver Nanoparticles.* Journal of Physical Chemistry B, 2000. **104**(45): p. 10549-10556.
52. Kneipp, K., et al., *Single molecule detection using surface-enhanced Raman scattering (SERS).* Physical Review Letters, 1997. **78**(9): p. 1667-1670.
53. Nie, S. and S.R. Emory, *Probing single molecules and single nanoparticles by surface-enhanced Raman scattering.* Science, 1997. **275**(5303): p. 1102-1106.
54. McCall, S.L., P.M. Platzman, and P.A. Wolff, *Surface enhanced Raman scattering.* Physics Letters A, 1980. **77A**(5): p. 381-383.

55. Campion, A., et al., *On the Mechanism of Chemical Enhancement in Surface-Enhanced Raman Scattering.* Journal of the American Chemical Society, 1995. **117**(47): p. 11807-8.
56. Zhao, L.L., L. Jensen, and G.C. Schatz, *Surface-Enhanced Raman Scattering of Pyrazine at the Junction between Two Ag20 Nanoclusters.* Nano Letters, 2006. **6**(6): p. 1229-1234.
57. Kneipp, K., et al., *Surface-enhanced Raman scattering: A new tool for biomedical spectroscopy.* Current Science, 1999. **77**(7): p. 915-924.
58. Hou, Y. and D.A. Higgins, *Single Molecule Studies of Dynamics in Polymer Thin Films and at Surfaces: Effect of Ambient Relative Humidity.* J. Phys. Chem. B, 2002. **106**(40): p. 10306-10315.
59. Jackson, J.B., *Classical Electrodynamics*. 2nd ed. 1975: Wiley, New York.
60. Kreibig, U. and M. Vollmer, *Optical Properties of Metal Clusters*. Vol. 25. 1995: Springer series in material science.
61. Mie, G., Ann. Phys., 1908. **25**: p. 377-445.
62. Messinger, B.J., et al., *Local fields at the surface of noble-metal microspheres.* Physical Review B, 1981. **24**(2): p. 649-57.
63. Talley, C.E., et al., *Surface-Enhanced Raman Scattering from Individual Au Nanoparticles and Nanoparticle Dimer Substrates.* Nano Letters, 2005. **5**(8): p. 1569-1574.
64. Rechberger, W., et al., *Optical properties of two interacting gold nanoparticles.* Optics Communications, 2003. **220**(1-3): p. 137-141.
65. Sweatlock, L.A., et al., *Highly confined electromagnetic fields in arrays of strongly coupled Ag nanoparticles.* Physical Review B, 2005. **71**(23): p. 235408/1-235408/7.
66. Salerno, M., et al., *The optical near-field of gold nanoparticle chains.* Optics Communications, 2005. **248**(4-6): p. 543-549.
67. Hohenester, U. and J. Krenn, *Surface plasmon resonances of single and coupled metallic nanoparticles: A boundary integral method approach.* Physical Review B: Condensed Matter and Materials Physics, 2005. **72**(19): p. 195429/1-195429/9.
68. Jain, P.K., W. Huang, and M.A. El-Sayed, *On the Universal Scaling Behavior of the Distance Decay of Plasmon Coupling in Metal Nanoparticle Pairs: A Plasmon Ruler Equation.* Nano Letters, 2007. **7**(7): p. 2080-2088.
69. Xu, H. and M. Kaell, *Polarization-dependent surface-enhanced Raman spectroscopy of isolated silver nanoaggregates.* ChemPhysChem, 2003. **4**(9): p. 1001-1005.
70. Felidj, N., et al., *Grating-induced plasmon mode in gold nanoparticle arrays.* Journal of Chemical Physics, 2005. **123**(22): p. 221103/1-221103/5.
71. Michaels, A.M., J. Jiang, and L. Brus, *Ag Nanocrystal Junctions as the Site for Surface-Enhanced Raman Scattering of Single Rhodamine 6G Molecules.* Journal of Physical Chemistry B, 2000. **104**(50): p. 11965-11971.
72. Suh, Y.D., et al., *Probing nanoscale surface enhanced Raman-scattering fluctuation dynamics using correlated AFM and confocal ultramicroscopy.* Ultramicroscopy, 2003. **97**(1-4): p. 89-102.

73. Khan, I., et al., *A TEM and electron energy loss spectroscopy (EELS) investigation of active and inactive silver particles for surface enhanced resonance Raman spectroscopy (SERRS).* Faraday Discussions, 2006. **132**: p. 171-178.

74. Svedberg, F., et al., *Creating Hot Nanoparticle Pairs for Surface-Enhanced Raman Spectroscopy through Optical Manipulation.* Nano Letters, 2006. **6**(12): p. 2639-2641.

75. Xu, H.X., et al., *Spectroscopy of single hemoglobin molecules by surface enhanced Raman scattering.* Physical Review Letters, 1999. **83**(21): p. 4357-4360.

76. Dadosh, T., et al., *Measurement of the conductance of single conjugated molecules.* Nature, 2005. **436**(7054): p. 677-680.

77. Grabar, K.C., et al., *Two-dimensional arrays of colloidal gold particles: A flexible approach to macroscopic metal surfaces.* Langmuir, 1996. **12**(10): p. 2353-2361.

78. Handley, D.A., *Colloidal Gold - Principles, Methods, and Applications*. Hayat, M. A. ed. Vol. 13. 1989, New York: Academic Press.

79. Weisbecker, C.S., M.V. Merritt, and G.M. Whitesides, *Molecular self-assembly of aliphatic thiols on gold colloids.* Langmuir, 1996. **12**(16): p. 3763-3772.

80. Ron, H., S. Matlis, and I. Rubinstein, *Self-Assembled Monolayers on Oxidized Metals. 2. Gold Surface Oxidative Pretreatment, Monolayer Properties, and Depression Formation.* Langmuir, 1998. **14**(5): p. 1116-1121.

81. http://www.biomath.info/power/chsq.htm, *Chi-square*.

82. Krahne, R., et al., *Fabrication of nanoscale gaps in integrated circuits.* Applied Physics Letters, 2002. **81**(4): p. 730-732.

83. Amlani, I., et al., *An approach to transport measurements of electronic molecules.* Applied Physics Letters, 2002. **80**(15): p. 2761-2763.

84. Krahne, R., et al., *Nanoparticles and nanogaps: controlled positioning and fabrication.* Physica E-Low-Dimensional Systems & Nanostructures, 2003. **17**(1-4): p. 498-502.

85. Ramos, A., et al., *The role of electrohydrodynamic forces in the dielectrophoretic manipulation and separation of particles.* Journal of Electrostatics, 1999. **47**(1-2): p. 71-81.

86. Hazani, M., et al., *DNA-mediated self-assembly of carbon nanotube-based electronic devices.* Chemical Physics Letters, 2004. **391**(4-6): p. 389-392.

87. Hanna, A.E. and M. Tinkham, *Variation of the Coulomb Staircase in a 2-Junction System By Fractional Electron Charge.* Physical Review B, 1991. **44**(11): p. 5919-5922.

88. Xiao, X.Y., B.Q. Xu, and N.J. Tao, *Measurement of single molecule conductance: Benzenedithiol and benzenedimethanethiol.* Nano Letters, 2004. **4**(2): p. 267-271.

89. Maiti, S.K., *Effect of localizing groups on quantum transport through single conjugated molecules.* Physica B: Condensed Matter, 2007. **394**(1): p. 33-38.

90. Lee, S.K., et al., *Rapid sonochemical synthesis of spherical-shaped mesoporous SBA-15 silica and Ti-incorporated SBA-15 silica materials.* Journal of Industrial and Engineering Chemistry, 2003. **9**(1): p. 83-88.

91. Remacle, F. and R.D. Levine, *Electrical transmission of molecular bridges.* Chemical Physics Letters, 2004. **383**(5-6): p. 537-543.

92. Lee, P.C. and D. Meisel, *Adsorption and Surface-Enhanced Raman of Dyes on Silver and Gold Sols.* journal of physical chemistry, 1982. **86**: p. 3391-3395.

93. Slot, J.W. and H.J. Geuze, *A new method of preparing gold probes for multiple-labeling cytochemistry.* European journal of cell biology, 1985. **38**(1): p. 87-93.

94. Zhang, J., et al., *Metal-Enhanced Single-Molecule Fluorescence on Silver Particle Monomer and Dimer: Coupling Effect between Metal Particles.* Nano Letters, 2007.

95. Tam, I.W., J. Yan, and R. Breslow, *An 11 nm Molecular Wire that Switches Electrochemically between an Insulating and a Fully Conjugated Conducting State.* Organic Letters, 2006. **8**(2): p. 183-185.

96. Sarkar, U.K., et al., *Surface enhanced Raman spectroscopic study of [alpha]-bithiophene and [alpha]-quaterthiophene molecules adsorbed on silver sols.* Spectrochimica Acta Part A: Molecular Spectroscopy, 1992. **48**(11-12): p. 1625-1630.

97. Fujita, W., N. Teramae, and H. Haraguchi, *Formation of thiophene oligomers and polythiophene on a roughened gold electrode studied by surface enhanced Raman scattering.* Chemistry Letters, 1994(3): p. 511-14.

98. Casado, J., et al., *Infrared and Raman features of a series of alpha,omega-bis(arylthio)oligothiophenes as molecular wires. A pi-electron delocalization efficiency study.* Journal of Chemical Physics, 2003. **118**(4): p. 1912-1920.

99. Vosgrone, T. and A.J. Meixner, *Surface- and resonance-enhanced micro-raman spectroscopy of xanthene dyes: From the ensemble to single molecules.* Chemphyschem, 2005. **6**(1): p. 154-163.

100. Chowdhury, J., et al., *Surface-enhanced Raman scattering of Rhodamine 123 in silver hydrosols and in Langmuir-Blodgett films on silver islands.* Journal of Colloid and Interface Science, 2001. **235**(2): p. 317-324.

101. Yip, W.-T., et al., *Classifying the photophysical dynamics of single- and multiple-chromophoric molecules by single molecule spectroscopy.* Journal of Physical Chemistry A, 1998. **102**(39): p. 7564-7575.

102. Gensch, T., M. Boehmer, and P.F. Aramendia, *Single Molecule Blinking and Photobleaching Separated by Wide-Field Fluorescence Microscopy.* Journal of Physical Chemistry A, 2005. **109**(30): p. 6652-6658.

103. Weber, W., et al., *Shedding light on the dark and weakly fluorescent states of green fluorescent proteins.* PNAS, 1999. **96**(11): p. 6177-6182.

104. Aizpurua, J., et al., *Optical properties of coupled metallic nanorods for field-enhanced spectroscopy.* Physical Review B, 2005. **71**(23): p. 235420/1-235420/13.

105. Toher, C. and S. Sanvito, *Effects of self-interaction corrections on the transport properties of phenyl-based molecular junctions.* Los Alamos National Laboratory, Preprint Archive, Condensed Matter, 2007: p. 1-12, arXiv:0712.1747v1 [cond-mat.mes-hall].

106. Zou, B., et al., *Effects of field-induced geometry relaxation on the electron transport properties of 4,4'-biphenyldithiol molecular junction.* Chemical Physics Letters, 2007. **447**(1-3): p. 69-73.

107. Na, J.-S., et al., *Conduction mechanisms and stability of single molecule nanoparticle/molecule/nanoparticle junctions.* Nanotechnology, 2007. **18**(3): p. 035203/1-035203/8.

108. Baron, A.L. and D.R. Blank, *Synthesis and properties of some aromatic polythioethers.* Makromolekulare Chemie, 1970. **140**: p. 83-9.

List of publications

1. Dadosh, T., Gordin, Y., Krahne, R., Khivrich, I., Mahalu, D., Frydman, V., Sperling, J., Yacoby, A., and Bar-Joseph, I. (2005). Measurement of the Conductance of Single Conjugated Molecules. ***Nature*** 436, 677-680.
2. Krahne, R., Dadosh, T., Gordin, Y., Yacoby, A., Shtrikman, H., Mahalu, D., Sperling, J., and Bar-Joseph, I. (2003). Nanoparticles and Nanogaps: Controlled Positioning and Fabrication. ***Physica E***: Low-Dimensional Systems & Nanostructures 17, 498-502.
3. Krahne, R., Yacoby, A., Shtrikman, H., Bar-Joseph, I., Dadosh, T., and Sperling, J. (2002). Fabrication of Nanoscale Gaps in Integrated Circuits. ***Applied Physics Letters*** 81, 730-732.
4. Dadosh, T., Haran, G., Sperling, J., and Bar-Joseph, I., SERS of dimeric nanoparticle structures, *in preparation.*
5. Shegai, T., Li, Z., Dadosh T., Xu, H., and Haran H., Frequency-dependent polarization of Raman-scattered light from nanocrystal aggregates: Theory meets experiment, *Submitted.*
6. Dadosh, T., Haran, G., Bar-Joseph, I. and Sperling, J., Synthesis of mono-dispersed silver nanoparticles, *in preparation.*

Collaborations

SERS measurements

The SERS project was done with full collaboration with Prof. Gilad Haran from the Chemical Physics department at the Weizmann Institute.

Synthesis of the polythiophene molecule (T4)

Prof. Ronald Breslow and his former student, Dr. Iris Tam, from Colombia University synthesized the T4 molecule.

Plasminics calculation

The calculations of the SERS enhancement that appear in Figures 53 and 54 were performed by Garnett Bryant from NIST.

Synthesis of BPD and BPE molecules

The synthesis was carried out by Veronica Frydman from the Chemical Services unit at the Weizmann Institute.